STUDIES ON THE TRIGGER CONFIGURATION FOR THE JUNO EXPERIMENT

STUDIEN ZUR TRIGGERKONFIGURATION FÜR DAS JUNO-EXPERIMENT

von
RIKHAV SHAH

MASTERARBEIT IN PHYSIK
vorgelegt der
FAKULTÄT FÜR MATHEMATIK, INFORMATIK UND

NATURWISSENSCHAFTEN
der
RWTH AACHEN

September 2018

angefertigt im
PHYSIKALISCHEN INSTITUT III. B

Erstgutachter und Betreuer

PROF. DR. LIVIA LUDHOVA
Physikalischen Institut III B
RWTH Aachen

Zweitgutachter

PROF. DR. ACHIM STAHL
Physikalischen Institut III B
RWTH Aachen

Ich versichere, dass ich die Arbeit selbstständig verfasst und keine anderen als die angegebenen Quellen und Hilfsmittel benutzt sowie Zitate kenntlich gemacht habe.

Aachen, den 24. September 2018

Abstract

JUNO (Jiangmen Underground Neutrino Observatory) is a $20\,$kton multiple purpose liquid scintillator detector under construction in Kaiping, China. The chief goal of JUNO is the determination of the neutrino mass hierarchy, the prime question facing neutrino physics. The other aims of JUNO include precision measurements of neutrino oscillations parameters from the solar, astrophysical and atmospheric neutrinos. For this, JUNO is designed to have an energy resolution of $3\%/\sqrt{\mathrm{MeV}}$, provided by $\sim\!18,000$ photomultiplier tubes (PMTs) surrounding the $34\,$m diameter spherical vessel. JUNO will observe $\sim\!83$ antineutrino interactions per day, with antineutrinos originating from the nearby Yangjiang and Taishan fission reactors. Within 6 years of data-taking, this is expected to lead to a $3-4\sigma$ sensitivity on the neutrino mass hierarchy.

The study of the trigger configuration is undertaken to optimize a resulting trigger condition. The goal of this thesis is the minimization the effects of the dark noise from the PMTs on low-energy events. This is carried out by parameterizing the detector with respect to two characteristic features: the event location and the trigger decision window (trigger window) for the PMT setup. The optimum trigger settings can then be obtained from the threshold energies and trigger efficiency. The radioactive decays of unstable nuclei like ^{210}Po, ^{238}U, etc. in the liquid scintillator lead to large, non-negligible backgrounds in JUNO. The data acquisition system in JUNO is required to cope with these contaminants, which are investigated for their influence on the trigger rate. Solar neutrinos are also investigated similarly, with neutrinos originating in pp and ^{7}Be decays in the Sun.

Contents

1

Introduction

Neutrinos, which were first understood in the 20th century as *dark* particles in β-decay, have come to be a new and novel way of probing areas of solar physics, geophysics and particle physics. Along with forming an important part of new fields like multi-messenger astroparticle physics, neutrino physics also seeks to shed light on physical processes not described by the Standard Model.

The standard electroweak model put forth in 1967 by S. Weinberg [1] successfully explained electroweak phenomena, assuming neutrinos to be massless and thus had no lepton flavour mixing. Subsequent experiments found that neutrinos do however switch flavours, and must therefore have non-zero mass. This tendency of neutrinos was inspired by the possibility of $K^0 \rightleftarrows \bar{K}^0$ oscillations [2] put forth by Landau[3], Lee and Yang[4], and Salam[5].

This periodic conversion of a neutrino into one of another flavours, described by B. Pontecorvo in 1957 ([6][7]), was first observed by the Homestake experiment [8] in 1968. The observed neutrino flux in Homestake was a third of the value expected from the standard solar model [9]. The ensuing "solar neutrino problem" was laid to rest by the results of SNO[10], as the sum of the fluxes of all neutrino flavours matched the predicted solar neutrino flux. The electron neutrinos (ν_e) created in the Sun may change into another flavour upon reaching the Earth. Spurred on by further neutrino experiments [11][12], a new era of neutrino physics led to the search for properties used to parametrize neutrino oscillations (mixing angles, mass differences, etc.).

Neutrino detection has a rich history with multiple detectors operating with different mechanisms - from detecting Čerenkov radiation in IceCube[13] and Super-K[14] to analyzing liquid scintillation in DUNE [15] (water based, for accelerator neutrinos), Borexino [16], JUNO [17] and others. While neutrino interactions of any kind are rare, they span a large range in energy - from keV, e.g. neutrinos produced in the Sun, to PeV, e.g. cosmic neutrinos from active galactic nuclei. Analyzing the lower end of this range is challenging due to the prevalence of other physical processes like radioactive decays and noise originating from the detector setup. These could show up as events similar to neutrino interactions and contaminate the signal. In a liquid scintillator detector the size of JUNO, with its large fiducial mass and excellent energy resolution, the problem of triggering and detecting neutrino events becomes one of utmost importance.

3

This problem is compounded by the data acquisition system of JUNO, which includes the photomultiplier tubes (PMTs). A typical neutrino event[1] in a liquid scintillator detector emits multiple photons which strike the PMTs lining the spherical detector, with each photon detected by a PMT registering as a hit. The PMTs add to the problem of triggering by providing a constant source of background in the form of *dark* hits; this noise is due to their optical amplification properties and architecture. In order to successfully trigger on neutrino events, an investigation is carried out into the effects of the dark hits on low-energy neutrino events.

With its sights on some of the goals of neutrino physics, the first part of this thesis investigates the trigger setup of the detector vis-à-vis parameters like the event vertex. This allows us to see the different possibilities of obtaining a trigger condition with respect to a chosen background, such as the constant dark hits (dark noise) from the PMTs. In this regard, the trigger configuration of the detector can be optimized to go low enough in terms of energy to detect solar neutrinos and to understand the treatment of low-energy events. With a simulated data set, it is possible to see the variation of this treatment for events of different (albeit low) energies and different event vertices in the detector. The time window used to make a trigger decision (trigger window) is also important to see the effect of the event vertex, dark noise and event energy on the detector characteristics. The latter half of this thesis describes the effects of internal (liquid scintillator-originating) radioactivity from the decay of nuclei, and solar neutrino events, on the trigger rate.

---

[1]This event could be neutrino-electron scattering, neutrino-proton scattering or an inverse beta decay (IBD).

2

Neutrino oscillations and mixing

Here we discuss the mechanism by which a neutrino undergoes oscillation, the parameters that describe such oscillations, and the quantities important for JUNO.

2.1   Oscillation mechanism

The three-neutrino-mass and flavour mixing paradigm explains the different oscillation phenomena and also keeps open the possibility of a $(3+n)$ scheme with n sterile neutrinos. Since neutrinos experience only the weak interaction, they are detected as the eigenstates of the weak interaction: $|\nu_\alpha\rangle$, $(\alpha = e, \mu, \tau)$ but are propagated as mass eigenstates of the Hamiltonian $\hat{H}$: $|\nu_i\rangle$, $(i = 1, 2, 3)$. Each kind of eigenstate can be described in the basis of the other:

$$|\nu_\alpha\rangle = \sum_i U_{\alpha i} |\nu_i\rangle \ \text{and} \ |\nu_i\rangle = \sum_\alpha U_{\alpha i}^\dagger |\nu_\alpha\rangle \ , \tag{2.1}$$

where the U is the 3 x 3 Pontecorvo-Maki-Nakagawa-Sakata (PMNS) matrix [18] which provides the change in the bases. The corresponding matrix for antineutrinos is the complex conjugate of $U_{\alpha i}$, i.e. $U_{\alpha i}^*$. In the Chau-Keung scheme [19], U can be parametrized as: (assuming U is unitary):

$$U = \begin{bmatrix} 1 & 0 & 0 \\ 0 & c_{23} & s_{23} \\ 0 & -s_{23} & c_{23} \end{bmatrix} \begin{bmatrix} c_{13} & 0 & s_{23}e^{-\iota\delta} \\ 0 & 1 & 0 \\ -s_{23}e^{\iota\delta} & 0 & c_{13} \end{bmatrix} \begin{bmatrix} c_{12} & s_{12} & 0 \\ -s_{12} & c_{12} & 0 \\ 0 & 0 & 1 \end{bmatrix} \begin{bmatrix} e^{\iota\rho} & 0 & 0 \\ 0 & e^{\iota\sigma} & 0 \\ 0 & 0 & 1 \end{bmatrix} \tag{2.2}$$

$$= \begin{bmatrix} c_{12}c_{13} & s_{12}s_{13} & s_{13}e^{-\iota\delta} \\ -s_{12}c_{23} - c_{12}s_{13}s_{23}e^{\iota\delta} & c_{12}c_{23} - s_{12}s_{13}s_{23}e^{\iota\delta} & c_{13}s_{23} \\ s_{12}s_{23} - c_{12}s_{13}s_{23}e^{\iota\delta} & c_{12}s_{23} - s_{12}s_{13}c_{23}e^{\iota\delta} & c_{13}c_{23} \end{bmatrix} \begin{bmatrix} e^{\iota\rho} & 0 & 0 \\ 0 & e^{\iota\sigma} & 0 \\ 0 & 0 & 1 \end{bmatrix} , \tag{2.3}$$

where $c_{ij} = \cos\theta_{ij}$ and $s_{ij} = \sin\theta_{ij}$. θ_{12}, θ_{23} and $\theta_{13} \in [0, \pi/2]$ are the three mixing angles, $\delta \equiv \delta_{CP} \in [0, 2\pi)$ is the (Dirac) CP-violating phase, and ρ, σ are the Majorana CP-violating phases (if neutrinos are Majorana particles). The Majorana phases do not influence the oscillation as they are present only on the main diagonal.

The propagation of neutrinos is approximated as a plane wave, which is governed by the Schrödinger equation and the Hamiltonian $\hat{H}$:

$$\iota\frac{\partial}{\partial t} |\nu_i(t)\rangle = \hat{H} |\nu_i(t)\rangle , \tag{2.4}$$

with the solution (in a vacuum)

$$|\nu_i(t)\rangle = e^{-\iota E_i t} |\nu_i(t = 0)\rangle \tag{2.5}$$

$$\implies |\nu_\alpha(t)\rangle = \sum_\alpha U_{\alpha i}^\dagger |\nu_i(t = 0)\rangle e^{-\iota E_i t} \tag{2.6}$$

The time dependent amplitude of the change from one flavour eigenstate to another ($A(\nu_\alpha \to \nu_\beta)$) will thus be:

$$A(\nu_\alpha \to \nu_\beta) = \langle \nu_\beta | \nu_\alpha(t) \rangle \tag{2.7}$$

$$= \sum_i U^\dagger_{\alpha i} U_{\beta i} e^{-\iota E_i t}. \tag{2.8}$$

For $E >> m$,

$$E = \sqrt{p^2 + m_i^2} \approx p + \frac{m_i^2}{2p} \approx E + \frac{m_i^2}{2E} \tag{2.9}$$

can be used in (2.8). Simultaneously substituting the time t by the proper distance travelled L and using the normalization term $\sqrt{(UU^\dagger)_{\alpha\alpha}}$ for a non-unitary PMNS matrix, we get

$$A(\nu_\alpha \to \nu_\beta) = \frac{1}{\sqrt{(UU^\dagger)_{\alpha\alpha}(UU^\dagger)_{\beta\beta}}} \sum_i \left[U^*_{\alpha i} e^{-\iota \frac{m_i^2 L}{2E}} U_{\beta i} \right]. \tag{2.10}$$

The probability of this oscillation is $P(\nu_\alpha \to \nu_\beta) = |A(\nu_\alpha \to \nu_\beta)|^2$, which is

$$P = \frac{1}{(UU^\dagger)_{\alpha\alpha}(UU^\dagger)_{\beta\beta}} \left\{ |U_{\alpha i}|^2 |U_{\beta i}|^2 + 2\sum_{i<j} \left[\left(\Re\left(U_{\alpha i} U_{\beta j} U^*_{\alpha j} U^*_{\beta i} \right) \cos\left(\frac{\Delta m_{ij}^2 L}{2E} \right) \right) \right.\right.$$
$$\left.\left. - \Im\left(U_{\alpha i} U_{\beta j} U^*_{\alpha j} U^*_{\beta i} \right) \sin\left(\frac{\Delta m_{ij}^2 L}{2E} \right) \right] \right\}, \tag{2.11}$$

where $\Delta m_{ij}^2 = m_i^2 - m_j^2$. The probability of the oscillation $\bar{\nu}_\alpha \to \bar{\nu}_\beta$ can be seen from (2.11) with $U \to U^*$. The incoming reactor anti-(electron) neutrinos serve as the main source of the JUNO signal. For this signal, we measure the disappearance of the reactor antineutrinos, which we get from (2.11) as the survival probability with $\alpha = \beta = e$ (using (2.3)):

$$P(\bar{\nu}_e \to \bar{\nu}_e) = 1 - (\sin^2 2\theta_{12}) c_{13}^4 \sin^2\left(\frac{\Delta m_{21}^2 L}{4E} \right)$$
$$- (\sin^2 2\theta_{13}) \left[c_{12}^2 \sin^2\left(\frac{\Delta m_{31}^2 L}{4E} \right) + (s_{12}^2) \sin^2\left(\frac{\Delta m_{32}^2 L}{4E} \right) \right], \tag{2.12}$$

where $\Delta m_{23}^2 = \Delta m_{31}^2 - \Delta m_{21}^2$ and s_{ij}, c_{ij} are as previously defined (from [17]). JUNO aims to measure the energy spectrum of $\bar{\nu}_e \to \bar{\nu}_e$ to pin down the neutrino mass hierarchy, or conversely, measure the sign of Δm_{31}^2.

2.2 Neutrino oscillation parameters

While great strides have been made in the analysis of oscillation parameters, neutrino physics faces a plethora of open questions which shall be discussed. In the standard 3-flavour neutrino model, six independent parameters govern neutrino oscillations: two mass-squared differences: Δm_{31}^2 and Δm_{21}^2, three mixing angles: θ_{12}, θ_{13}, θ_{23}, and a Dirac CP-violating phase δ. From 1989 to the present day, a variety of solar, atmospheric, reactor, and accelerator neutrino experiments [20] have provided evidence for neutrino oscillations and determined these oscillation parameters. The current, best-known values of these oscillation

parameters can be found in Figure 2.1, from [21]. The results in 2.1 are from data sets collected from Gallex/GNO [22], SAGE[23], SNO (3 phases)[24], Super-K (4 phases)[25], and Borexino (Phase-I and -II) [26]. It also includes long baseline data from $\nu_\mu, \bar\nu_\mu$ disappearance and $\nu_e, \bar\nu_e$ appearance channels in MINOS [27], NoνA[28], KamLAND[29] and T2K[30], and medium baseline neutrino experiments like CHOOZ[31] and Palo Verde[32]. Running experiments like Daya Bay[33] and RENO[34] also provide spectral data. From these values,

NuFIT 3.2 (2018)

	Normal Ordering (best fit)		Inverted Ordering ($\Delta\chi^2 = 4.14$)		Any Ordering
	bfp $\pm 1\sigma$	3σ range	bfp $\pm 1\sigma$	3σ range	3σ range
$\sin^2\theta_{12}$	$0.307^{+0.013}_{-0.012}$	$0.272 \to 0.346$	$0.307^{+0.013}_{-0.012}$	$0.272 \to 0.346$	$0.272 \to 0.346$
$\theta_{12}/°$	$33.62^{+0.78}_{-0.76}$	$31.42 \to 36.05$	$33.62^{+0.78}_{-0.76}$	$31.43 \to 36.06$	$31.42 \to 36.05$
$\sin^2\theta_{23}$	$0.538^{+0.033}_{-0.069}$	$0.418 \to 0.613$	$0.554^{+0.023}_{-0.033}$	$0.435 \to 0.616$	$0.418 \to 0.613$
$\theta_{23}/°$	$47.2^{+1.9}_{-3.9}$	$40.3 \to 51.5$	$48.1^{+1.4}_{-1.9}$	$41.3 \to 51.7$	$40.3 \to 51.5$
$\sin^2\theta_{13}$	$0.02206^{+0.00075}_{-0.00075}$	$0.01981 \to 0.02436$	$0.02227^{+0.00074}_{-0.00074}$	$0.02006 \to 0.02452$	$0.01981 \to 0.02436$
$\theta_{13}/°$	$8.54^{+0.15}_{-0.15}$	$8.09 \to 8.98$	$8.58^{+0.14}_{-0.14}$	$8.14 \to 9.01$	$8.09 \to 8.98$
$\delta_{\rm CP}/°$	234^{+43}_{-31}	$144 \to 374$	278^{+26}_{-29}	$192 \to 354$	$144 \to 374$
$\dfrac{\Delta m^2_{21}}{10^{-5}\ \rm eV^2}$	$7.40^{+0.21}_{-0.20}$	$6.80 \to 8.02$	$7.40^{+0.21}_{-0.20}$	$6.80 \to 8.02$	$6.80 \to 8.02$
$\dfrac{\Delta m^2_{3\ell}}{10^{-3}\ \rm eV^2}$	$+2.494^{+0.033}_{-0.031}$	$+2.399 \to +2.593$	$-2.465^{+0.032}_{-0.031}$	$-2.562 \to -2.369$	$\begin{bmatrix}+2.399 \to +2.593 \\ -2.536 \to -2.395\end{bmatrix}$

Figure 2.1: Three-flavor oscillation parameters from fit to global data as of November 2018. The numbers in the 1st (2nd) column are obtained assuming Normal Ordering (NO) (and Inverted Ordering (IO)), i.e., relative to the respective local minimum, whereas in the 3rd column it is minimized with respect to the ordering. Data from [35].

an estimate of the mixing matrix U_{PMNS} up to 3σ can be found (albeit with strong emphasis on unitarity): Ongoing and future neutrino experiments are expected to shed light on

NuFIT 3.2 (2018)

$$|U|_{3\sigma} = \begin{pmatrix} 0.799 \to 0.844 & 0.516 \to 0.582 & 0.141 \to 0.156 \\ 0.242 \to 0.494 & 0.467 \to 0.678 & 0.639 \to 0.774 \\ 0.284 \to 0.521 & 0.490 \to 0.695 & 0.615 \to 0.754 \end{pmatrix}$$

Figure 2.2: The U_{PMNS} from the values in 2.1 up to a 3σ limit. The unitarity constraint leads to strong correlations between the elements in the matrix.

certain topics such as:

- $|\Delta m^2_{13}|$: The values of θ_{13}, θ_{23} and δ_{CP} in a global fit such as 2.1 are sensitive to sign of Δm^2_{31}, making it necessary in JUNO and other experiments to determine which neutrino has the lowest mass, ν_3 or ν_1; i.e. if $\Delta m^2_{13} > 0$ or $\Delta m^2_{13} < 0$.

- δ_{CP}: As $\delta_{CP} \neq 0$ at the 2σ level, it implies a possibility of CP-violation in the neutrino sector. This is likely to show up in long-baseline neutrino oscillation experiments.

- θ_{23}: As $\theta_{23} \approx 45°$, it can lie in either the first or second octant (within 1σ). Resolving the octant it lies in is important to pin down the geometrical structure of the PMNS matrix U.

For $\mu - \tau$ symmetry to hold (in U_{PMNS}), one of two conditions must hold: $\theta_{13} = 0°$ and $\theta_{23} = 45°$, or $\delta_{CP} = 90°(270°)$ and $\theta_{23} = 45°$. Daya Bay data [36] has already shown evidence for $\theta_{13} \neq 0°$, so the values of θ_{23}, δ_{CP} are needed so as to find the strength of $\mu - \tau$ symmetry breaking in U_{PMNS}.

2.3 Open questions in neutrino physics

A large number of questions remain unanswered in neutrino physics, some of which we discuss here.
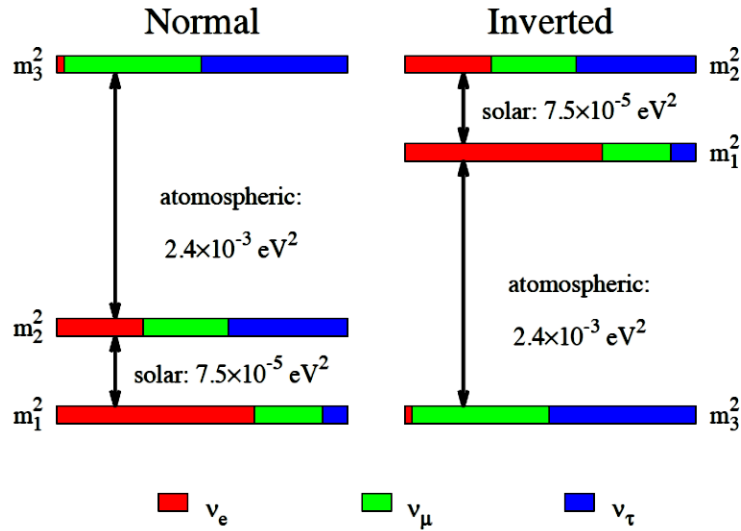

Figure 2.3: Ordering of the neutrino masses according to the normal and inverted hierarchies, from [17].

- *Neutrino mass hierarchy*: While we know from the solar sector that $\Delta m^2_{21} > 0$; a model-independent approach is lacking for the sign of Δm^2_{31} (see Figure 2.3). The sign of Δm^2_{31} impacts various processes in particle physics, astrophysics and cosmology. The neutrino mass ordering that comes with knowing the sign of Δm^2_{31} may point to leptogenesis mechanisms [37] and the observed baryon asymmetry of the universe [38], [39]. The ambiguity in the sign of Δm^2_{31} could be solved by

    - *Probing matter effects*:
      The (terrestrial) Mikheyev-Smirnov-Wolfenstein effects [40], [41] on neutrino oscillations would be minimal for the JUNO reactor antineutrino signal due to the medium baseline and lower energy probed. Upcoming experiments such as PINGU and DUNE will also investigate these effects.

  – *Probing interference between Δm_{23}^2 and Δm_{31}^2:*
  The probability $P_{NH}(\bar{\nu}_e \to \bar{\nu}_e)$ for normal hierarchies is equal to the one for inverted hierarchy $P_{IH}(\bar{\nu}_e \to \bar{\nu}_e)$ with respect to the signs of $\Delta m_{31,23}^2$. However, for different values of $\Delta m_{31,23}^2$, $P_{NH}(\bar{\nu}_e \to \bar{\nu}_e) \neq P_{IH}(\bar{\nu}_e \to \bar{\nu}_e)$; an effect of the oscillations that shows up most for a distance of $\sim$50 km from the source of antineutrinos (for reactor antineutrinos).

- *Dirac or Majorana nature*: Neutrinos can either be Dirac particles, i.e. they have a unique antiparticle, or Majorana particles, i.e. they are their own antiparticles. If they are Majorana particles, they would violate lepton number conservation and annihilate with each other; the only feasible way to see this presently would be via a $0\nu\beta\beta$ decay. The sign of Δm_{13}^2 influences the effective mass in $0\nu\beta\beta$ decay $\langle m \rangle_{ee} \equiv \sum_i m_i U_{ei}^2$ [42]. In the 3-neutrino mixing paradigm, this would set a limit of $|\langle m \rangle_{ee}| \geq 0.01$ eV in the event that the mass hierarchy is inverted ($m_2 > m_1 > m_3$), or if the neutrino masses are nearly degenerate [17]. The low limit can be accessible in future $0\nu\beta\beta$ decay experiments.

- *Absolute mass scale*: The absolute value of neutrino masses requires data from non-oscillation experiments (as oscillation experiments measure mass squared differences), like the upper bound set by $0\nu\beta\beta$ decay for effective mass: $\langle m \rangle_e < 0.2$ eV [43]. The KATRIN experiment measuring tritium (^3H) decay will probe $\langle m \rangle_e$ with a sensitivity of 0.2 eV [44]. The Planck collaboration [45] also gives the cosmological limit for the sum of neutrino masses: $\sum_i m_i < 0.23$ eV.
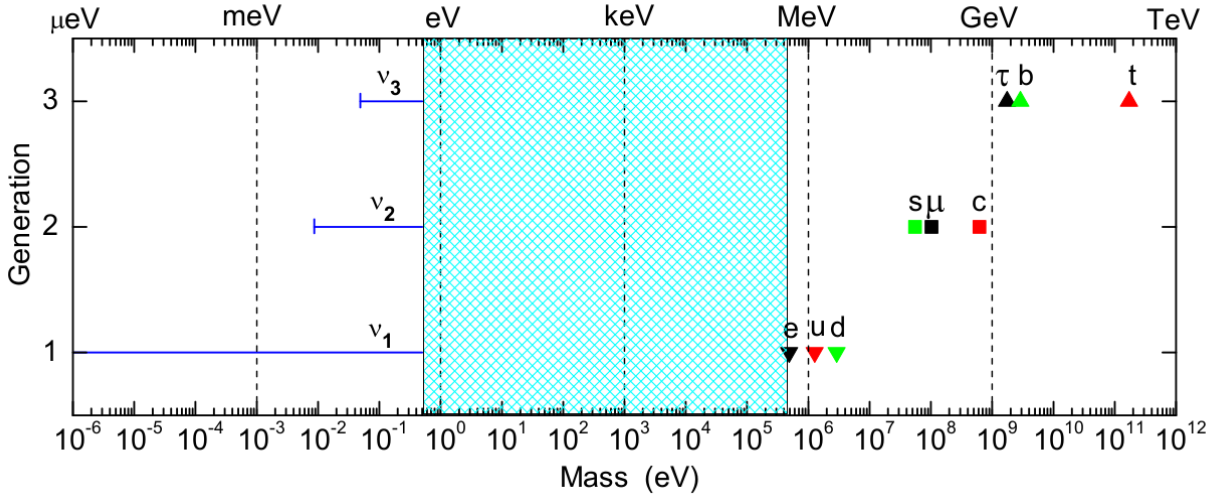

Figure 2.4: Schematic plot of "mass hierarchy" and "mass desert" (shaded blue region) with neutrinos ordered according to normal mass hierarchy, showing possible neutrino masses. Figure from [17].

- *The octant of θ_{23}*: $\mu-\tau$ flavour-symmetry models prefer $\theta_{23} = 45°$, so any different value could serve as a model discriminator [46]. Finding the octant of θ_{23} could be taken up in long-baseline or atmospheric neutrino oscillation experiments.

- δ_{CP}: Under CPT invariance, the extent of CP and T violation in neutrino oscillations is uniquely controlled by δ_{CP}. CP-violating effects could show up in neutrino oscillations

due to the existence of other massive neutrinos (violating the unitarity of the 3×3 PMNS matrix U) in long baseline experiments like T2K and in the future, DUNE and NoνA [47]. The measurement of δ, though, could be hampered in these experiments due to terrestrial matter effects in neutrino oscillations.

- *Extra neutrino species and unitarity tests for U_{PMNS}*: The existence of other neutrino species which do not experience the weak interaction [48] has roots in certain leptogenesis mechanisms and explanations of the matter-antimatter asymmetry in the universe [37]. A species of sterile neutrinos could also explain the anomalies seen in LSND [49], MiniBooNE [50] and reactor antineutrinos [51]. Such sterile neutrinos may also be good candidates for (warm) dark matter. They could modify the behaviour of the standard 3-flavour neutrino interactions and violate the unitarity of the 3×3 PMNS matrix U. Extra oscillation terms could then be added to $P(\bar{\nu}_e \rightarrow \bar{\nu}_e)$ (in 2.12).

3

Neutrino sources

With many open questions plaguing neutrino physics, a detector like JUNO is well poised to see different kinds of events and provide an answer. Neutrinos (and antineutrinos) arriving at the detector from different sources have varying characteristics, which we discuss here. The properties of the sources themselves and the processes that lead to the production of the neutrinos are also discussed. The spectra we expect to see, once possible events from these neutrinos have been detected, rely on the characteristics of the neutrino sources.

3.1 Anti-neutrinos

3.1.1 Reactor antineutrinos

The history of neutrino detection is flecked with experiments running in tandem with fission reactors, right from the early days of neutrino physics.

Anti-neutrinos in JUNO predominantly come from the nearby fission reactors, namely in Yangjiang and Taishan, which are $53\,$km away from the JUNO detector. The cores are all similar in design (water pressure reactors) and structure. The Yangjiang nuclear power plant (NPP) has six cores with a power of $\sim 3\,GW_{th}$ each, while Taishan NPP has 4 cores of $\sim 4.6\,GW_{th}$ each[1]. These are expected to have a combined power output of $\sim 36\,GW_{th}$ when data taking starts. In Figure 3.2, the antineutrino flux (in black) is shown with respect to the energy of the antineutrinos from the NPPs. The reactor antineutrinos are the products from the β-decay of unstable radioactive nuclei. In these reactors, 99.7% of the thermal energy generated and the electron antineutrinos ($\bar{\nu}_e$) generated is from the fission of 4 isotopes: ^{235}U, ^{238}U, ^{238}Pu and ^{241}Pu. Reactor neutrino fluxes per fission of each isotope are determined by inversion of the measured β spectra of fission products. The fission rates in a detector are predicted with:

$$\Phi(E_\nu) = \frac{W_{th}}{\sum_i f_i \cdot e_i} \cdot \sum_i f_i \cdot S_i(E_\nu) \,, \tag{3.1}$$

where W_{th} is the thermal power of the reactor; f_i, e_i, and $S_i(E_\nu)$ are the fission fraction, thermal energy per fission and the neutrino flux for the ith isotope respectively. This estimate comes with an uncertainty of 2-3%, and this neutrino flux is used in Figure 3.2 for JUNO. In the following chapters, the detection of reactor antineutrinos and geoneutrinos will be discussed with respect to JUNO.

---

[1]Yangjiang NPP's cores are 2nd generation CPR1000 (Improved Chinese pressure water reactor) cores and Taishan NPP's are 3rd generation Evolutionary Power Reactor (EPR) cores. All the reactors are manufactured and run by China General Nuclear Power Group (CGNPG).

Figure 3.1: The Yangjiang and Taishan NPPs (bottom left, in red), which serve as the main source of reactor antineutrinos for JUNO. The proposed (pending approval) power plants at Huizhou and Lufeng are also shown, these will be at a distance of ~300 km from JUNO but are of lesser importance. The Daya Bay NPP, which is 215 km away from JUNO, forms part of the Daya Bay complex with its other NPPs like Ling Ao-I and -II.
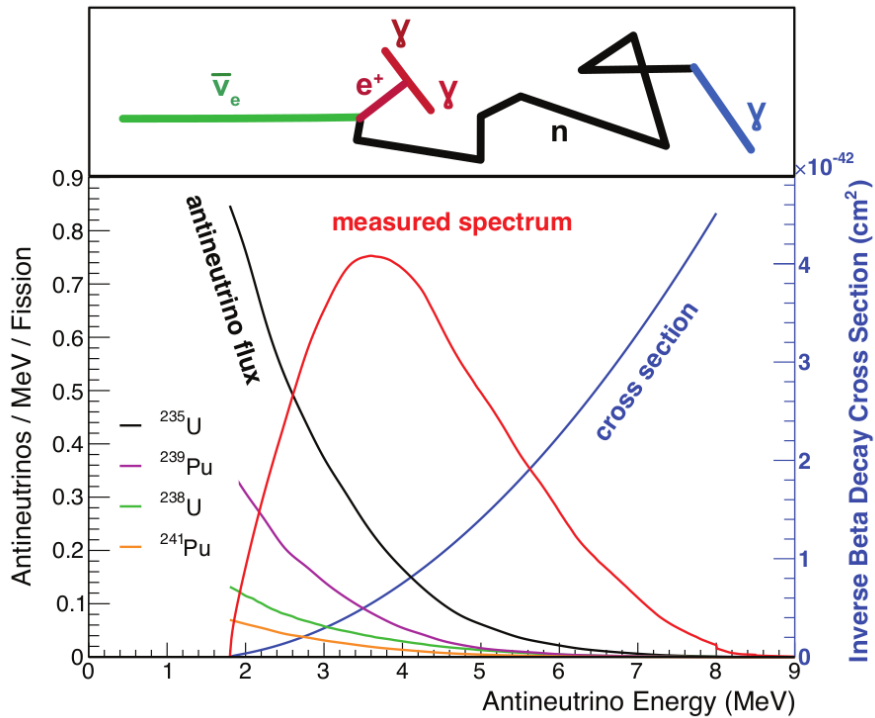

Figure 3.2: The shape of the expected unoscillated IBD spectrum (in red) is compared here with those of the antineutrino flux (in black, sum of all antineutrino fluxes; dominated by ^{235}U) as emitted from NPPs and the IBD interaction cross section (in blue). The steps involved in an IBD interaction are depicted above the plot. From [17].

3.1.2 Geoneutrinos

Over the years, a precise understanding of the Earth's surface heat flow (46 ± 3 TW [52]) has been obtained. However, there remains a debate regarding which fraction of this energy

Cores	YJ-C1	YJ-C2	YJ-C3	YJ-C4	YJ-C5	YJ-C6
Power (GW)	2.9	2.9	2.9	2.9	2.9	2.9
Baseline(km)	52.75	52.84	52.42	52.51	52.12	52.21
Cores	TS-C1	TS-C2	TS-C3	TS-C4	DYB	HZ
Power (GW)	4.6	4.6	4.6	4.6	17.4	17.4
Baseline(km)	52.76	52.63	52.32	52.20	215	265

Table 3.1: The thermal powers and the baselines to JUNO for Yangjiang (YJ), Taishan (TS), Daya Bay (DYB) and Huizhou (HZ). The baselines are measured to within 1 m precision by GPS. The distance between the reactor cores of Yangjiang is about 80 to 200 m, and for Taishan it is about 20 to 100 m.

comes from radiogenic and primordial sources. This has to do with the structural and chemical make-up of the Earth. Neutrino physics is essential in probing this area of geophysics, with the electron antineutrinos that make up the Earth's neutrino flux. These antineutrinos originate in the radioactive β-decay of elements occurring naturally in the Earth. Detecting the antineutrinos (from Earth's neutrino flux of $\sim 10^6 \, \text{cm}^{-2}\text{s}^{-1}$) can point to the concentrations of radioactive elements within the Earth, help understand Earth's heat budget, distinguish various models of the Earth's chemical composition, etc.

It is important to understand the relative contributions from the crust and mantle to the total geoneutrino signal at JUNO, and an accurate estimation of the geoneutrino flux from the crustal region surrounding JUNO is a priority. The global and regional contributions of the geoneutrino flux need to be predicted for the area surrounding the JUNO detector, as has been previously done at existing detectors as well.The unoscillated geoneutrino flux produced by a source volume ΔV at the detector position can be calculated with (integrated geoneutrino flux):

$$\Phi(\Delta V) = \frac{1}{4\pi} \int_{\Delta V} \frac{A(\vec{r})}{|\vec{R} - \vec{r}|^2} d^3\vec{r}, \tag{3.2}$$

where A is the rate of geoneutrino production in ΔV; which depends on the U, Th abundances, density and decay rates. $\vec{R}$ is the radius of the Earth. The intensity of the flux depends on the inverse-square of the distance to the sources, and thus the crust surrounding the detector, which contains a relatively small amount of the Earth's U and Th budget, has a large contribution in the signal.

The JUNO detector will thus accumulate a signal from the regional distribution of ^{232}Th and ^{238}U, as well as from the rest of the planet. The various contributions from different parts of the Earth are depicted in Figure 3.5. The main components constituting the theoretical geoneutrino signal (as seen in Figure 3.5) are electron antineutrinos from the chains of ^{238,235}U, ^{232}Th and ^{40}K decays. The different (relative) concentrations of these elements within the Earth can vary from model to model, changing the expected geoneutrino flux and the measured spectrum.
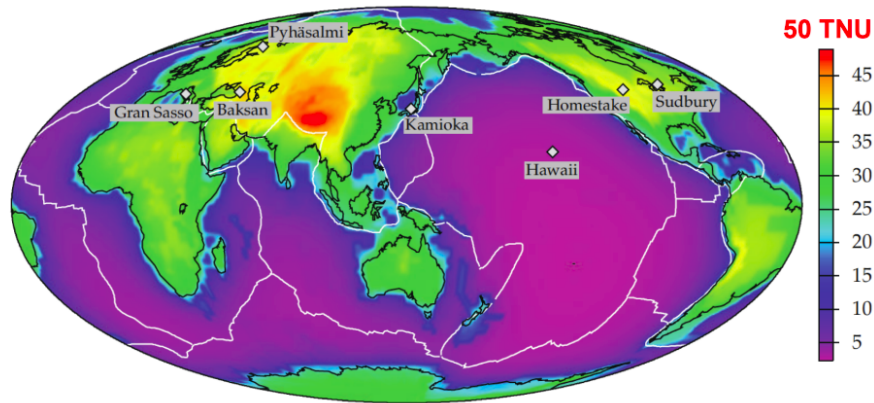
Figure 3.3: The contribution of the Earth's crust to the overall geoneutrino signal, measured in TNU. The geoneutrino signal is measured in TNU or terrestrial neutrino unit(s): 1 TNU corresponds to 1 geoneutrino event recorded over a year-long exposure of 10^{32} free protons (with 100% detection efficiency), which is approximately the number of free protons in a 1 kton liquid scintillation detector. This is analogous to the solar neutrino unit (SNU): 1 SNU equalling 1 interaction per second per 10^{36} target atoms. From [53].
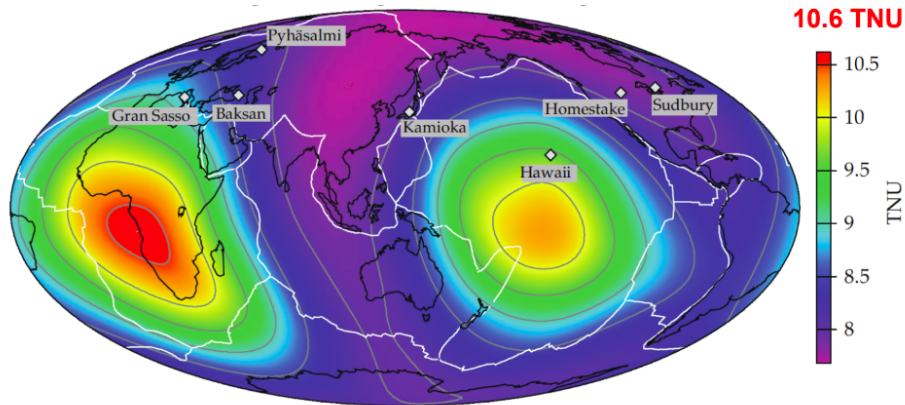
Figure 3.4: The mantle signal, measured in TNU. It is much more difficult to detect than the crustal signal. The various detector locations around the world (some proposed) can lead to an analysis of the contribution of different places in the Earth, to the geoneutrino signal. From [53].
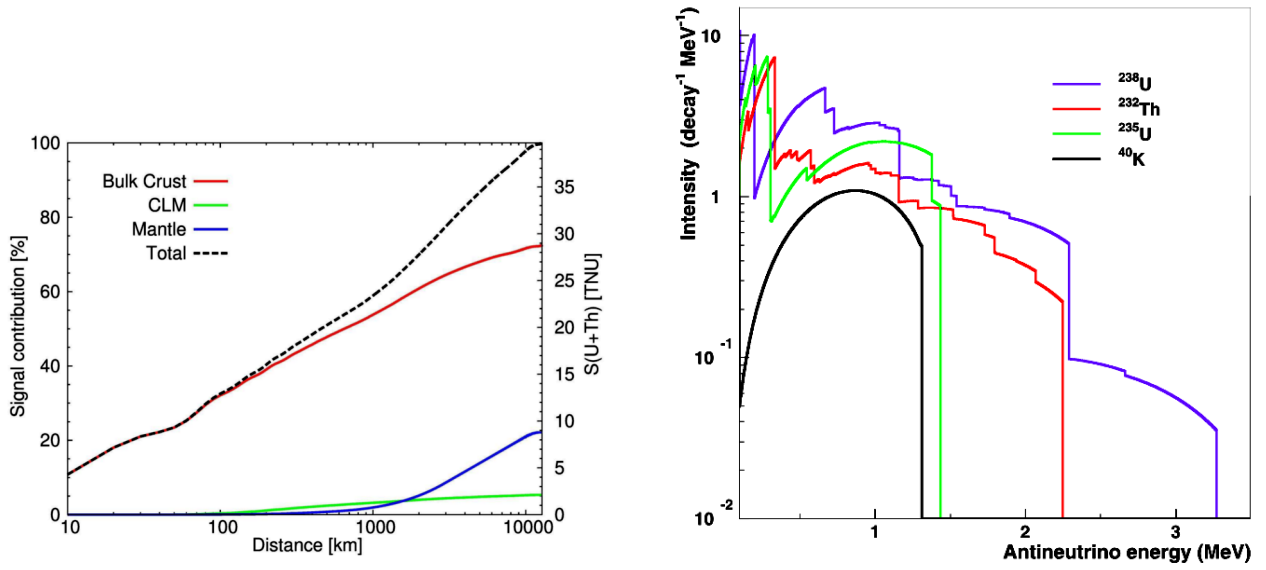
Figure 3.5: The contributing signal to the total geoneutrino signal expected at JUNO.The percentage contributions of the Bulk Crust, Continental Lithospheric Mantle (CLM) and Mantle are represented as function of the distance from JUNO, from [17]. On the right plot, the various contributing sources to the signal are shown, from [54]. The contribution comes from ^{238}U and ^{232}Th decays, which have energy above the IBD threshold.
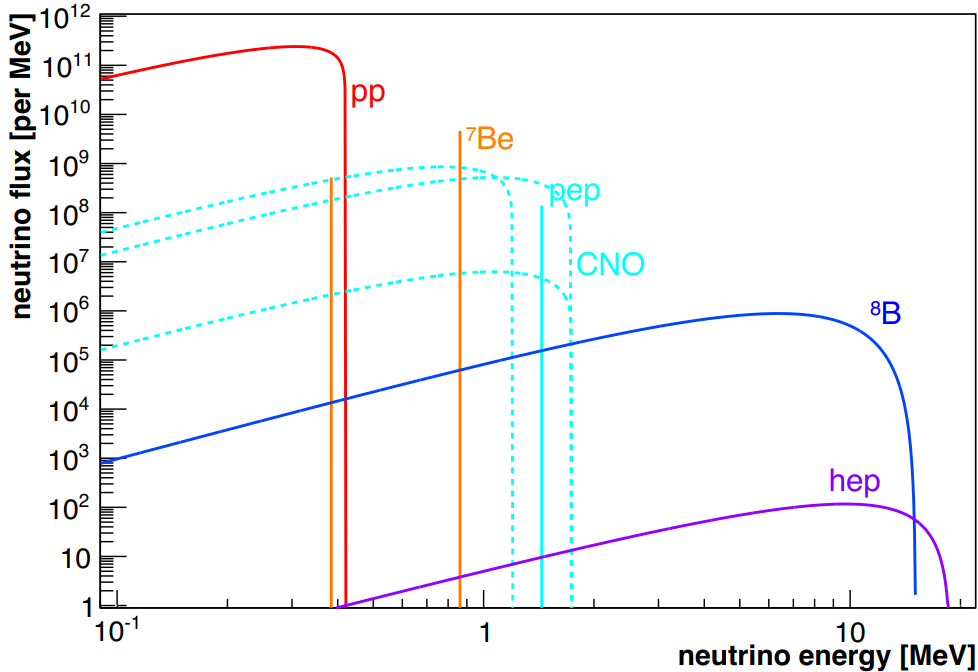

Figure 3.6: Solar neutrino spectrum with its various components, from [56] and [57]. Different fission processes in the sun like pep, pp, CNO, etc. lead to ν production, with differing energies.

3.2 Neutrinos

3.2.1 Solar neutrinos

Neutrinos coming from the Sun have been a cornerstone of neutrino physics, and many experiments have measured solar neutrino oscillation parameters. The Sun is a powerful source of neutrinos of energy $\sim 1\,\text{MeV}$ produced mainly from the pp process. Here, initially 4 protons combine into: $4p \rightarrow^4_2 He + 2e^- + 2\nu_e$. Neutrinos from production cycles in the Sun like pep and CNO (hitherto undetected) form a minor portion of the pp neutrino flux.

In consort with other neutrino experiments, solar neutrinos have provided ample evidence for neutrino oscillations. The study of solar neutrinos has formed an important part of astroparticle physics and solar physics. Besides testing of the Mikheyev-Smirnov-Wolfenstein (MSW) matter effect in particle physics, we can also improve significantly our knowledge of fundamental solar physics, such as the mechanism ruling the dynamics of the Sun, the solar metallicity problem, and the agreement between solar models and the data from helioseismology. JUNO aims to improve solar physics, solar dynamics, the metallicity problem, etc.

Source	Flux $\left(10^{10}\ \text{cm}^{-2}\text{s}^{-1}\right)$
pp	$5.95 \left(1.00^{+0.01}_{-0.01}\right)$
pep	$1.40 \times 10^{-2} \left(1.00^{+0.015}_{-0.015}\right)$
hep	9.3×10^{-7}
^{7}Be	$4.77 \times 10^{-1} \left(1.00^{+0.10}_{-0.10}\right)$
^{8}B	$5.05 \times 10^{-4} \left(1.00^{+0.20}_{-0.16}\right)$
^{13}N	$5.48 \times 10^{-2} \left(1.00^{+0.21}_{-0.17}\right)$
^{15}O	$4.80 \times 10^{-2} \left(1.00^{+0.25}_{-0.19}\right)$
^{17}F	$5.63 \times 10^{-4} \left(1.00^{+0.25}_{-0.25}\right)$

Table 3.2: The solar neutrino flux from the different interactions. The neutrinos from the decay of ^{13}N, ^{15}O and ^{17}F form the CNO neutrinos. From [55].

4

JUNO

JUNO (Jiangmen Underground Neutrino Observatory) is a multi-purpose neutrino detector currently under construction in Kaiping, China (Figure 4.1). JUNO was first proposed in 2008 with the main goal to pin down the neutrino mass hierarchy, which it plans to do within 6 years of data taking once operation commences. The determination of mass hierarchy requires it to be 53 km from the Yangjiang and Taishan NPPs (combined power of about 36 GW$_{th}$) which will provide JUNO with antineutrinos. The mass hierarchy determination requires equal baselines from the detector to all reactor cores to avoid cancellation of the oscillation dephasing effect. The JUNO detector has a target mass of 20 kton and will be deployed about 650 m beneath the Dashi hill, which will serve as its overburden and shield against cosmic showers. JUNO is designed to have an excellent energy resolution of $3\%/\sqrt{E\,(\mathrm{MeV})}$ so as to differentiate between the oscillation spectra of electron antineutrinos vis-à-vis normal and inverted mass hierarchies. Such a high energy resolution is a challenging proposition that entails stringent criteria for various properties of the photomultiplier tubes (PMTs) and the liquid scintillator used in JUNO. This also pertains to the production and investigation of the equipment which will be a part of the JUNO setup.
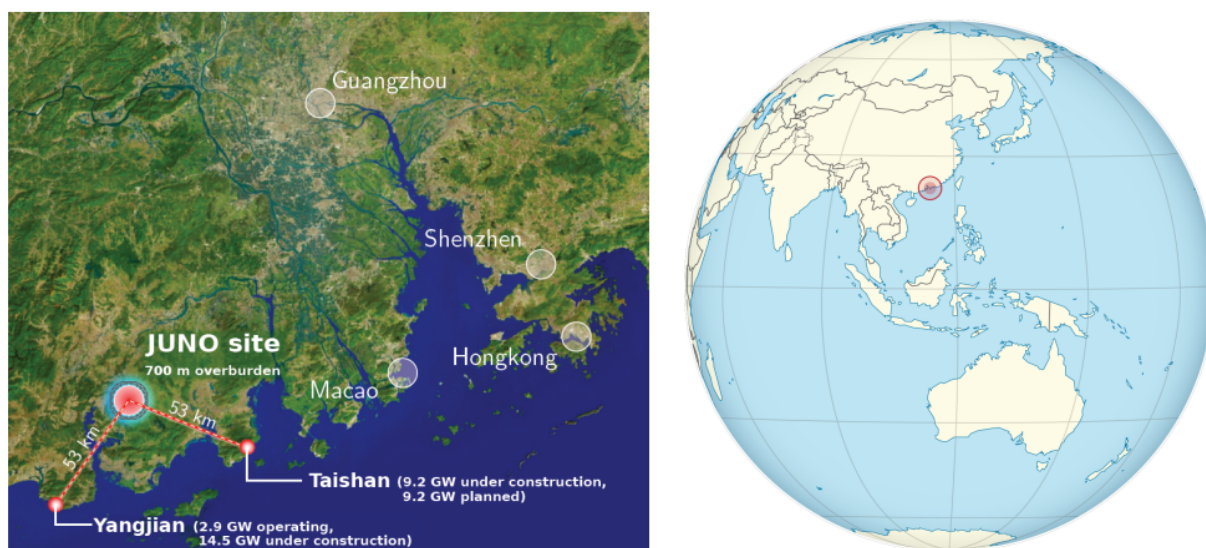

Figure 4.1: Location of the JUNO experiment in China.

4.1 The JUNO detector

The experimental setup of the JUNO detector consists of a central detector, a water pool surrounding it and a top tracker (for muons) above the central detector, as in Figure 4.2.

The central detector is submerged in the water pool to shield it from natural radioactivity originating from the surrounding rock and air. The PMTs lining it allow the water pool to serve as a Čerenkov muon veto.
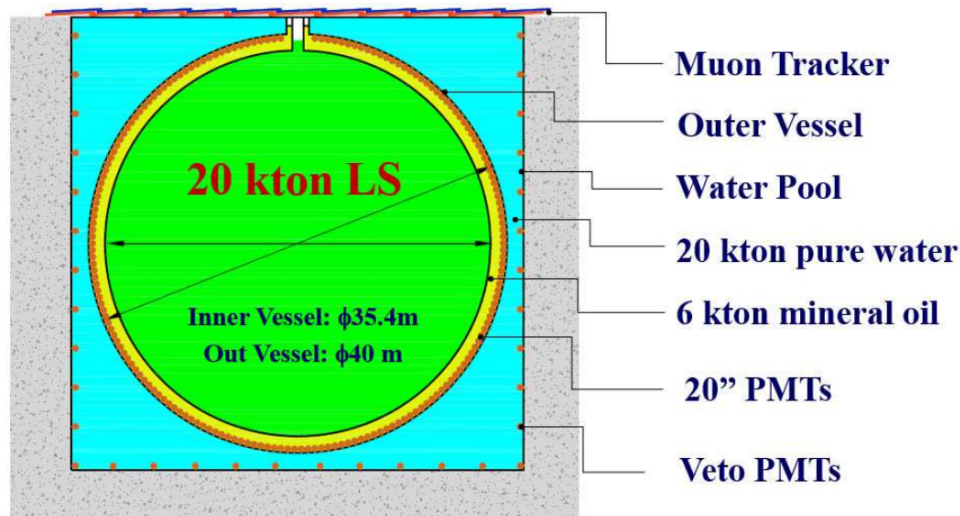

Figure 4.2: Setup of the JUNO detector.

The central detector

The central detector houses 20 kton of the liquid scintillator (LS) in an acrylic, spherical tank of 17.7 m radius. Incident particles interact with the LS such that the emitted scintillation photons are detected by PMTs on reaching the outer part of the central detector vessel. The LS cocktail consists of:

- LAB: Linear alkyl benzene, a mineral oil, which is the main solvent.

- PPO: 2,5 diphenyloxazole, which acts as the fluor and receives/transmits the scintillation light so that it is not re-absorbed by the LAB.

- bis-MSB: bis-Methyl styryl benzene, which acts as the wavelength shifter to increase the attenuation length of the scintillation light in the LS (22.4 m at a wavelength of 430 nm).

The spherical chamber is lined with about 18,000 20″ PMTs (which are the main eyes of JUNO) along with about 25,000 3″ PMTs, resulting in a 78% photo-cathode coverage. This contributes directly to the energy resolution goal that JUNO aims to reach. These PMTs are submerged in a water buffer at a radial distance of 19.5 m from the detector center, about 2 m away from the outermost region of the tank. This reduces the background contribution and the triggering rate in the LS due to radioactive elements in the PMT glass. The entire spherical vessel is supported by a steel truss, and submerged entirely in a cylindrical pool of ultra-pure water (Figure 4.3).

The veto detectors

An overburden of 650 m (about 2000 m.w.e) reduces the cosmic muons that impinge on the detector. The most prominent backgrounds come from the cosmic muons incident on JUNO. Muon interactions lead to the production of isotopes like ^{9}Li-^{8}He which mimic the antineutrino signal when they decay. The water pool (Figure 4.3) surrounding the central detector is lined with about 1,600 20″ PMTs to serve as a Čerenkov detector and veto incident muons. The muon detection efficiency of the water pool is expected to be 99.8% [17].

The top tracker above the JUNO detector setup is from the discontinued OPERA exper-
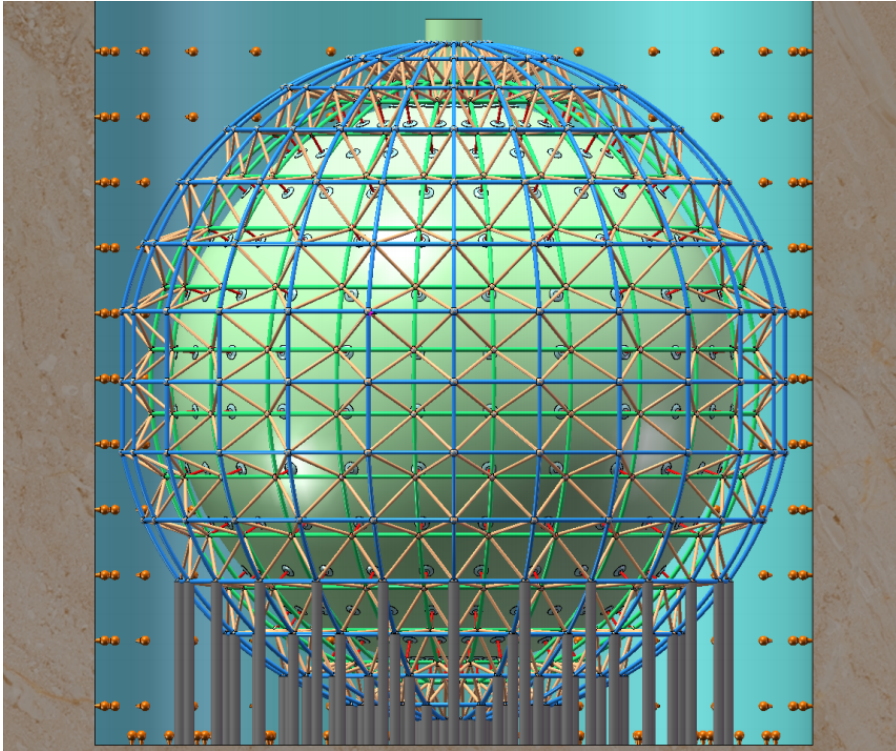
Figure 4.3: The water pool along with the PMTs lining it, surrounding the steel truss that supports the central detector, from [59].

iment [61]. Plastic scintillator strips from the erstwhile OPERA detector (Figure 4.4) will be re-purposed into modules to detect and tag incident cosmic muons. Each target tracker module will require at least 3 layers to sufficiently suppress the radioactivity background, which can induce extremely high noise rates in the detector. This radioactivity background is from the rock surrounding the experiment,formed by the U,Th and K decays in the vicinity and the activities of these radioactive elements are known (130, 113, and 1062 Bq/kg respectively). The entire top tracker layout covers about 25% of the surface area directly over the main detector.
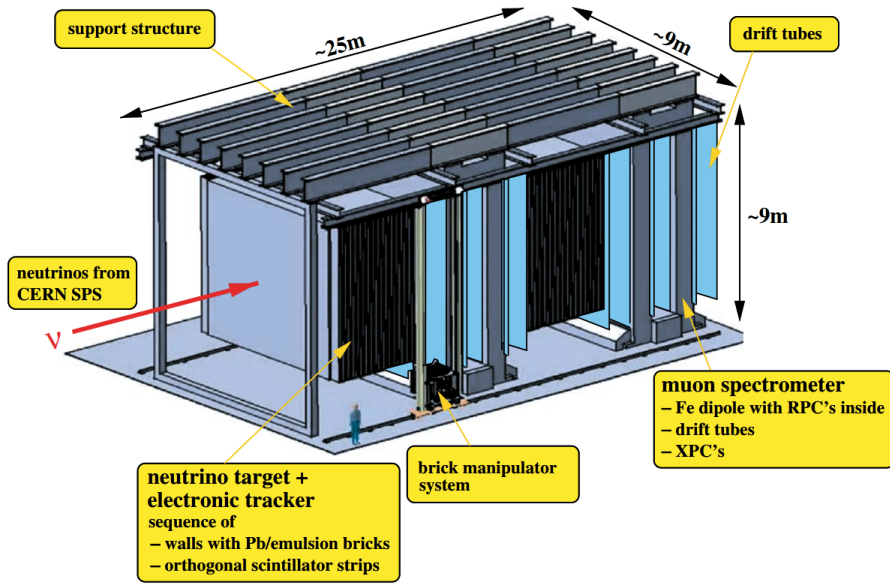
Figure 4.4: Schematics of the erstwhile OPERA detector, from [60].

4.2 PMT setup in JUNO

The PMTs are key components of JUNO, serving as its eyes and are thus directly related to the goals that JUNO aims to achieve. It is important that the approx. 20,000 PMTs used have high gain, low costs, large lifetimes, large area, large photon detection efficiencies, low noise and reliability. With $\sim$78% of the detector to be covered by PMTs, they will take up about 4,700 m^2 of the surface area of the detector sphere.

PMT Specifications

In Figure 4.1, we see some of the salient features that are required of a PMT for JUNO. The 20,000 PMTs that will be used in JUNO are comprised of:

- *MCP-PMTs:*
  About 15,000 of the PMTs used in JUNO will be multi-channel plate (MCP) PMTs (Figure 4.6).

- *Hamamatsu PMTs*:
  5,000 PMTs will be dynode PMTs, made by Hamamatsu (PMT type R12860).

Parameters	Specification(s)	Further comments
Diameter in mm	508	~ 20 inches
Photocathode diameter in mm	500	With glass thickness $4\,\text{mm}$
Peak quantum efficiency (QE)	$\geq 38\%$	Preferably at wavelength $\sim 420\,\text{nm}$
Photoelectron collection efficiency (PCE)	$\geq 93\%$	Averaged over the entire photocathode (i.e., the PMT)
Photon detection efficiency (PDE)	35%	$\text{PDE} \cong \text{QE} \times \text{PCE}$
Spectral response in nm	$300 - 650$	Scintillation from 380 to $550\,\text{nm}$
Transition time spread (TTS) in ns	5	Full width at half maximum (FWHM)
Gain	$> 10^7$	
Single photoelectron (pe) $\frac{Peak}{Valley}$ (P/V)	≥ 2	
Linear range (of a pe)	$0.1 - 1000$	
Dynamic range (pe)	$0.1 - 4000$	
Pre-pulse	$< 1\%$	
Fast after-pulse	$< 1\%$	$< 1\,\mu\text{s}$
Slow after-pulse	$< 5\%$	$< 200\,\mu\text{s}$
Maximum hydraulic pressure in atm	9	$4.2\,\text{atm}$ in JUNO
Fast after-pulse	$< 1\%$	$< 1\,\mu\text{s}$
^{238}U content in g/g	10^{-8}	PMT weight $\sim 1\,\text{kg}$
^{232}Th content in g/g	$2 \cdot 10^{-8}$	PMT weight $\sim 1\,\text{kg}$
^{40}K content in g/g	10^{-5}	PMT weight $\sim 1\,\text{kg}$
Lifetime of PMT in years	20	

Table 4.1: The specifications of a typical JUNO PMT. The typical dark noise pulse rate (or dark rate) for a PMT is $\sim 30\,\text{kHz}$, but in this work the dark rates of the PMTs have been uniquely assigned in order to investigate their effects. Data from [62].

In addition to these 20″ PMTs, JUNO will also use $\sim$25,000 3″ PMTs arranged between the larger PMTs. All in all, this arrangement bumps up the photo-cathode coverage to 78%.
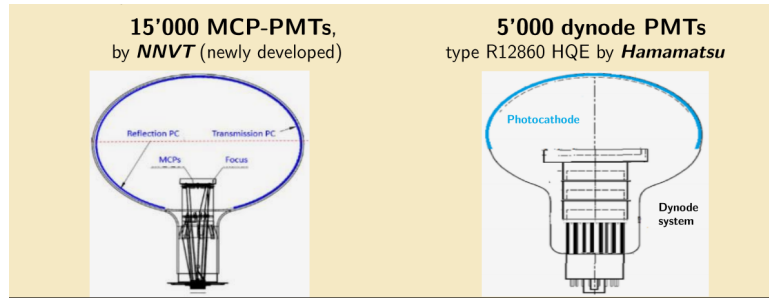
Figure 4.5: A cross sectional view of the two kinds of large PMTs used in JUNO: MCP-PMTs and Hamamatsu (dynode) PMTs. The difference in the internal architecture as well as the ellipsoidal glass of the photocathodes can be seen.

Figure 4.6: Various 20″ PMTs under test, and PMT testing systems set up in IHEP, Beijing; from [62].

PMT dark rates

The dark noise of a PMT is the signal it produces even during no optical stimulus (hence the word dark) i.e., even when there is no incident light. The dark noise comes from the PMT architecture, thermionic emission and field effects in the PMT due to ambient temperature and the electric voltage supplied to it. For JUNO's PMTs, the maximum permitted dark rates (of each PMT) are decided by the PMT type. For **Hamamatsu PMTs**, the maximum permitted dark rate is **50 kHz**. For **MCP-PMTs**, the maximum permitted dark rate is **100 kHz**. A PMT of either type that has higher dark rate than the imposed limit will not be used. All PMTs are tested (Figure 4.6) to check their properties at the site in Zhongshan, China. We will use the data from this testing facility to assign dark rates (in 7.3) to all the PMTs in JUNO, to investigate the effects of the dark noise.

5

Neutrino detection in JUNO

5.1 Antineutrinos

Reactor antineutrinos from the nearby fission reactors are detected in JUNO via the inverse beta decay (IBD). This interaction serves as the main constituent of the antineutrino signal, and is expected to help pin down the neutrino mass hierarchy. In an IBD interaction, an electron antineutrino incident on a proton produces a neutron and positron:

$$\bar{\nu}_e + p^+ \rightarrow n + e^+, \tag{5.1}$$

with the threshold energy $E_{threshold} = 1.8\,\text{MeV}$. So, for a $\bar{\nu}_e$ to participate in an IBD,

$$E_{\bar{\nu}_e} = E_{kin} + 1.8\,\text{MeV}. \tag{5.2}$$

The much lighter positron carries most of the kinetic energy E_{kin} of the original $\bar{\nu}_e$ after the collision, and goes on to interact with the LS. It quickly deposits this E_{kin} in the detector and annihilates with an electron (producing two $511\,\text{keV}$ γ's), with an overall energy

$$E_{prompt} = E_{kin} + E_{annihilation}\,, \tag{5.3}$$

which serves as the prompt energy.

The neutron moves about in the detector till it is thermalized. It is then captured on a proton after a delay of about $220\,\mu$s and releases energy $E_{delayed} = 2.2\,\text{MeV}$ in the form of γ's (binding energy of ^{1}He).

For reactor antineutrinos: The nuclear plants located $53\,\text{km}$ away from the JUNO detector ensure the maximum possible difference in the survival probability $P(\bar{\nu}_e \rightarrow \bar{\nu}_e)$ of the $\bar{\nu}_e$ dictated by either the inverted or normal mass hierarchy, as shown in Figure 5.1. The consequent signal seen at JUNO (oscillated and unoscillated) is shown in Figure 5.1 as well. **For geoneutrinos**: The expected geoneutrino signal at JUNO is shown in Figure 5.2 as well as the comparison between the reactor antineutrinos and geoneutrinos. The interaction mechanism for geoneutrinos is the same as that for reactor antineutrinos, which means that they are natural backgrounds to each other and the spectrum for each must be dealt with to analyze the other.
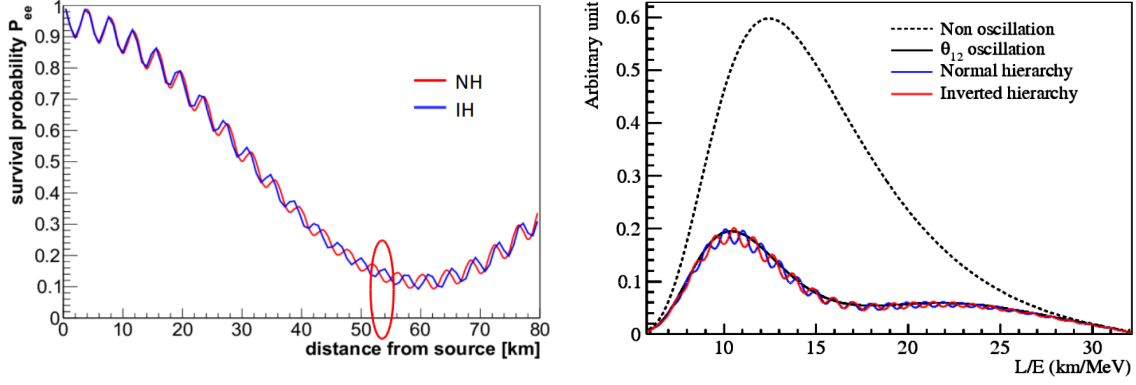
Figure 5.1: $P_{ee} \equiv P(\bar{\nu}_e \rightarrow \bar{\nu}_e)$ for reactor neutrinos as a function of the distance travelled in km by a $\bar{\nu}_e$. The red ellipse shows the area of interest caused by the θ_{12} oscillation, i.e, the maximum difference between the P_{ee} for both hierarchies, at $53\,\mathrm{km}$. The right plot shows the expected antineutrino spectrum in JUNO with spectral distortion for both possible mass hierarchies. Figures from [17].
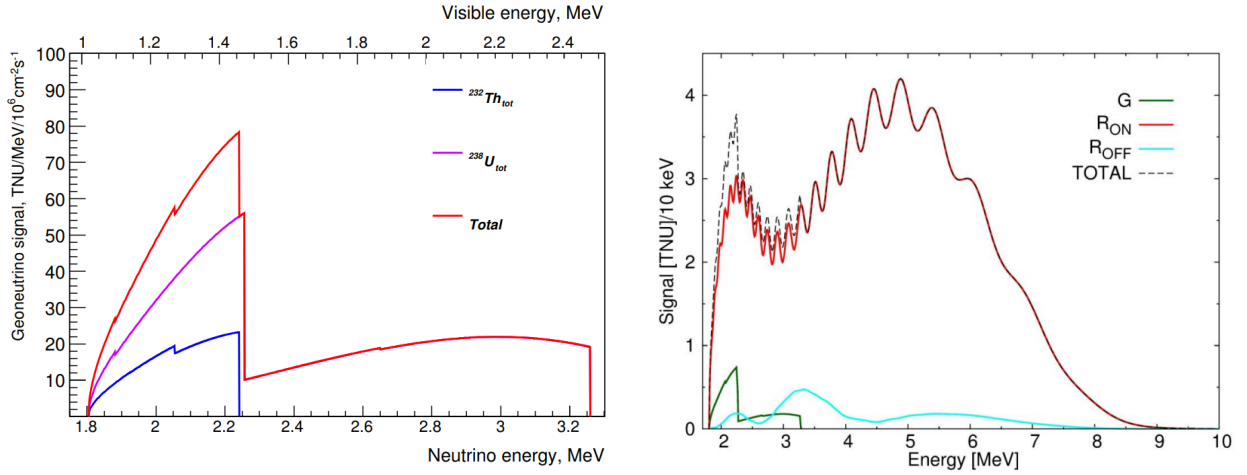

Figure 5.2: The expected geoneutrino IBD spectra from the U and Th chains assuming secular equilibrium in the chains and at the chondritic ratio of Th/U masses (M(Th)/M(U))=3.9, from [54]. The right plot shows the geoneutrino background and its effect on the IBD spectrum while the reactors are running (solid red line). For nearly no reactor antineutrinos, the solid light blue line shows the worldwide reactor antineutrino background for geoneutrinos, from [63].

5.2 Backgrounds for antineutrinos

The background profile in JUNO comes from three major sources:

- *Accidentals from radioactive decay of singles*: The decay of radioactive nuclei creating false signals in the detector can contribute to many accidental coincidences that contaminate the E_{prompt} and $E_{delayed}$ signal. The decay of radioactive nuclei in the detector can contribute to an accidentals rate of 7.6 counts/second, and we can have about 1.1

event/day (blue region in Figure 5.3) after all requisite cuts[1] are used.

- *Radioactivity arising from the decay of cosmogenic isotopes*: Cosmogenic isotopes, mainly ^{9}Li-^{8}He, undergo β decay and mimic the signal of IBD events. As these isotopes are sufficiently long-lived, they can travel some distances in the detector away from the cosmic muon interactions which produced them. This leads to about $340\,\bar{\nu}_e$-like events/day. This is reduced to <0.01/day after the cuts are implemented. The cosmogenic isotopes ^{9}Li-^{8}He (green region in Figure 5.3) are caused by cosmic muon spallation on ^{12}C, these do not decay very quickly[2] and may survive long enough in the detector (requiring a veto of $\sim 1-2\,$s) to give a false IBD signal. They are highly correlated to the IBD spectrum and have about the same number of events per day as IBD events: $\sim$84/day.
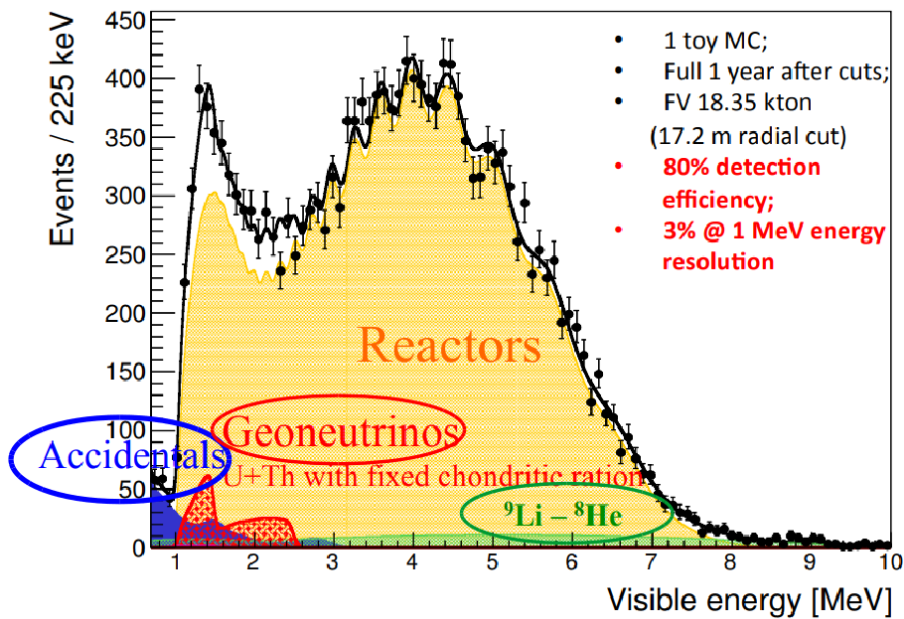
Figure 5.3: A 1 year MC simulation of IBD signal in JUNO, Accidentals, Geo-neutrinos and ^{9}Li-^{8}He. From [17].

- *Spallation neutrons*: The cosmic muons also produce hadron showers in the detector, leading to many spallation neutrons that go on to mimic the $E_{delayed}$. To deal with both, the cosmogenic isotopes and the spallation neutrons, JUNO employs certain cuts and vetoes. Spallation neutrons originate from hadron showers correlated to muons. The rate of spallation neutrons is negligible after cuts are applied along with the muon veto cut. The muon track is reconstructed and a cylindrical volume around it is vetoed for $\sim 1-2\,\mu$s following from the capture time.

Other sources are:

---

[1]Fiducial volume cut R$<$17 m, R$_{p-d}$ cut (distance between prompt and delayed signals) <1.5 m, ΔT (time elapsed between prompt and delayed signals) <1 ms, etc.

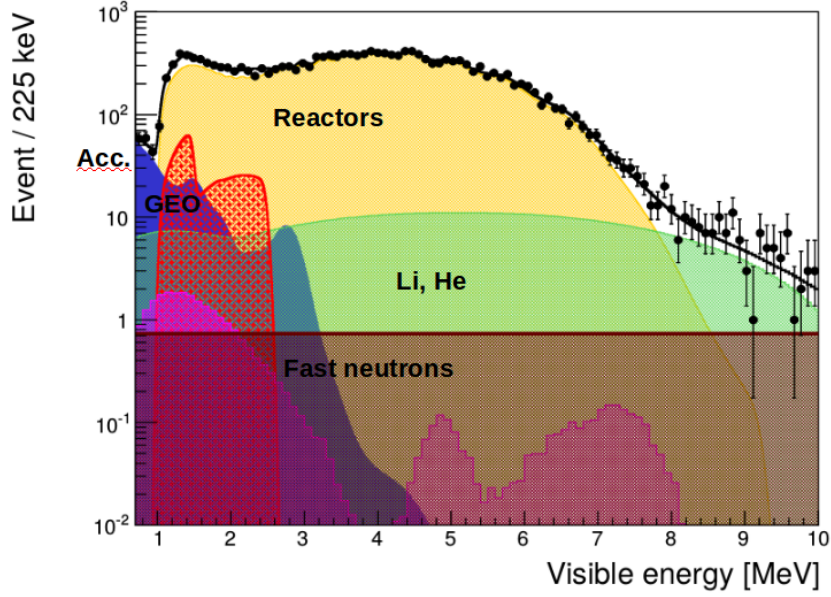[2]The half-lives of Li and He are: $t_{\frac{1}{2}}(^9$Li) = 178 ms and $t_{\frac{1}{2}}(^8$He) = 113 ms.

Figure 5.4: A logarithmic plot of the 1 year MC simulation, with mainly the lower backgrounds seen: fast neutrons (flat maroon region) and $^{13}C(\alpha, n)$ - ^{16}O (double-bumped pink region). From [17].

- *Fast neutrons*: These provide a constant, flat background to IBDs are highly energetic neutrons formed by incident, untagged, corner-clipping muons or from muons which which hit the detector in areas of low water shielding. In Figure 5.4, they are the maroon shaded region, with a rate of about 0.1/day.

- $^{13}C(\alpha, n)$ - ^{16}O: The $^{13}C(\alpha, n)$ - ^{16}O background comes from the reaction of α's from ^{235}U, ^{232}Th and ^{210}Po, which is out of equilibrium with the rest of the ^{235}U chain, on ^{13}C. The resulting ^{16}O can undergo de-excitation and is a correlated background for the IBD spectrum. The resulting ^{16}O can undergo de-excitation and result in a correlated background for IBD spectrum. After cuts, a rate of 0.05/day is expected. The pink shaded region in 5.4 illustrates this background.

- *Geoneutrinos*: These have the same interaction as reactor antineutrinos do, with contribution from ^{238}U (77%) and ^{232}Th (23%). The expected rate after cuts is about 1/day. In Figure 5.2, the solid green line (geoneutrino) clearly has an effect (dashed black line) on the pure IBD spectrum (solid red line).

5.3 Neutrinos

The main interaction for neutrinos in JUNO is elastic scattering on electrons, which comprises of a single flash of light from energy transferred to the electron from a neutrino:

$$\nu_{e,\mu,\tau} + e^- \rightarrow \nu_{e,\mu,\tau} + e^-. \tag{5.4}$$

For solar neutrinos: The large volume of JUNO ensures higher statistics, which will help solve the solar metallicity/opacity problem (measuring ^7Be and ^8Be), and discriminate among

various Standard Solar Models (SSM). Figure 5.6 illustrates the expected rates from various solar neutrino sources in JUNO, while Figure 5.5 shows the spectrum for elastic scattering of solar neutrinos with respect to the recoil energy from the scattering.
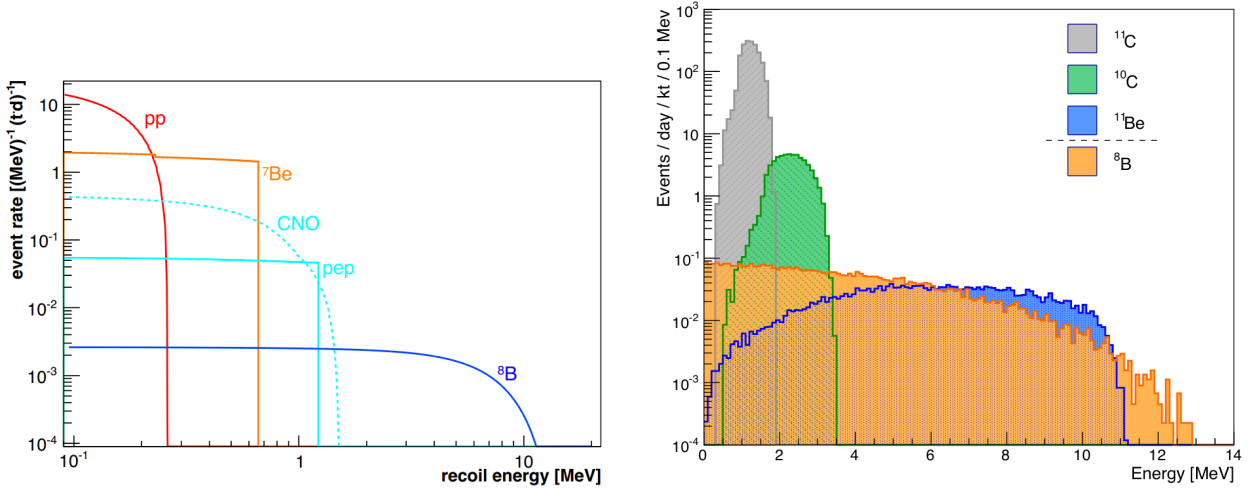

Figure 5.5: Solar neutrinos seen via the elastic scattering on electrons for the different neutrino sources in the Sun. The main signal contribution to the solar neutrino signal in JUNO comes from ^{8}B (if the threshold for IBD events is set at $1\,$MeV), from [56]. The expected solar neutrino spectrum, on the right, shows neutrino events from ^{8}B in JUNO with the main cosmogenic backgrounds: ^{11}C, ^{10}C and ^{11}Be. From [17].

Internal radiopurity requirements		
	baseline	ideal
^{210}Pb	5×10^{-24} [g/g]	1×10^{-24} [g/g]
^{85}Kr	500 [counts/day/kton]	100 [counts/day/kton]
^{238}U	1×10^{-16} [g/g]	1×10^{-17} [g/g]
^{232}Th	1×10^{-16} [g/g]	1×10^{-17} [g/g]
^{40}K	1×10^{-17} [g/g]	1×10^{-18} [g/g]
^{14}C	1×10^{-17} [g/g]	1×10^{-18} [g/g]
Cosmogenic background rates [counts/day/kton]		
^{11}C	1860	
^{10}C	35	
Solar neutrino signal rates [counts/day/kton]		
pp ν	1378	
^{7}Be ν	517	
pep ν	28	
^{8}B ν	4.5	
^{13}N/^{15}O/^{17}F ν	7.5/5.4/0.1	

Figure 5.6: The expected solar rates and the internal radiopurity levels required to see the solar neutrino events, from [17].

5.4 Backgrounds for neutrinos

The main sources of background to the measurement of solar neutrinos are dominated by cosmogenic isotopes and the internal radioactivity of the LS:

- *Cosmogenic isotopes*: The cosmogenic isotopes formed as spallation products of muons on ^{12}C like ^{10}C and ^{11}C, etc are sufficiently long lived in the detector. Their spectra needs careful investigation and subtraction from the overall spectrum. The neutrons produced along with the spallation products in a cosmic shower are an additional background, and could be used to suppress the ^{10}C, ^{11}C background with counts of $\sim$1300 and $\sim$30/day/kton respectively (Figure 5.6). The ^{11}Be background (2 counts/day/kton) is also important for ^{8}B. The rather large decay time of these isotopes means that they cannot be subtracted successfully along their parent muon track; an investigation of their spectra and rates is required before subtracting from the solar neutrino spectrum. See Figure 5.5.

- *Singles from internal radioactivity*: Radioactivity from the decay of nuclei can mimic the elastic scattering energy. The baseline i.e. the maximum permitted radiopurity of certain elements like ^{210}Bi, ^{85}Kr, ^{238}U, etc. is strictly set. The singles spectra is comprised of only β- and γ-decays, with non-negligible contributions to the background coming from ^{210}Pb, ^{85}Kr, ^{238}U and ^{40}K. The 2.6 MeV γ's coming from the decay of ^{208}Tl (in the PMT glass and from ^{232}Th contamination in LS) are a background for ^{8}B neutrinos.

Other sources of background which are not studied here include the external γ's; these can be reduced with a fiducial volume cut. Solar neutrinos have high enough statistics to look in the innermost (and cleaner) region of detector, where the only background is due to the contamination of singles in the LS. The rate of ES interactions from reactor $\bar{\nu}_e$ is $\sim$0.5/day/kton, which makes it $\sim$5% of ^{8}B signal. These can be statistically subtracted with high precision from IBD measurements.
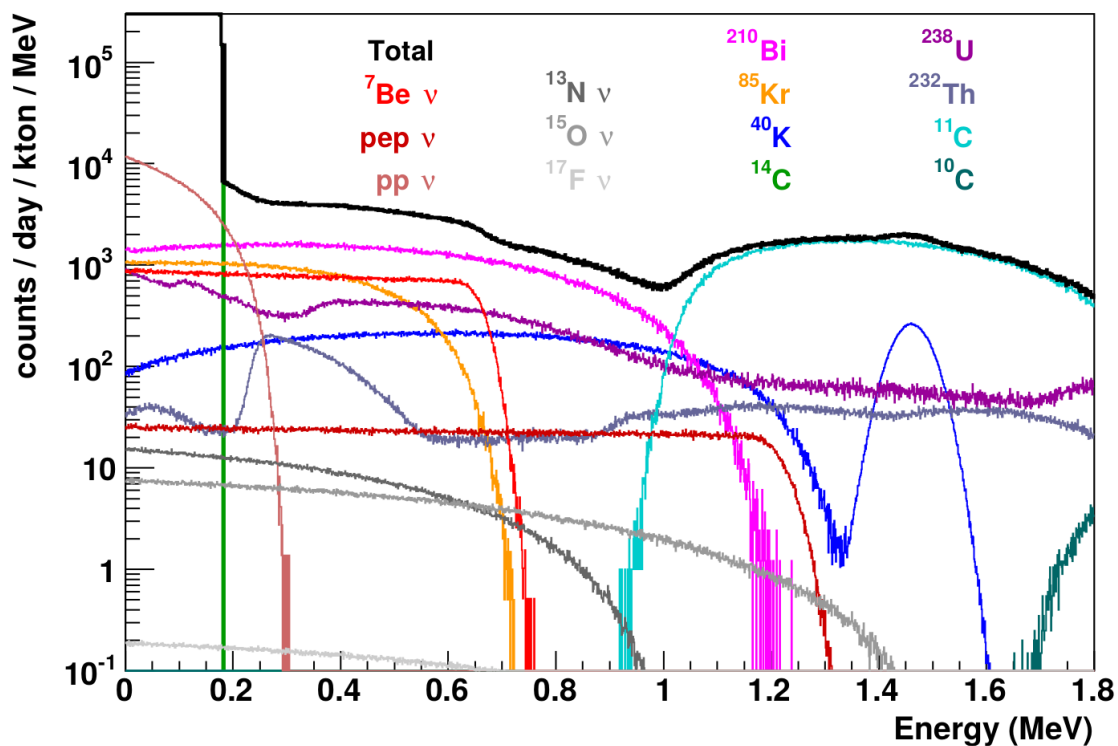
Figure 5.7: Spectra of radioactivity from different nuclides with "ideal" radiopurity levels (in Figure 5.6), from [17]. A further analysis of the spectra of internal radioactivity, carried out in this work, can be seen in Figures 8.8 and 8.9.

6

Physics goals of JUNO

The large mass (20 ktons) and the excellent energy resolution, 3% at 1 MeV, along with an accurate energy determination (better than 1%) will allow JUNO to probe various sections in neutrino physics and answer some of the open questions therein. In this section we discuss some of the main goals of JUNO and the corresponding methods of their determination.

6.1 Determining neutrino mass hierarchy

Pinning down the neutrino mass hierarchy, which is the main goal of JUNO, uses the reactor antineutrino signal. The $\bar{\nu}_e$'s from the Yangjiang and Taishan nuclear fission plants dominate the antineutrino signal in JUNO. To discern between the two possible alternatives for the mass hierarchy, i.e, the normal or inverted hierarchy, we recall the antineutrino survival probability $P(\bar{\nu}_e \to \bar{\nu}_e)$ from 2.12, rewriting it as:

$$P(\bar{\nu}_e \to \bar{\nu}_e) = 1 - \sin^2 2\theta_{13} \left(c_{12}^2 \sin^2 \Delta_{31} + s_{12}^2 \sin^2 \Delta_{32} \right)$$
$$- c_{13}^4 \sin^2 \theta_{12} \sin^2 \Delta_{21} \tag{6.1}$$
$$= 1 - \frac{1}{2} \sin^2 2\theta_{13} \left[1 - \sqrt{1 - \sin^2 2\theta_{12} \sin^2 \Delta_{21}} \right] \cos(|\Delta_{ee}| \pm \phi)$$
$$- c_{13}^4 \sin^2 \theta_{12} \sin^2 \Delta_{21} , \tag{6.2}$$

where $c_{ij}, s_{ij} = \cos \theta_{ij}, \sin \theta_{ij}$ respectively, $\Delta_{ij} = \Delta m_{ij}^2 L/(4E)$, L is the baseline/distance travelled by the antineutrino (between the point of creation and point of possible detection) and E is the antineutrino energy. The phase ϕ can be defined as:

$$\sin \phi = \frac{c_{12}^2 \sin \left(2s_{12}^2 \Delta_{21} \right) - s_{12}^2 \left(2s_{12}^2 \Delta_{21} \right)}{\sqrt{1 - \sin^2 2\theta_{21} \sin^2 \Delta_{21}}} \tag{6.3}$$

$$\cos \phi = \frac{c_{12}^2 \sin \left(2s_{12}^2 \Delta_{21} \right) + s_{12}^2 \left(2s_{12}^2 \Delta_{21} \right)}{\sqrt{1 - \sin^2 2\theta_{21} \sin^2 \Delta_{21}}} , \tag{6.4}$$

and $\Delta m_{ee}^2 = c_{12}^2 \Delta m_{31}^2 + s_{12}^2 \Delta m_{32}^2$. The $\pm$ in 6.2 refers to the mass hierarchies: (+) for the normal and (-) for the inverted hierarchy. In JUNO, which is a medium baseline experiment, the oscillation in Δm_{ee}^2 show up as multiple cycles in the spectrum (depending on the hierarchy), seen in Figure 5.1. Figure 6.1 shows the baseline dependence of of the extra effective mass-squared difference

$$\Delta m_\phi^2 = \frac{4E\phi}{L} . \tag{6.5}$$

The effective mass squared difference for NH (normal hierarchy) will be $2|\Delta m_{ee}^2| + \Delta m_\phi^2$ while for IH (inverted hierarchy) it will be $2|\Delta m_{ee}^2| - \Delta m_\phi^2$; this will cause an advancement
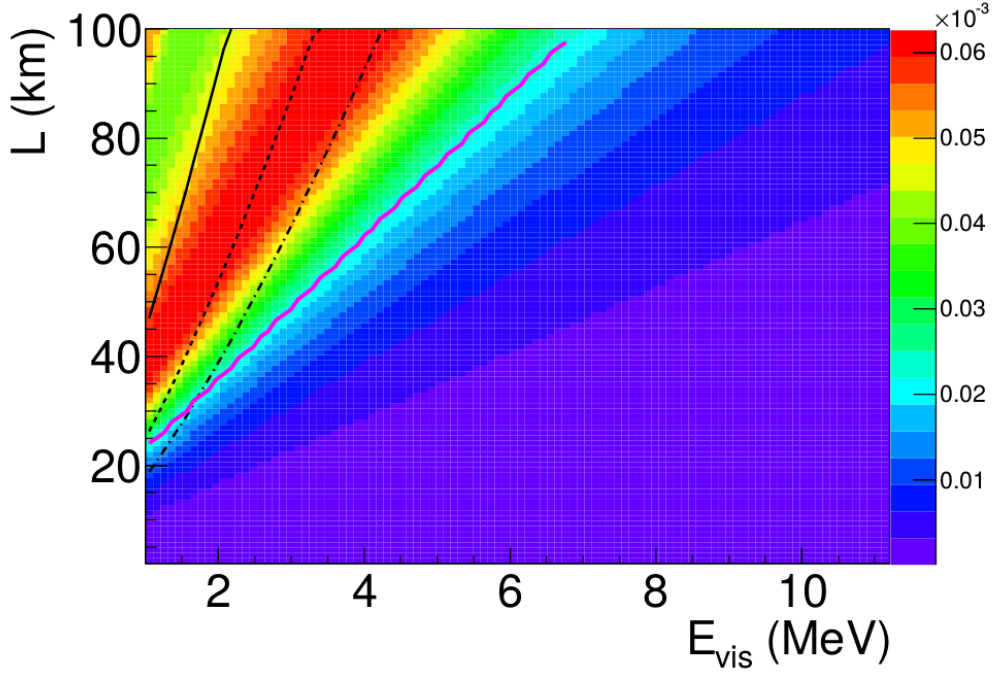
Figure 6.1: The change in Δm_ϕ^2 (coloured bands) for different baselines and $E_{vis} = E_{\bar{\nu}_e} - 0.8\,\text{MeV}$. The solid purple line represents the approximate boundary of the degenerate mass squared difference. The solid, dashed and dotted line indicate an energy resolution of 2.8%, 5% and 8% respectively.

or retardation in the spectrum and can be used to discern the mass hierarchy. To do this successfully, a large number of events ($O(10^5)$ IBD events from reactor antineutrinos) need to be detected, and an energy resolution of 3% (at 1 MeV) is needed. The energy scale of JUNO must be better than 1% as well, to extract the required information from the spectral distortion.

6.2   Precision measurements

Solar neutrino oscillation parameters

JUNO aims to measure the solar neutrino oscillation parameters ($\sin^2\theta_{12}, \Delta m_{12}^2$) with 1% precision. This precision measurement is carried out with the spectrum of reactor antineutrinos $\bar{\nu}_e$ from the fission reactors close to JUNO. The dominant dip in the IBD spectrum in Figure 5.1 is due to the solar oscillation parameters.
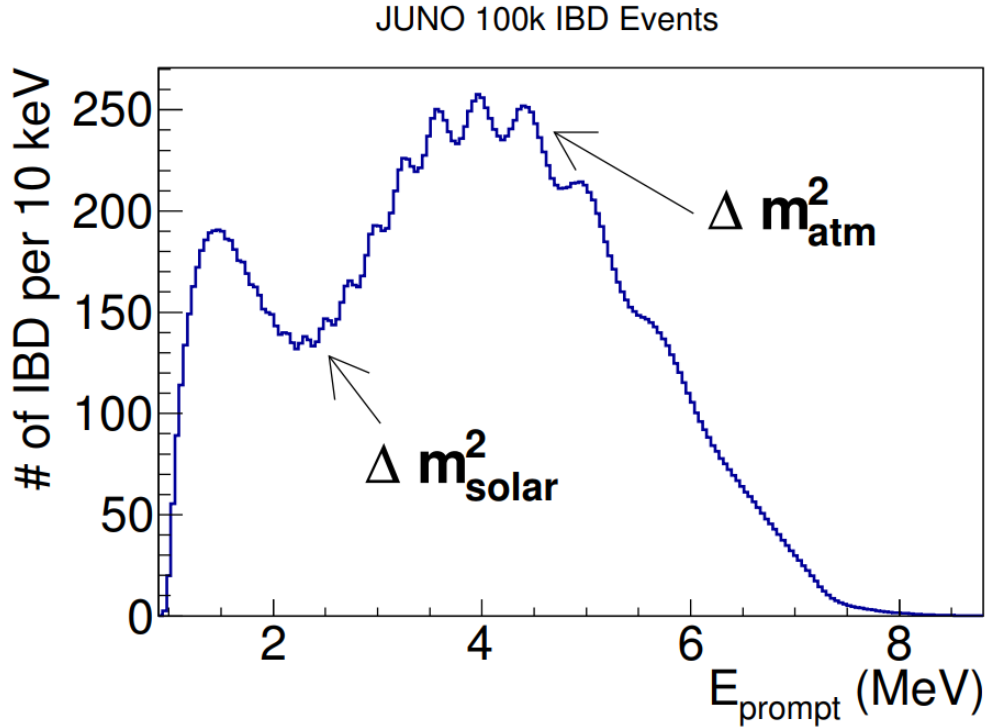
Figure 6.2: Spectrum of 6 years worth of data-taking in JUNO, which is expected to be approximately 100,000 Inverse beta decay (IBD) events from fission reactor-sourced electron antineutrinos. The dominant oscillation in the spectrum, due to $\Delta m^2_{solar} = \Delta m^2_{21}$, is appended by the oscillations due to Δm^2_{atm} as shown. The x-axis is the prompt energy $E_{prompt} = E_{\bar{\nu}_e} - 0.8\,\text{MeV}$. From [17].

Optimization of the trigger time window

7.1 Introduction

In order to fully understand and investigate JUNO's response to low-energy events, it is imperative to view the detector setup in terms of a few parameters, i.e. to now see the detector response in terms of the change registered with respect to these parameters. The foundation of any such an investigation is an analysis of the collected photons, or the hits in the PMTs. The successful collection of photons from an event requires a sufficient data acquisition time window, which is 1250 ns in JUNO, after the decision to trigger has been made. This decision is made within a so-called trigger decision window or trigger window. In order to optimize this duration, the location of events and event energies has to be taken into account. For events with energy ≤ 1 MeV, the investigation is carried out with the continuous background of the dark hits in the PMTs. Such events, which come for example from the elastic scattering of solar neutrinos, are simulated and studied with regard to a choice of analysis parameters. The main idea is to understand the minimum energy that an event requires in order for it to be successfully triggered; this involves the optimization of the trigger time window and trigger condition to achieve the lowest possible threshold energy with respect to dark noise.

7.2 Analysis parameters

The choice of analysis parameters is governed by some salient features of the detector. The main ones include:

- *Time of flight*:
  The photons emitted from an event or an interaction do not always travel the same distance through the detector; the location of the event within the detector differs for each event. For the extreme case, a photon will require ~175 ns to travel from one end of the detector to another.

- *Adequate trigger window*:
  The trigger window for a PMT is the duration of time that it counts event hits for, once it has observed a photon, in order to make a trigger decision. As photons can take up to ~175 ns to travel the entire detector, any trigger window < 200 ns is at risk of collecting inadequate photons to make a trigger decision.

- *Detected photons*:
  Once the photons have reached the PMTs, their successful detection depends on PMT occupancy. This is expected to effect the collection of photons from events very close

to the detector edge, which will travel a relatively minuscule distance to the closest PMTs. A large number of photons incident on the PMT almost simultaneously can lead to inefficient collection of the photons.

The differences in the detector response for events further from the radially arranged PMTs motivates the simulation of radially distributed events in the detector. Effects hampering the collection of photons near the edge of the spherical tank can be visualized with a radial distribution of events. Such effects include total internal reflection (TIR) at the boundary of the LS-acrylic sphere-water setup and the reduction in the number of hits (for border events) registered due to the aforementioned PMT occupancy. To facilitate a trigger condition and optimize the trigger window, two analysis parameters can thus be defined to study the detector response:

- *Shells*:
  The spherical detector (of radius 17.7 m) can be split up into 17 concentric and equidistant shells. The distance between any two consecutive shells is 1 m and each shell is 0.05 m thick. Events originating from different shells can be studied for the difference in the responses.

- *Trigger windows*:
  The detector response for trigger decisions can be studied for various lengths of the trigger decision window, i.e., the trigger window. We start with 200 ns and go up to 350 ns in steps of 50 ns to see the change in the response.

7.3 Assigning dark rates

In the context of the studies undertaken here, the only background considered is the dark noise from the PMTs and nothing else. We investigate the effect of th 17,738 PMTs lining the detector with their different dark rates, which differ from PMT to PMT. The data pertaining to the dark rates of ∼1300 PMTs of both types (Figure 7.1) from the testing site is used to recreate a realistic version of dark noise in JUNO. This includes both, the Hamamatsu and the MCP PMTs. The data in Figure 7.1 is used to assign a dark rate to 5,000 Hamamatsu PMTs and 12,738 MCP PMTs respectively (shown in Figure 7.2), which will cover the spherical detector.
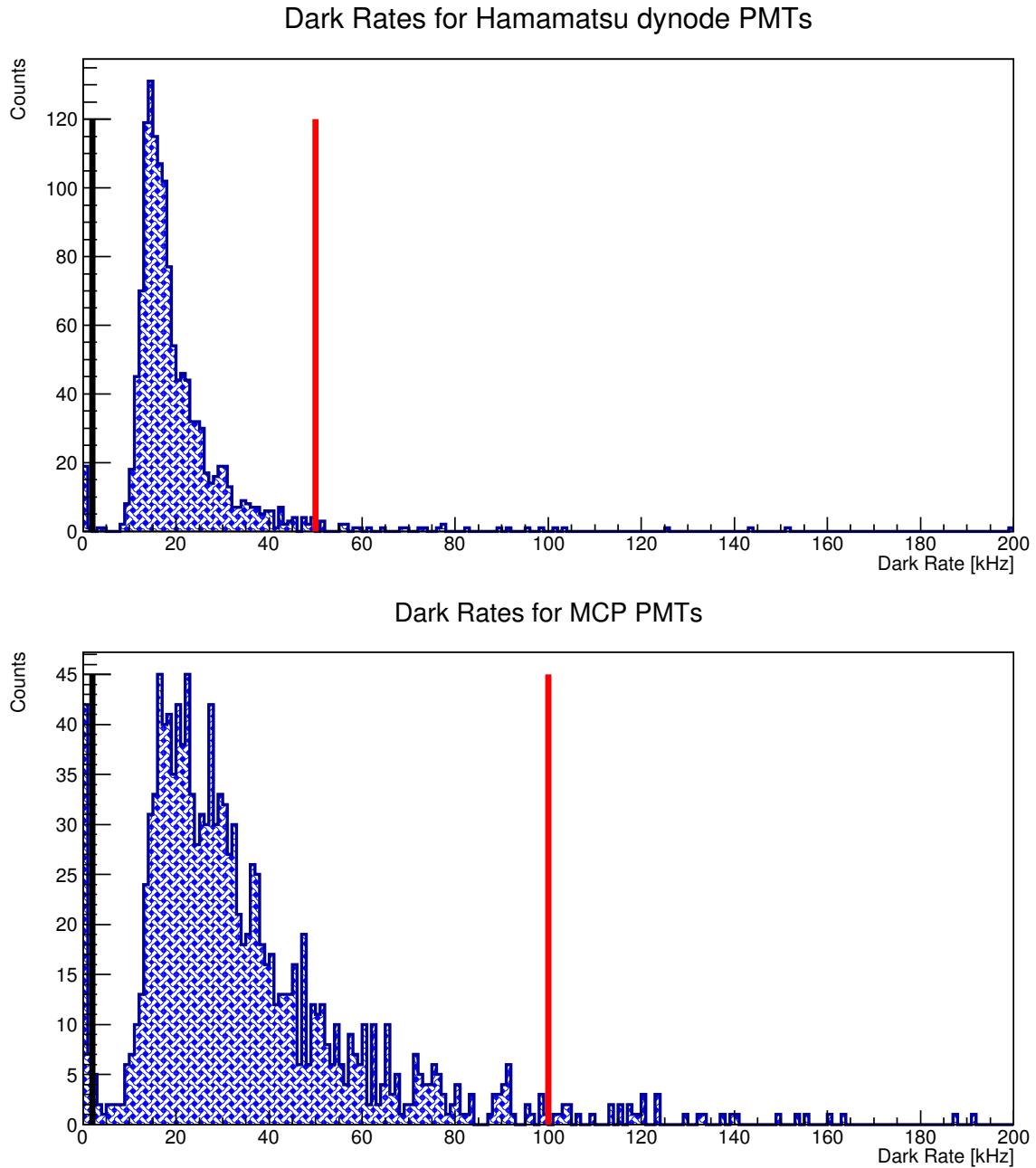
Figure 7.1: These histograms are the dark rates of 1319 Hamamatsu and 1306 MCP PMTs respectively, with data as received from Zhongshan PMT testing site, China. The red line in each histogram is the limit imposed on the dark rate for each type of PMT, while the black line is the starting point of the dark rate data without the theoretically inconsistent peak at ∼0 kHz in each histogram. The range between these lines represents the dark rates used for each PMT type to recreate and assign the dark rates of JUNO's PMTs. *Figures and data received with thanks, from Michaela Schever.*

Dark Rates (Hamamatsu PMT)
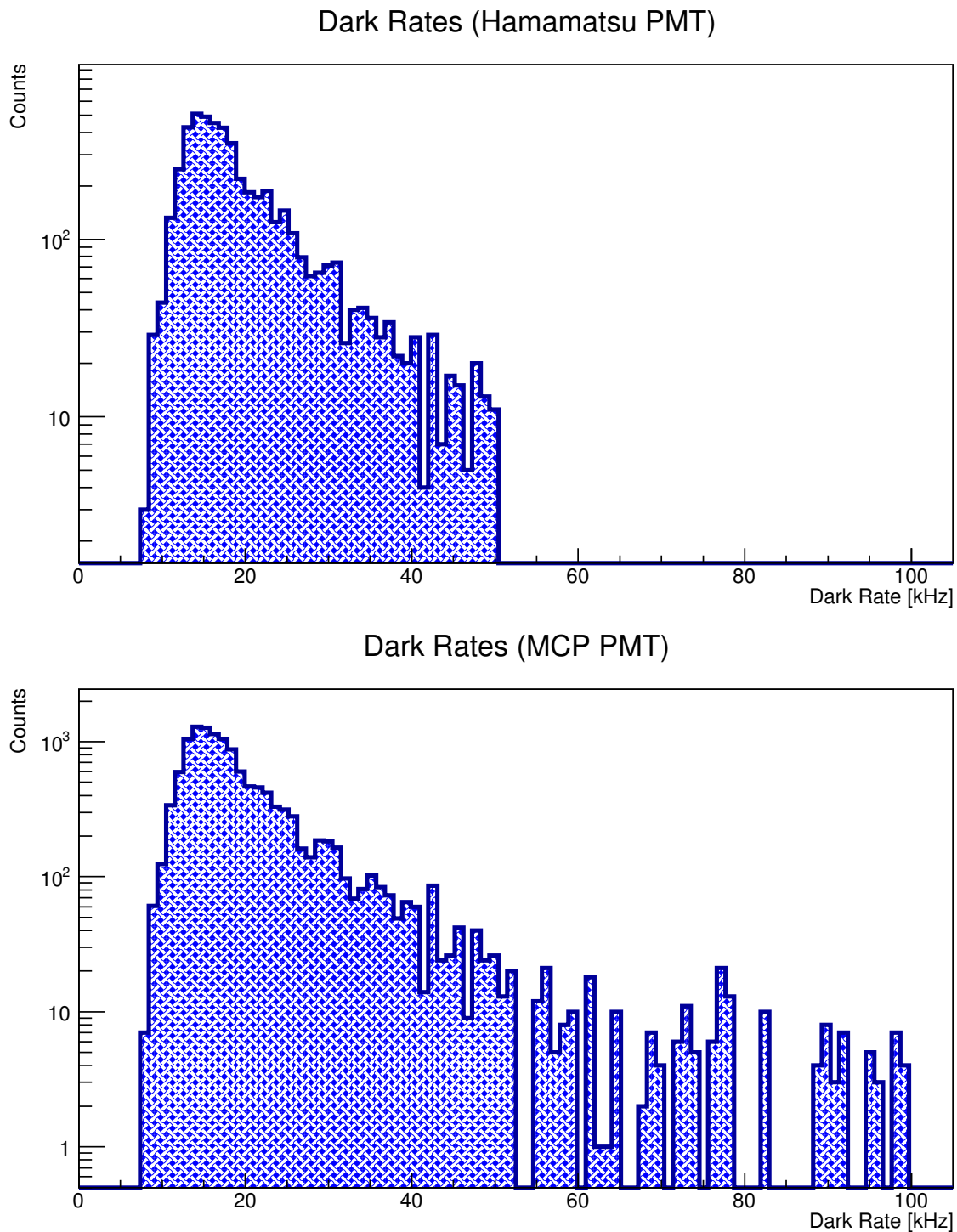
Dark Rates (MCP PMT)

Figure 7.2: The dark rates for 5,000 Hamamatsu PMTs and 12,738 MCP PMTs used in simulations are these distributions respectively. An overall mean dark rate of $\sim$20 kHz is obtained.

7.4 The Monte Carlo dataset

Event Generation: The studies comprising this work are analyses of Monte Carlo-generated data. The generation of events in the JUNO detector and any subsequent steps undertaken to facilitate and complete the analyses are mentioned here in brevity. To generate the events and electronic response of the detector setup, the JUNO offline is used. This part of the offline is the DetSim (detector simulation) package which contains GEANT4 based software specifically tailored for JUNO. The primary step to obtain a usable dataset is the generation of events using DetSim. These can be generated for a choice of particle types, such as electrons and positrons (depending on event type) or for neutrinos from various sources. The constituent package *nusol*, for e.g., is used to generate the solar neutrino events in JUNO for the different possible origins of the solar neutrinos - the pp process, ^{7}Be, etc. A similar treatment with the *sn* package can be used for supernova neutrinos. The generation of electron events (with the *gun* package) can be chosen for various energies, and various event vertices in the detector, as will be implemented in this study. Other backgrounds in the detector like the radioactive decay of unstable singles in the LS like ^{14}C and ^{210}Po (which originate false positives in (α, n) interactions) are also generated using the *gendecay* package. The output of this step contains no data regarding the response of the detector's electronics to the event; this is seen with the Electronic Simulation (ElecSim) package.

Electronic simulation: The DetSim generated data is processed using ElecSim. The various options in ElecSim provide the tools required to modify (or in some cases, deactivate) the readout and data acquisition of JUNO. Such properties include the trigger decision window (trigger window), the readout window, the average dark rate of all the PMTs, etc. These properties, on tuning, can generate different datasets using the same input from the DetSim data. The different settings of the properties in ElecSim also include the mixing of events, which can then be used to generate the pileup of two or more event types, etc. The output of the electronic simulation of JUNO can be modified with the programs which generate the PMT behaviour. This forms an essential part of the work undertaken in the following sections. The generation of dark noise pulses follows from the utilization of the unique dark rates which we have assigned (for all the PMTs). This is done by making modifications to the PMT simulation algorithm (PMTSimAlg). A further step undertaken to facilitate data generation involves the triggering algorithm (PreTrgAlg). A modification in this can directly provide the number of hits per event, and subsequently offer this as an output ready for further analysis.

Final Statistics: For each combination of parameters from Table 7.1, a set of 1,000 low-energy electron events are generated to be used. The resulting values of number of hits registered in the detector, event by event, is then analyzed to recreate the apposite histograms, some of which are shown in this section. The utilization of these parameters is further discussed in the following section.

Table 7.1: Combinations of analysis parameters

Trigger windows (ns)	Shells	Energies (MeV)
200	0	0.1
250	1	0.2
300	. . .	. . .
350	17	0.9

7.5 Shells and trigger windows

With the analysis parameters (shells and trigger windows) in hand, we can study a range of low energy events. For events below 1 MeV, Table 7.1 shows the studied combinations of analysis parameters and event energies - a total of 648 combinations. For each combination of shell/trigger window/event energy, a histogram can be made for the *number of hits* in the PMTs due to an event. Figure 7.3 are two such examples, where the difference in the two peaks featured in each depends on the combination of Shell/Trigger window/Energy. The two separate peaks in both these histograms come from disparate sources - the peak to the left is due to the dark noise, while the peak on the right is due to event hits as well as dark noise.
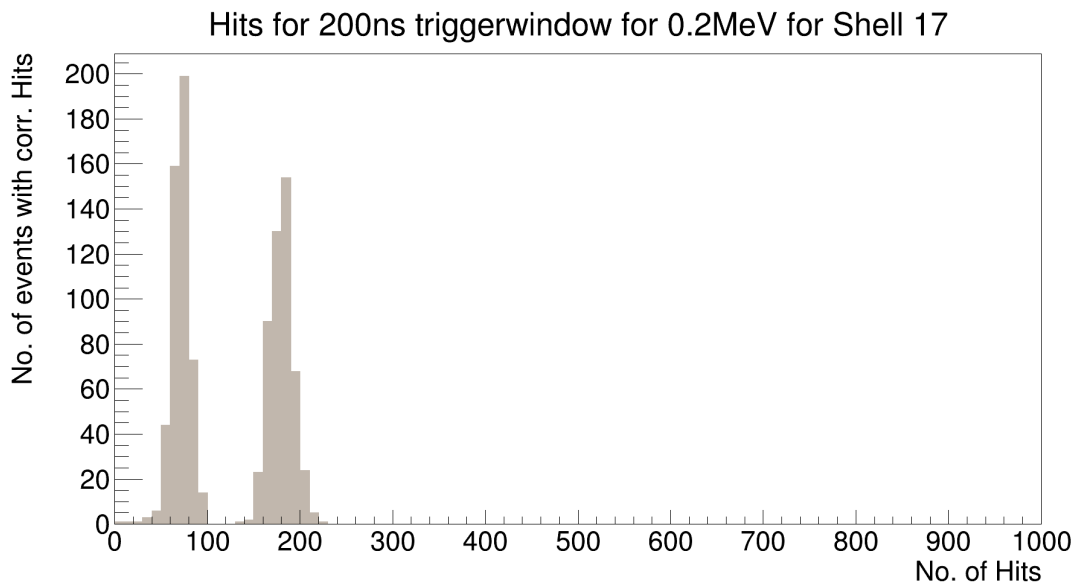
Figure 7.3: The above figure shows the difference in the number of hits (number of photons incident on PMTs from an event or dark noise).
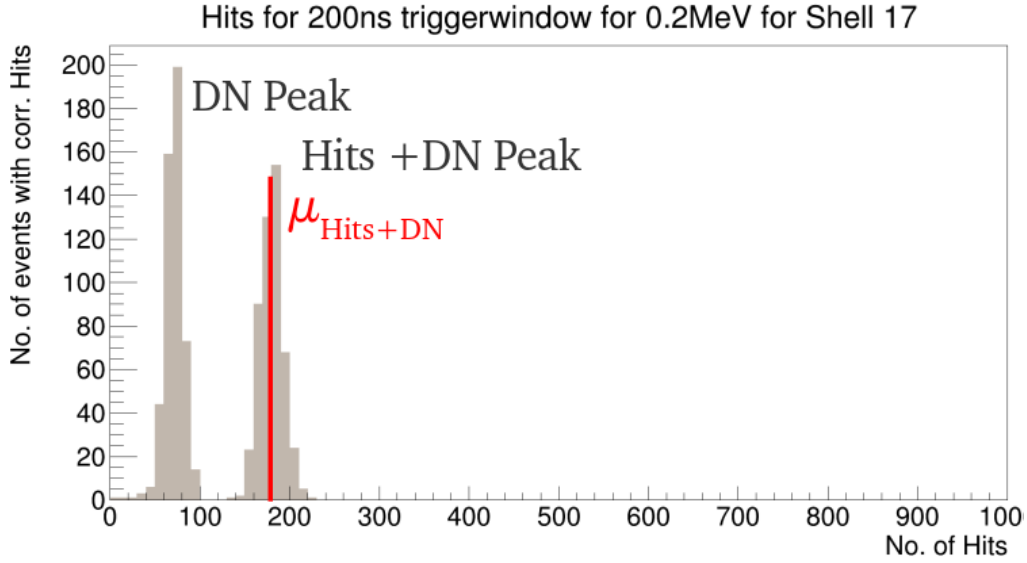
Figure 7.4: Illustration of Figure 7.3 with the peaks labelled: *DN peak* is the peak in the histogram due to dark noise and *Hits + DN peak* is the second peak due to hits from the event and dark noise. The red line is the mean of the *Hits + DN peak* ($\mu_{\text{Hits + DN}}$) once a Gaussian function has been fitted to it. For 200 ns, the DN peak has mean at $\sim$70 hits.

Trigger window (ns)	Hits due to dark noise (Mean value)
200	71
250	87
300	106
350	125

Table 7.2: Number of hits due to dark noise, for the different trigger windows.

Table 7.2 gives a general idea regarding the dark hits one can expect in JUNO in a certain trigger window. When the twin peaks in the histograms of Figure 7.3 are fitted with a Gaussian function, the mean values of each peak can be found. Table 7.2 summarizes the possible values of the left-most peak, which is the peak due to dark noise hits. The change in the mean values of the right-most peak (i.e. peak due to event hits as well as dark noise) can be further investigated.

Event hits: Detector trends

The mean values of each of the "Event hits + Dark Noise hits" peaks (right-most peak in Figure 7.3) for different shells and trigger windows can be used to view the consequent trends in the detector response, as seen in Figures 7.5 and 7.6. For events located in shells 8 to 12, there is a marked decrease in the mean values of "Event and dark noise" hits. This dip
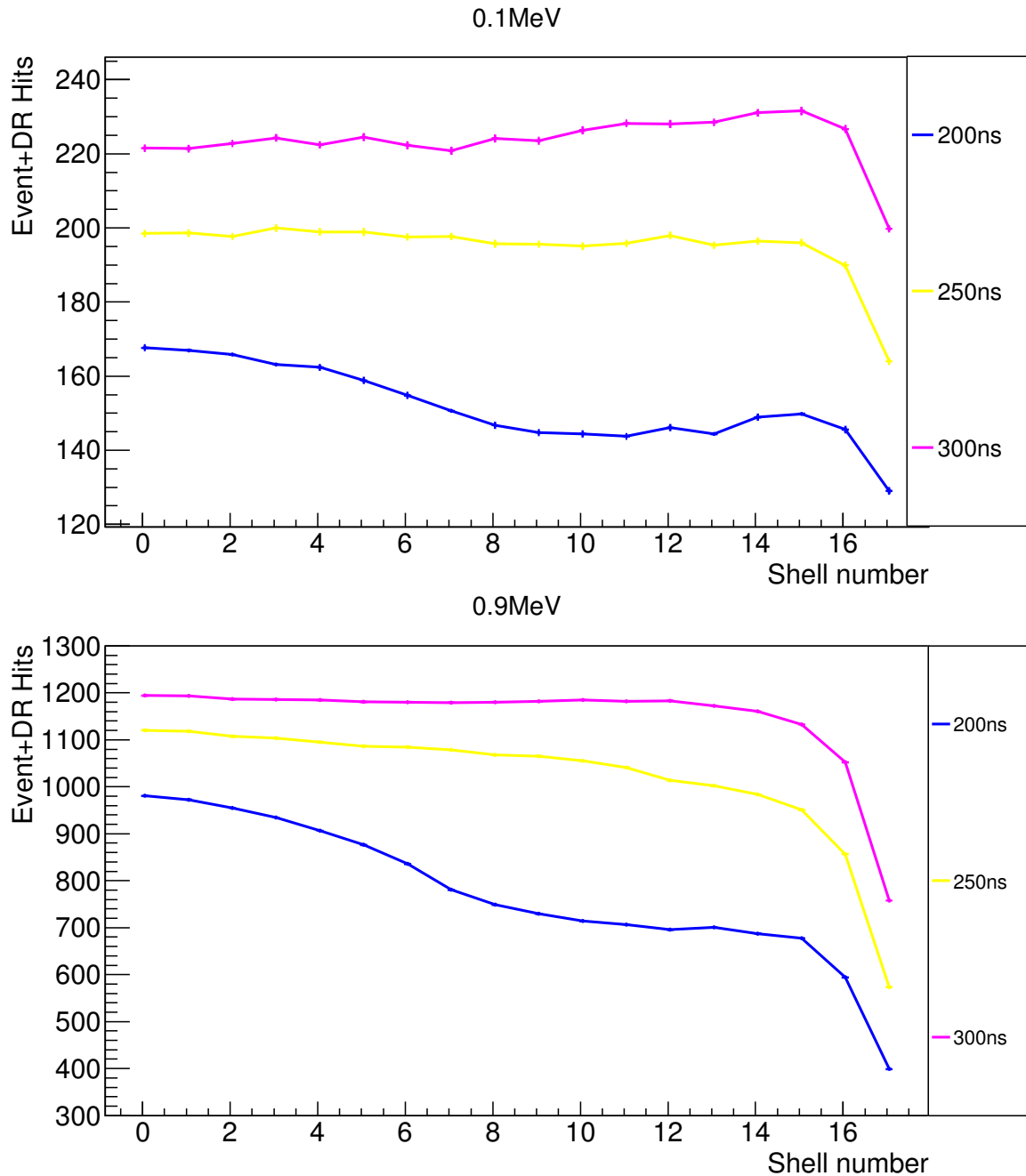
Figure 7.5: For 0.1 MeV events, the mean values for the "Event and dark noise" hits are shown with respect to shell number, moving from the center to the outermost part of the detector. As the trigger window is increased from 200 ns to 300 ns, the decrease in the mean values (*dip*) at shells 8 to 12 is slowly remedied. The same happens for 0.9 MeV events as well; only for 300 ns is this *dip* fully removed.

is caused by the inadequate trigger window of 200 ns which is too little for all the photons emitted from an event[1] to reach the PMTs; some travel lesser distances than others and reach the PMTs quicker. It is noted that only for a choice of 300 ns (as a trigger window) do we have a homogeneous treatment of all shells in the detector.

---

[1] Photons from an event are emitted isotropically.
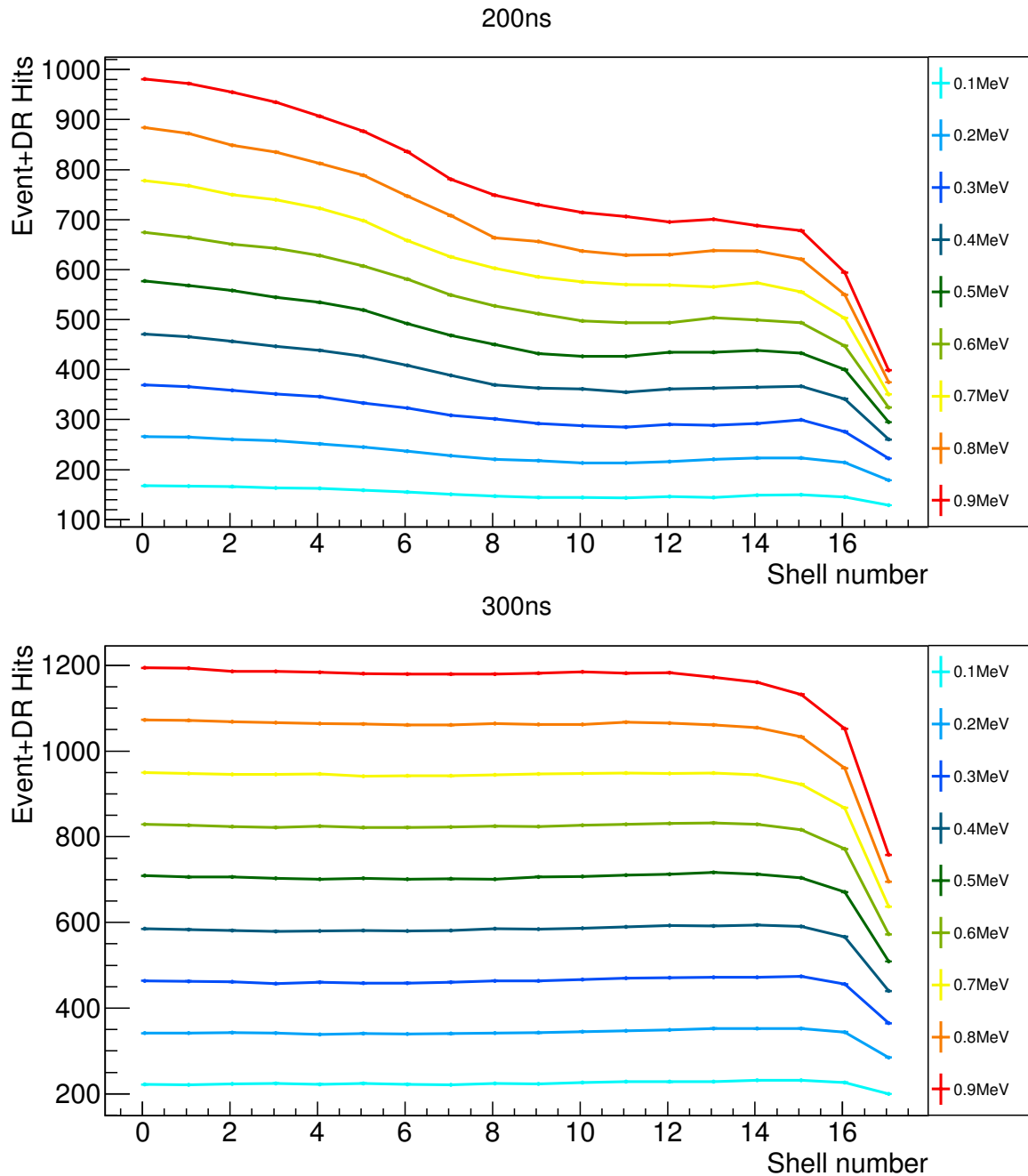
Figure 7.6: The decrease in the mean values for the "Event and dark noise" hits (*dip*) in shells 8 to 12 (Figure 7.5) is corroborated here; it is an effect seen for all energies and is only removed for a trigger window of 300 ns.

7.6 Trigger condition

The scope of this analysis considers the dark noise from the PMTs as the only background to the detection of events, no other source of backgrounds is dealt with for now. In order to set a trigger condition that only triggers on event hits and not pure dark noise hits, a few details are considered:

- The dark noise depends only on the trigger window, so a unique trigger condition can

be set for each trigger window.

- Working with three parameters viz., *shells, trigger windows and energy* means that for a choice of trigger window all the simulated data can be added to find the most correct value with respect to dark noise hits.

- Once all the requisite data (for a trigger window) has been summed up, the subsequent dark noise histogram(s) can be fitted with a Gaussian function, as as shown in Figure 7.7. The results are given in Table 7.2.

To set a trigger condition with data from the Gaussian fit (mean μ_{DN} and standard deviation σ_{DN}), a choice is made to set the threshold number of hits from events at

$$\mu_{\mathbf{DN}} + \mathbf{n} \cdot \sigma_{\mathbf{DN}}, \; n \in \mathbb{N}. \tag{7.1}$$

The value of **n** can be optimized by minimizing the rate of false triggers.

False trigger rate

As the data system of JUNO reads out the PMT data every 16 ns (trigger slip window), there is a possibility that pure dark noise hits could cause false triggers *if* the value **n** is not large enough, i.e., if the threshold number of hits is not sufficiently higher than the dark hits. Table 7.3 summarizes the different values of **n** and the false trigger rates that they could lead to. $\mathbf{n} \cdot \sigma_{DN}$ is an integral multiple of σ_{DN} that quantifies the difference between μ_{DN} and the threshold number of hits that could be set at $\mu_{\mathbf{DN}} + \mathbf{n} \cdot \sigma_{\mathbf{DN}}$.

$\mathbf{n} \cdot \sigma_{DN}$	**False trigger rate** (in Hz)
$4 \cdot \sigma_{DN}$	13436.5
$5 \cdot \sigma_{DN}$	15.2145
$6 \cdot \sigma_{DN}$	0.07697
$7 \cdot \sigma_{DN}$	$< 10^{-5}$

Table 7.3: False trigger rates for different values of $\mathbf{n} \cdot \sigma_{DN}$

Table 7.3 makes it clear that a choice of $n = 7$ is best for a trigger condition as it ensures that there are no hits from dark noise, shown in Figure 7.7. Thus, the minimum number of hits from an event (which is the trigger condition) is chosen to be:

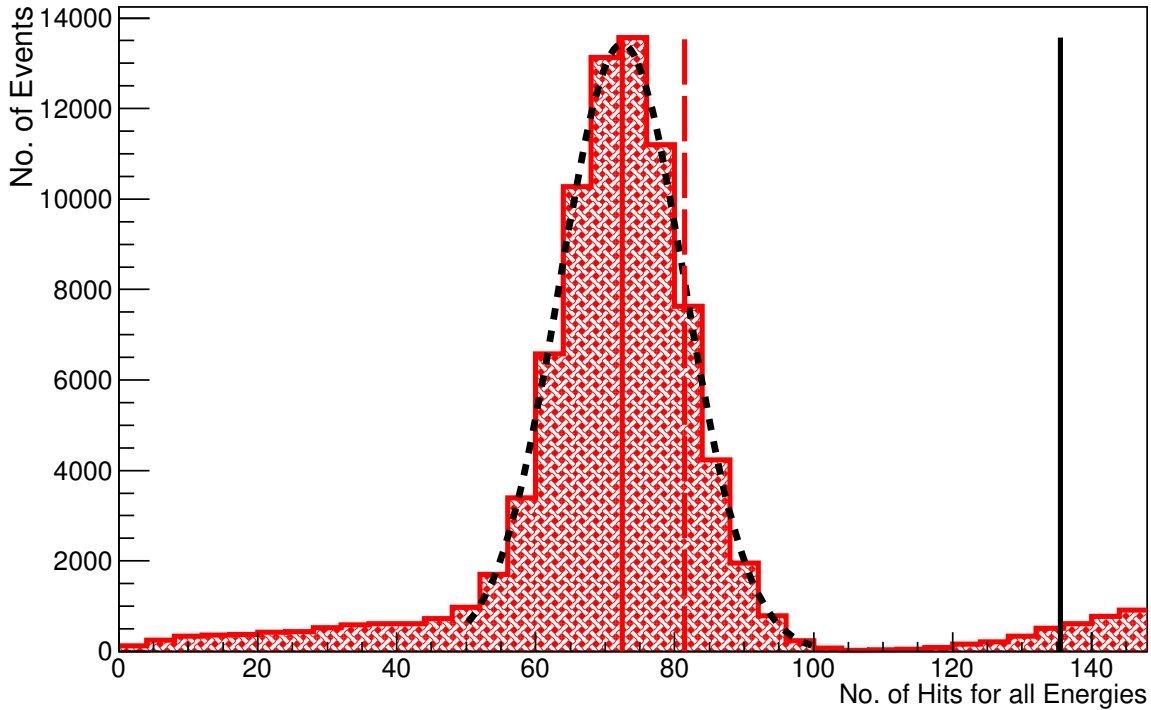$$\mu_{\mathbf{DN}} + \mathbf{7}\sigma_{\mathbf{DN}}. \tag{7.2}$$

Figure 7.7: Gaussian-fitted histogram of all simulated dark noise and event data (in red), for a trigger window of 200 ns. This includes data from all shells and all energies from Table 7.1. The red dashed line represents a distance of $1\sigma_{DN}$-hits from the mean μ_{DN}, which is the red line. The solid black line is $7\sigma_{DN}$ away from μ_{DN}, set as the trigger condition.

7.7 Trigger threshold energy

The number of hits from events (note that these always have a contribution from dark noise as well) are different for every shell and trigger window for all event energies. To understand how the trigger threshold, a value in terms of number of hits, translates to an energy i.e. a trigger energy, we see an example in Figure 7.8. The change of the detector response for events of the same energy but different shells or trigger windows is seen in the difference of the number of hits - which further necessitates the correlation of a particular number of hits (depending on the analysis parameters) to the actual energy of the event such that a relation between event energy and number of hits is Figure 7.9. With the calibration data from the curves in Figure 7.9, we can evaluate the trigger threshold (hits) in terms of energy, and see the trends in the detector for the threshold energy shell-by-shell in figures 7.10, 7.11 and 7.12.

The trigger energy is always less than 75 keV for a trigger window of 300 ns, and less than 90 keV for a trigger window of 200 ns.
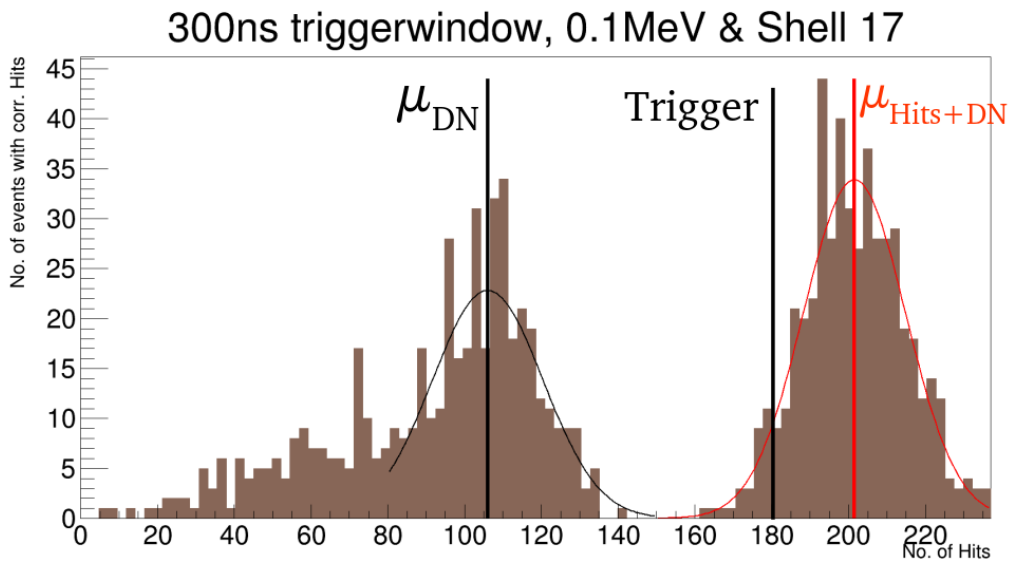
Figure 7.8: The above figure is the raw output of a 0.1 MeV event in shell 17, for a choice of trigger window of 300 ns. Once Gaussian functions have been fitted, we can see (from the black lines) the μ_{DN} and the trigger, which has been set for the 300 ns trigger window. The mean value of the event hits $\mu_{\text{Hits} + \text{DN}}$ is for an event with specific analysis parameters, which are subject to change for different combinations of parameters from Table 7.1. The trigger efficiency is the ratio of events in the right histogram (Histogram of dark noise and event hits) after the trigger to the total events in the right histogram.
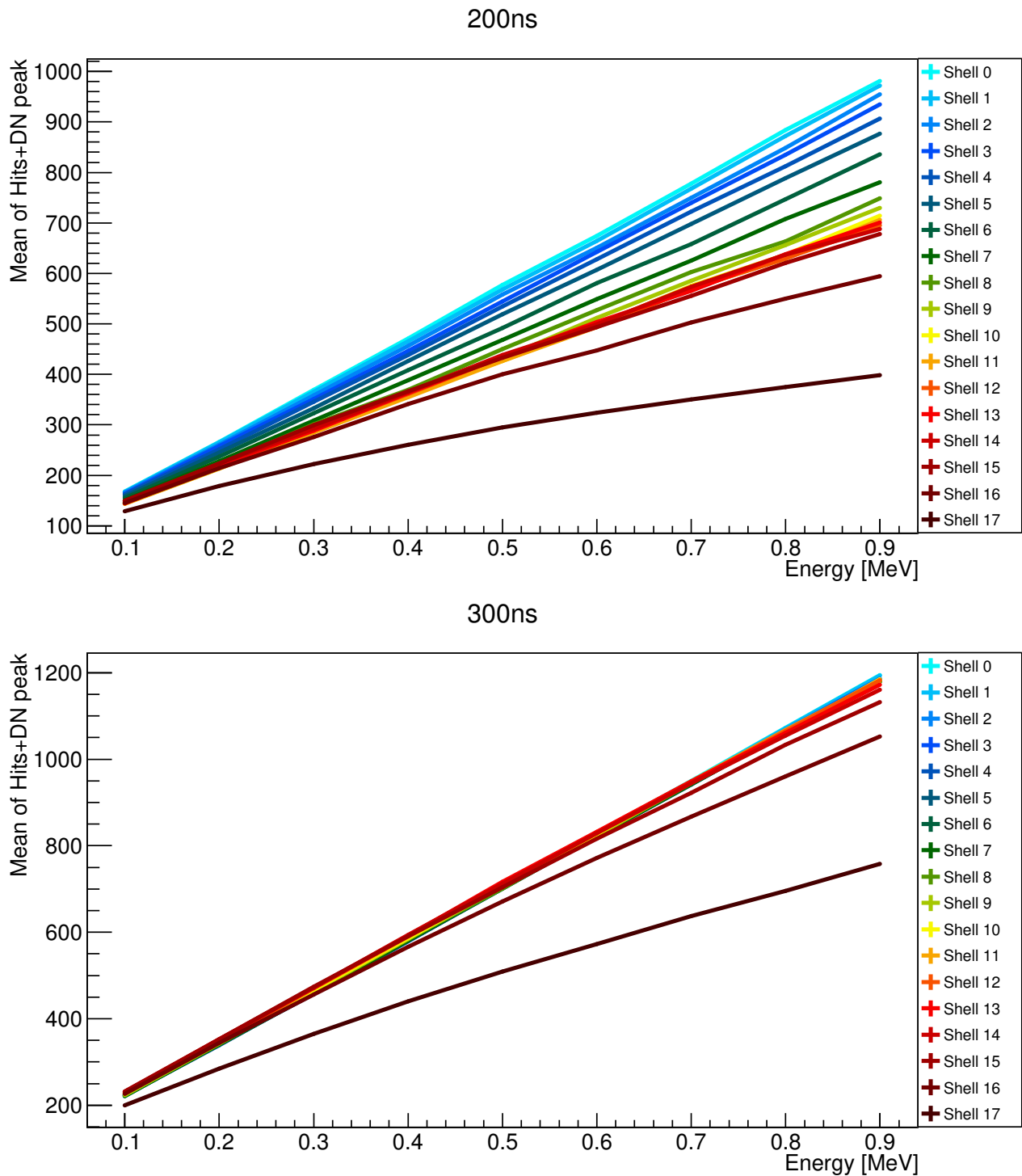
Figure 7.9: The calibration curves for two trigger windows: 200 ns (upper) and 300 ns (lower). For 200 ns, there is a clear differentiation among the calibration curves for each shell as they are spread out. However, for a 300 ns trigger window, there is only a short band in which the calibration curves lie except for the outermost shells (i.e. shells 16 and 17). This further shows that for a 300 ns trigger window, the detector response is homogeneous for all shells, while it is not so for a 200 ns trigger window.

45
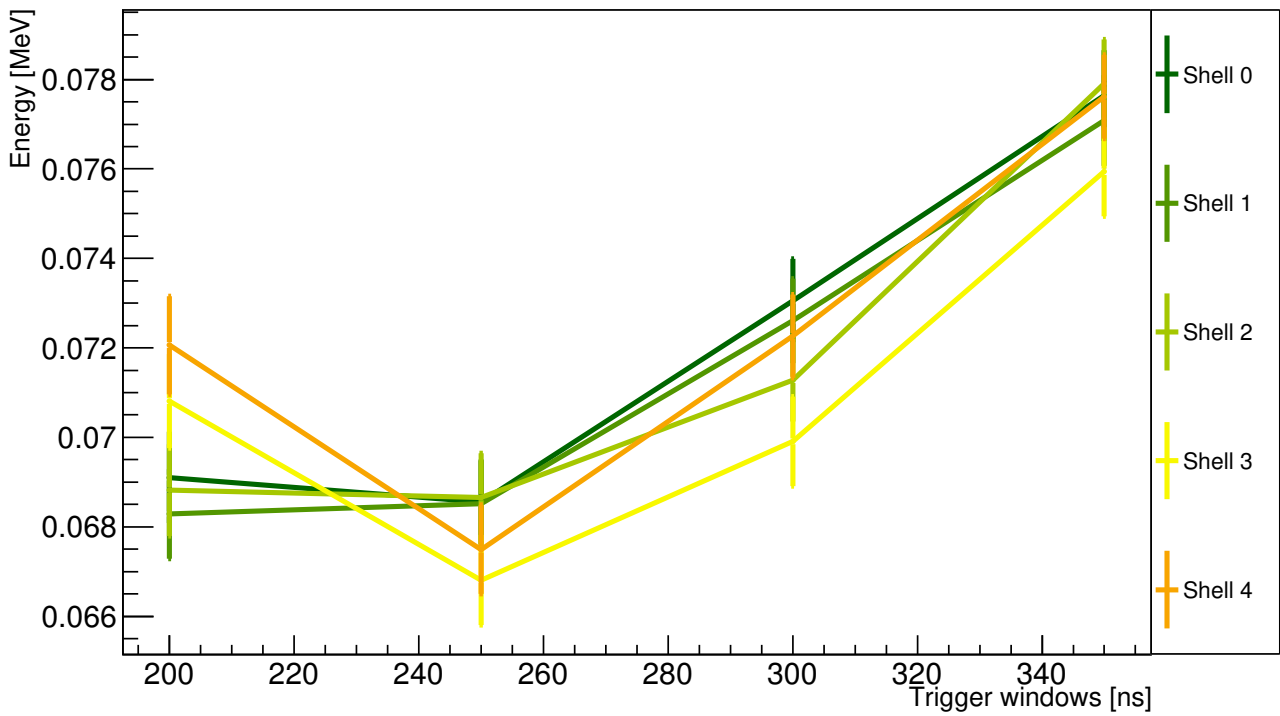
Figure 7.10: The trigger energies for shells 0 to 4, which follow a similar trend: increasing with increasing trigger window. With the increas in the trigger windows an incremement of ~18% is observed.
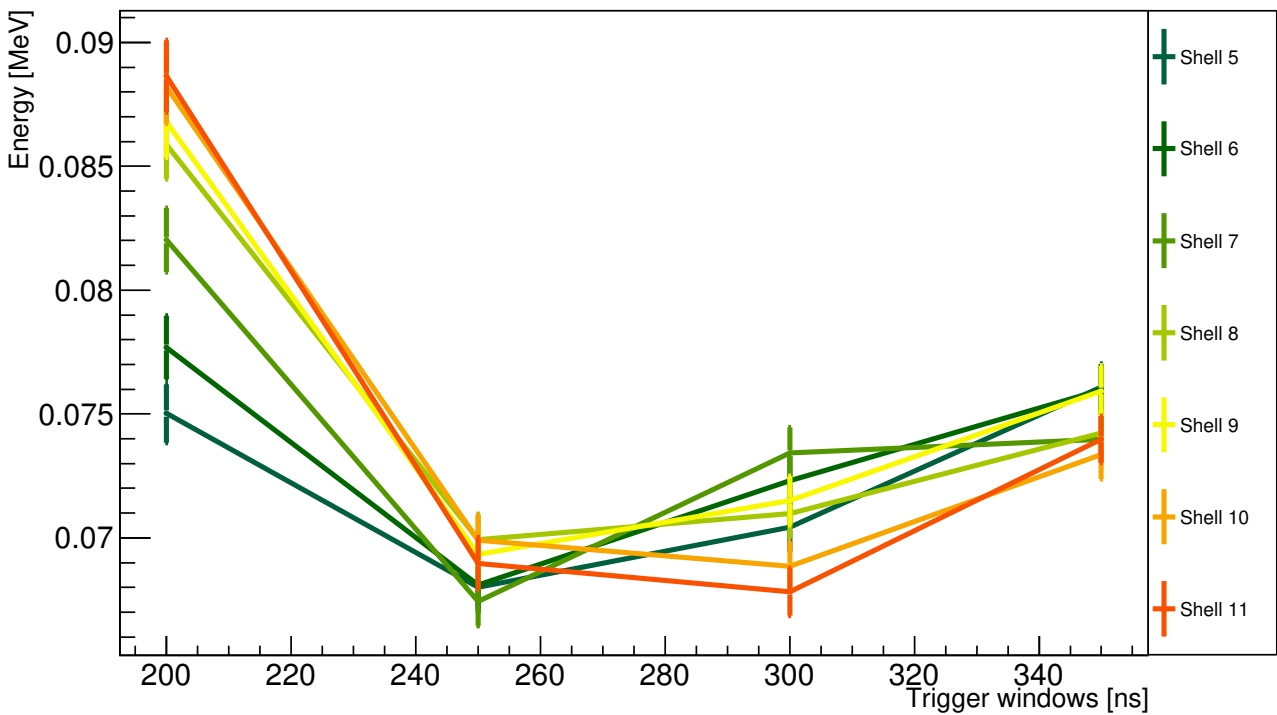
Figure 7.11: The trigger energies for shells 5 to 10, which also follow a similar trend: decreasing (~25% overall) or stagnating with increasing trigger window.
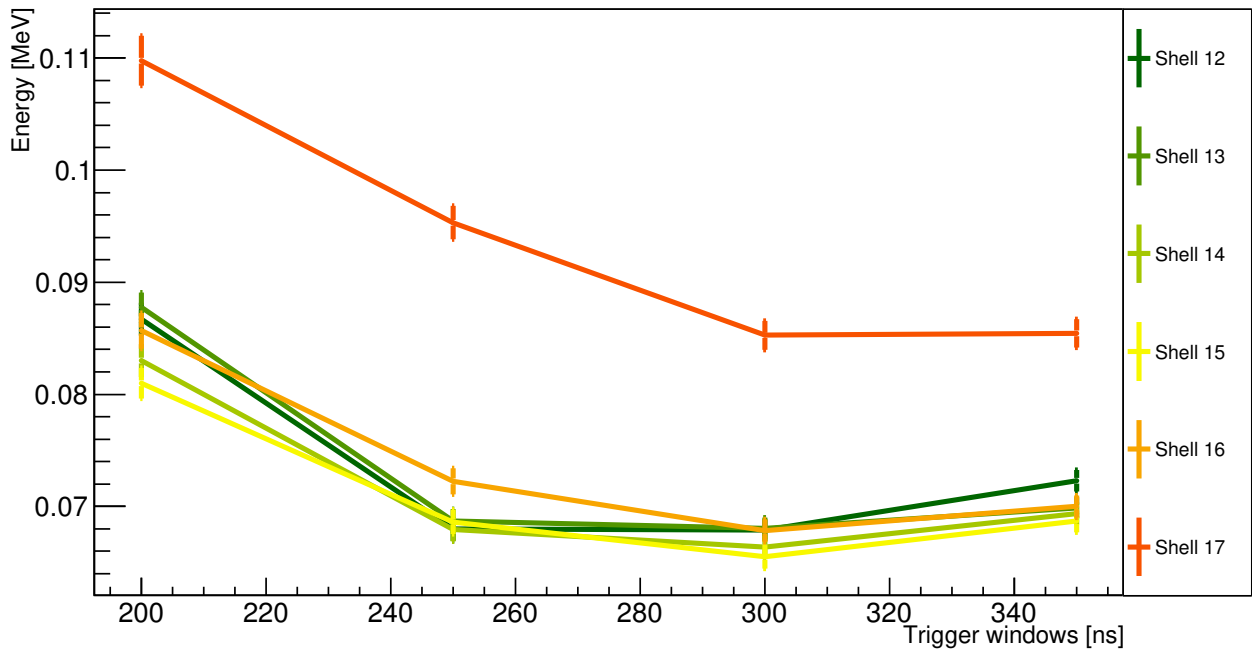
Figure 7.12: The trigger energies for shells 11 to 17, which follow a similar trend to the shells directy before: decreasing with increasing trigger window. For shell 17, the trigger energy is much higher as it is the outermost shell and registers the lowest number of hits.
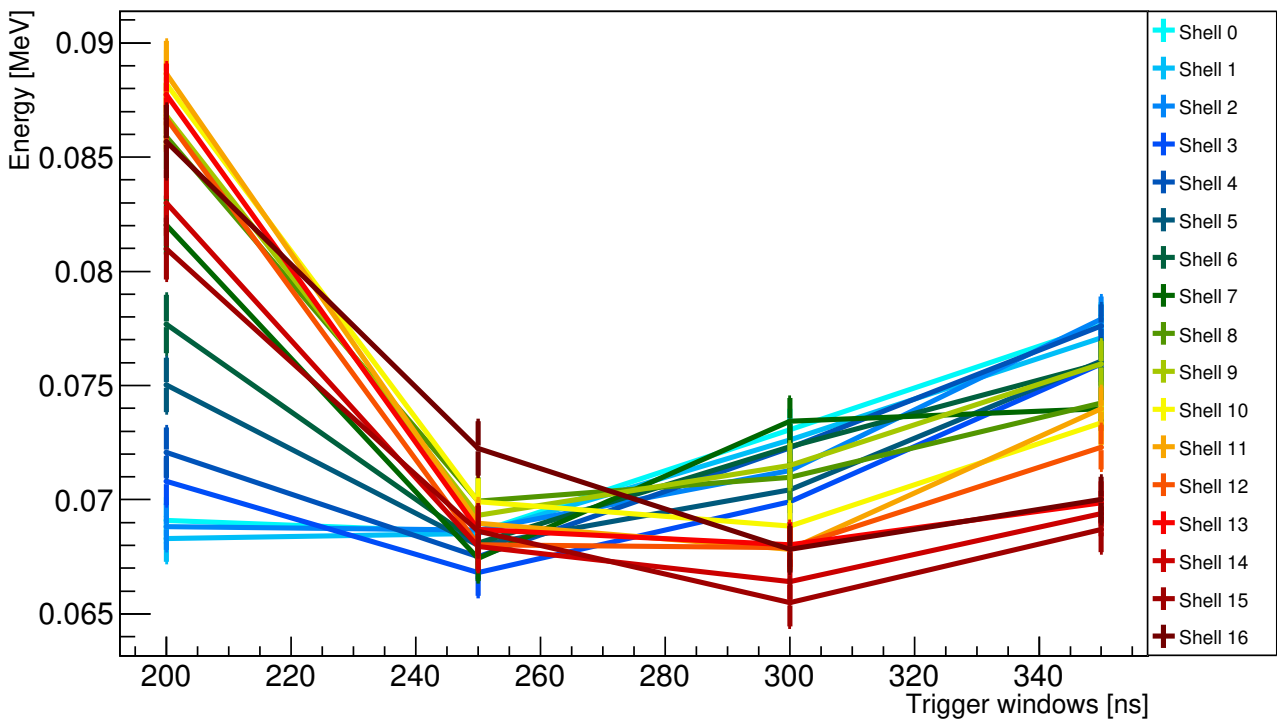
Figure 7.13: The trigger energies for all the shells, save for shell 17. The trends in the Figures 7.10, 7.13 and 7.12 can be seen here, with respect to each other.

7.8 Trigger efficiency

The trigger efficiency for the detector can be presented in 3 ways, for a choice of at least 2 of the 3 analysis parameters (shells, trigger windows and event energies) and varying the third parameter. The trigger efficiency is described in Figure 7.8. Features of the trigger efficiency (observed in Figures 7.14, 7.15 and 7.16) include:

- The trigger efficiency (TE) is 100% for all events with energy $E \geq 0.2$ MeV, as seen in Figure 7.15, for all shells and all trigger windows.

- The TE is low for the outermost shell (shell 17) for 200 ns, but is higher for 250 ns and 300 ns trigger windows (Figure 7.14). A larger trigger window (e.g. 350 ns) leads to no further increase in the trigger efficiency.

- TE is ~100% for a trigger window of 300 ns for all shells and energies.

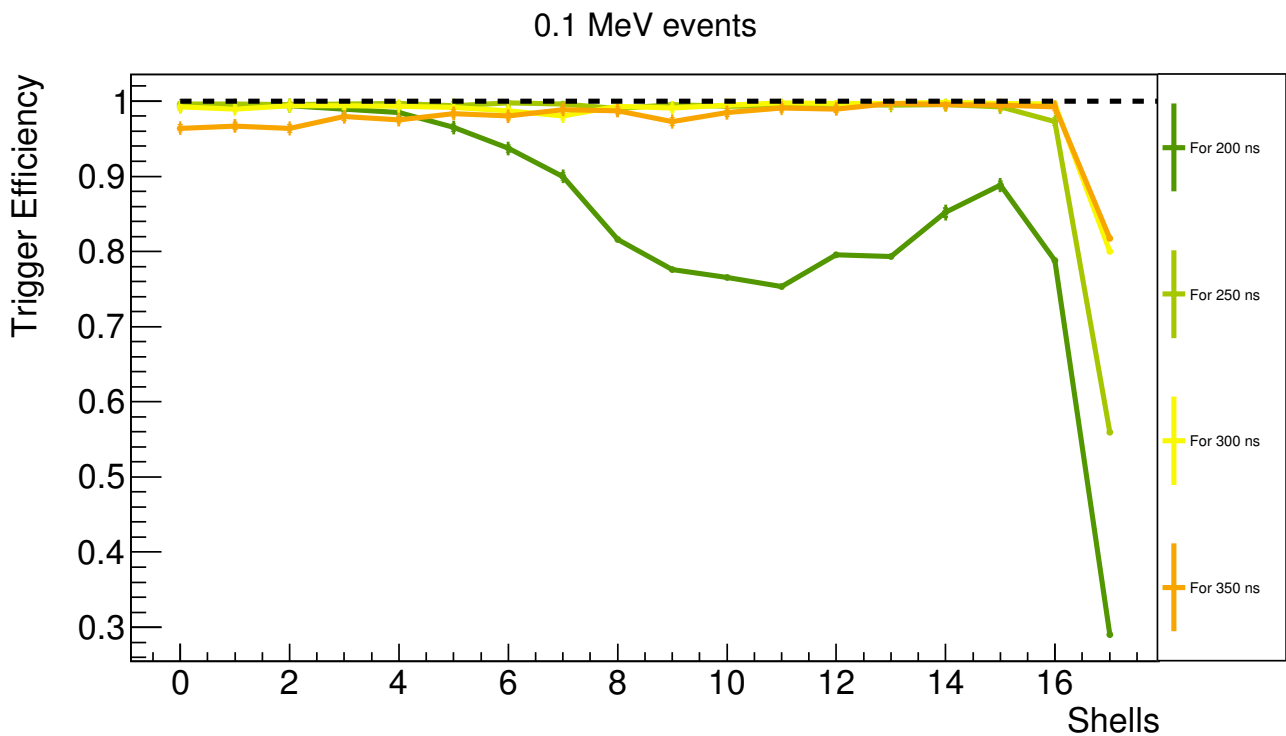- The errors on the estimation of the trigger efficiency are statistical in nature, about ~0.5% .

Figure 7.14: Trigger efficiency (TE) for events of energy 0.1 MeV, plotted as a function of the shells for various trigger windows. For inner shells of the detector (shells 0 to 4) the TE is ~100%, which gets worse for outer shells. The trends show a large inefficiency for a trigger window of 200 ns, while for 250 and 300 ns the efficiency is higher. The black dashed line is 100% efficiency.
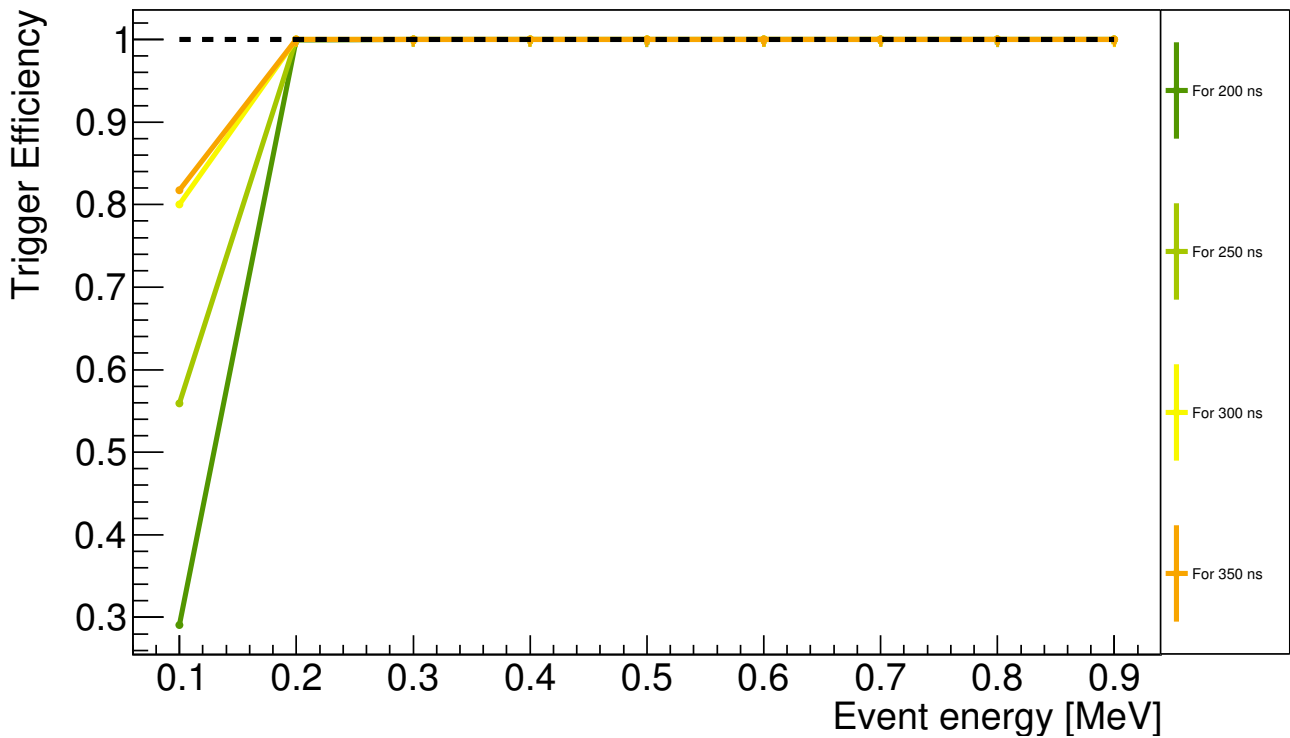
Shell 17

Figure 7.15: The trigger efficiency is plotted as a function of the event energies for different trigger windows in shell 17. The change in the TE is shown for different trigger windows reaches 100% efficiency for $E \geq 0.2$ MeV. The black dashed line denotes 100% efficiency.
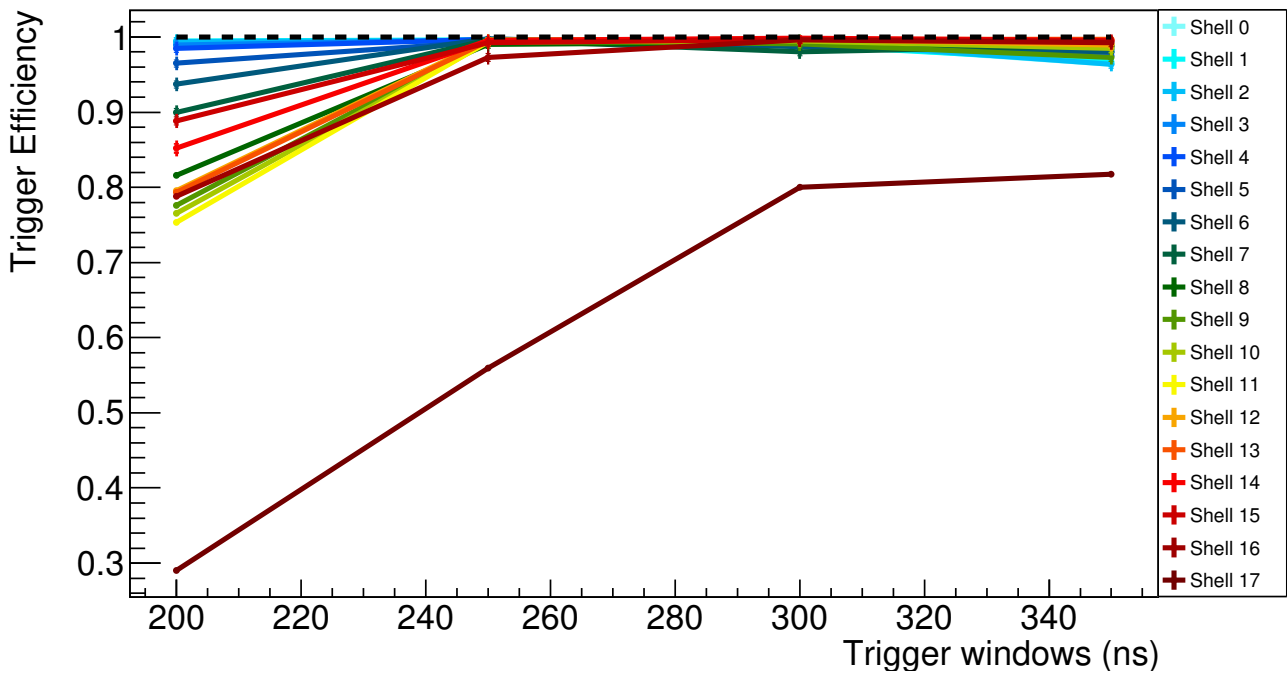
0.1MeV events

Figure 7.16: The trigger efficiency is plotted for 0.1 MeV events as a function of trigger windows. The least efficiency is for the outermost shell, i.e. shell 17. For the other shells, the increase in trigger window after 300 ns leads to no appreciable change. This can be seen relative to the black dashed line representing 100% efficiency.

Trigger rate in JUNO

In the previous section, the only background we considered for analysis was dark noise from the PMTs, for low-energy events. The internal radioactivity of the detector, from the decay of unstable nuclei in the LS, is a major contributor to the backgrounds which effect the detection of neutrino events. This section deals with the effects of the backgrounds and studies the persistence of these backgrounds for different hits registered in the detector. The result of the previous section, the optimized trigger window of 300 ns, is used in this analysis. Along with the backgrounds, we also add the solar neutrinos from the pp process and from ^{7}Be decay in the Sun. The backgrounds originating from within the detector, specifically in the LS, are easier to study via a Monte Carlo simulation whereas the backgrounds due to the decay of unstable nuclei around the detector and from external sources is more difficult to generate via a Monte Carlo simulation. The Monte Carlo simulation of decay products from external (non-LS) sources is more time consuming and intensive, hence they are not investigated in the scope of this work, though may be taken up later in succeeding studies.

8.1 Choice of components

The extent of the work done here covers the sources of background, i.e. the unstable nuclei, present in the liquid scintillator itself. The presence and concentration of these impurities in the LS is kept to a minimum to ensure the purity and have the resulting internal radioactivity be as little as possible. The choice of these sources of backgrounds is done while keeping in mind their activity, concentration in the LS, etc. as seen in Table 8.1. Other components which constitute our analysis are solar neutrinos, and the pileup events.

Component	Counts per second [CPS] (in JUNO)	Counts per day per kton [CPD/kton]	Specific Activity [Bq/kg]	Concentration in the LS (g/g)
^{238}U	0.0248	107.136	$1.24 \cdot 10^4$	10^{-16}
^{232}Th	0.00814	35.1648	4070	10^{-16}
^{14}C	$4 \cdot 10^4$	$1.728 \cdot 10^8$	$1.7 \cdot 10^{11}$	10^{-17}
^{40}K	0.0531	229.392	$2.654 \cdot 10^6$	10^{-17}
^{85}Kr	0.1157	500	$1.45 \cdot 10^{13}$	$4 \cdot 10^{-25}$
^{11}C	0.431	1861.92	$3.11 \cdot 10^{19}$	$7 \cdot 10^{-31}$
^{210}Po	1.62038	7000	$1.66 \cdot 10^{14}$	$5 \cdot 10^{-25}$
^{210}Bi	0.0095	410.6	$4.6 \cdot 10^{14}$	10^{-27}
^{14}C-^{14}C pileup	480	$2.0736 \cdot 10^6$	-	10^{-17}
^{7}Be νs	0.119	517	-	-
pp-process νs	0.318981	1378	-	-

Table 8.1: The data accumulated and used to analyze the events arising from the decay of the radioactive nuclei, from pileup events, and from solar neutrino interactions. While most of the data comes from [17], some Borexino data from [65] and [66] is used. The values for CPS (counts per second), CPD (counts per day)/kton and concentration are all related to each other, and are mentioned here for completeness; the data used in the aforementioned sources uses one of these three values to measure the radioactivity in the detectors. In the case where the CPD/kton value is known, for example, the specific activity is used to obtain values of the CPS and the concentration in the LS. This gives a more broad perspective for these contaminations in the LS. Further details regarding each background is in Figures 8.6 and 8.7. The event rate in CPS for ^{14}C-^{14}C pileup is CPS[^{14}C] $\cdot$ CPS[^{14}C] $\cdot$ (Trigger window). For a 300 ns trigger window, the CPS[^{14}C-^{14}C pileup]=480. A similar treatment for the solar neutrinos (*pp*-process and ^{7}Be) is implemented.

8.2   The Monte Carlo dataset

The number of events seen in a single day, per kton of the LS, vary from a few tens to $\sim 10^9$ (see Table 8.1). To study such backgrounds, the Monte Carlo generated dataset must have the adequate statistics which encompass all the properties of the spectra of these background sources. As mentioned in 7.4, the generation of the backgrounds is done using the *gendecay* package, *nusol* package, and finally the electronic simulation. The resultant hit profile (number of hits registered in the detector, event-by-event) is prepared without the influence of any dark noise and for the optimized trigger window of $300\,$ns. To observe the influence of the dark noise on the hits profile, a generator is set up which utilizes the dark rates assigned in 7.3. The Poisson-sampled dark hits (generated for a trigger window of $300\,$ns) are then added to the hit profile of each of the backgrounds[1], which results in an overall shift of the spectra.

Final statistics: For each background type (except for ^{14}C), a dataset of 10^5 events is generated, and the corresponding hit profile of each is used in the following analysis. As the number of events due to ^{14}C decay is $\sim 10^9$, a larger dataset of 10^6 events is used, which still falls short of replicating the whole hits profile for ^{14}C; but the generation, electronic simulation, and dark noise addition requires the maximum used events be 10^6. The dataset (from the DetSim) of these 10^6 ^{14}C decays is then used to produce the dataset for the ^{14}C-^{14}C pileup events using the event-mixing properties of the ElecSim.

8.3   Full spectra

Dark noise influence

The trigger rate studies undertaken here are with the spectra simulated with the presence of dark noise, from the setup we have previously described. To elucidate the difference this brings out, we take the example of ^{210}Bi decay events. In Figure 8.1, we have the spectrum of ^{210}Bi without the any dark noise, and in 8.2 we see the shift brought about by the presence of the dark noise. The addition of these dark hits to the hits registered in the detector for the background events are unique not only to the background source, but each individual event. If the spectra were to be analyzed without the influence of any dark rate, we would obtain Figure 8.4 for the overall backgrounds spectra. The figures presented here are analyzed with the trigger window of $300\,$ns (and $1250\,$ns, in Figure 8.3.) Figures 8.1 to 8.3 use the maximum expected number of ^{210}Bi decays in a day, $\sim$82120[2].

---

[1]The dark hits generated are unique to each event that they are added to, the spectra are not shifted by a single common value. The mean value of the dark hits generated is 106 for a trigger window of $300\,$ns. The dark hits generator is consistent with the JUNO offline software, and shares the Poissonian treatment of the dark noise used there in the PMT simulation algorithm (PMTSimAlg). The data used to assign the dark rates for each PMT is mentioned in 7.3.

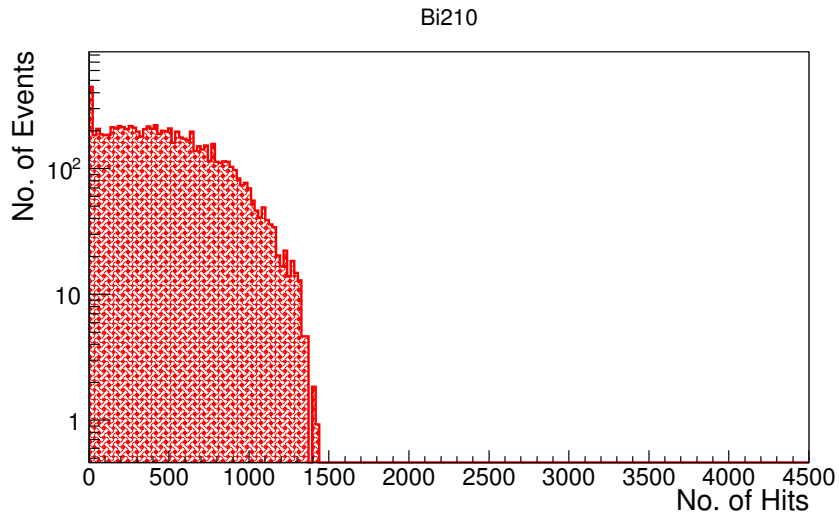[2]From Table 8.1, the CPD/kton values are scaled up by a factor of 20.

Figure 8.1: ^{210}Bi decay events for a trigger window of $300\,$ns, without the influence of any dark noise.
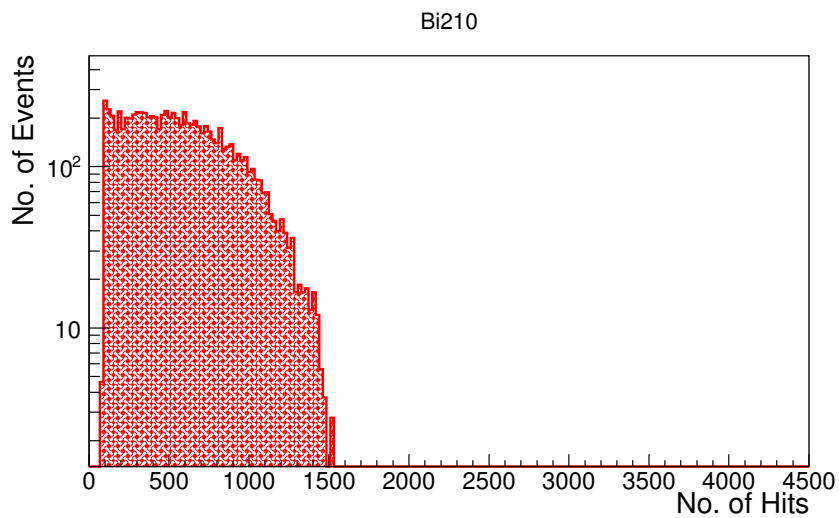

Figure 8.2: ^{210}Bi decay events for a trigger window of $300\,$ns, with dark noise. The mean value of dark noise (hits) for a trigger window of $300\,$ns is 106.
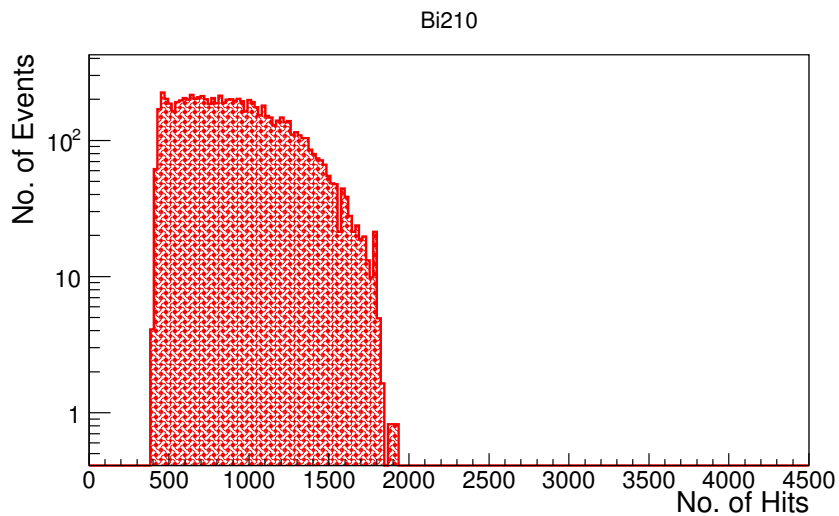

Figure 8.3: ^{210}Bi decay events for the data acquisition window of $1250\,$ns, with dark noise. The mean value of dark noise (hits) for $1250\,$ns is 440.
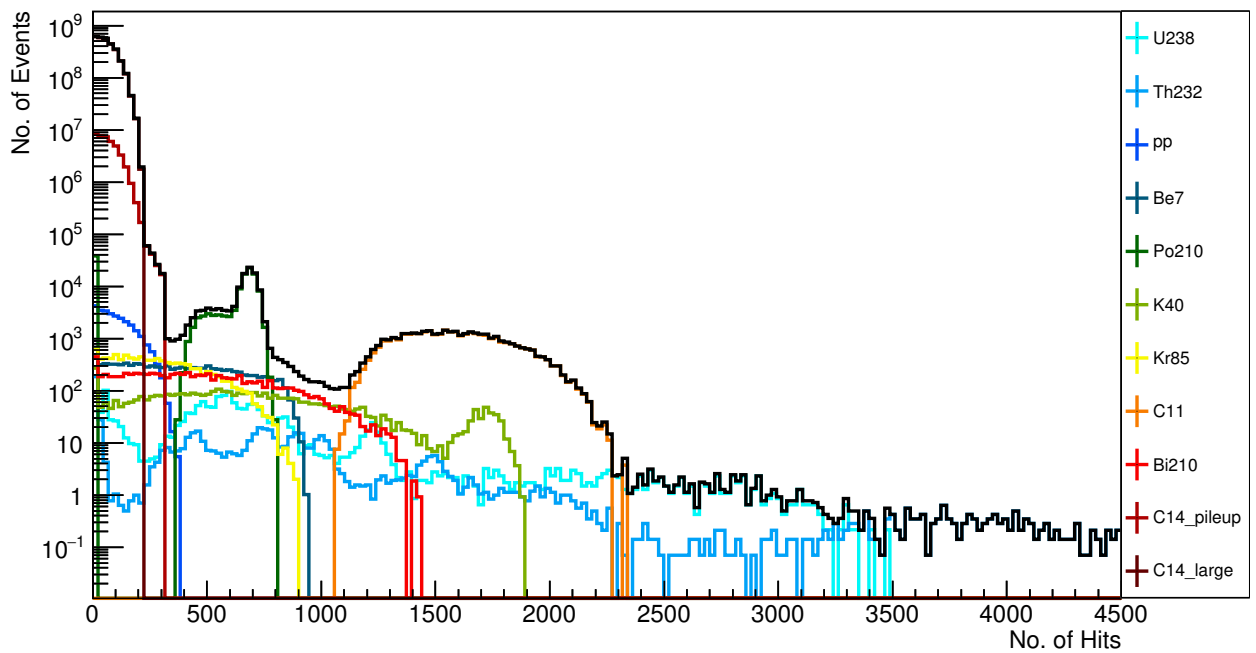
Figure 8.4: Monte Carlo simulation of all sources of backgrounds, for the maximum expected background events in a single day. The data is generated for a trigger window of 300 ns, without the influence of any dark noise. The solid black line is the sum of all background sources.
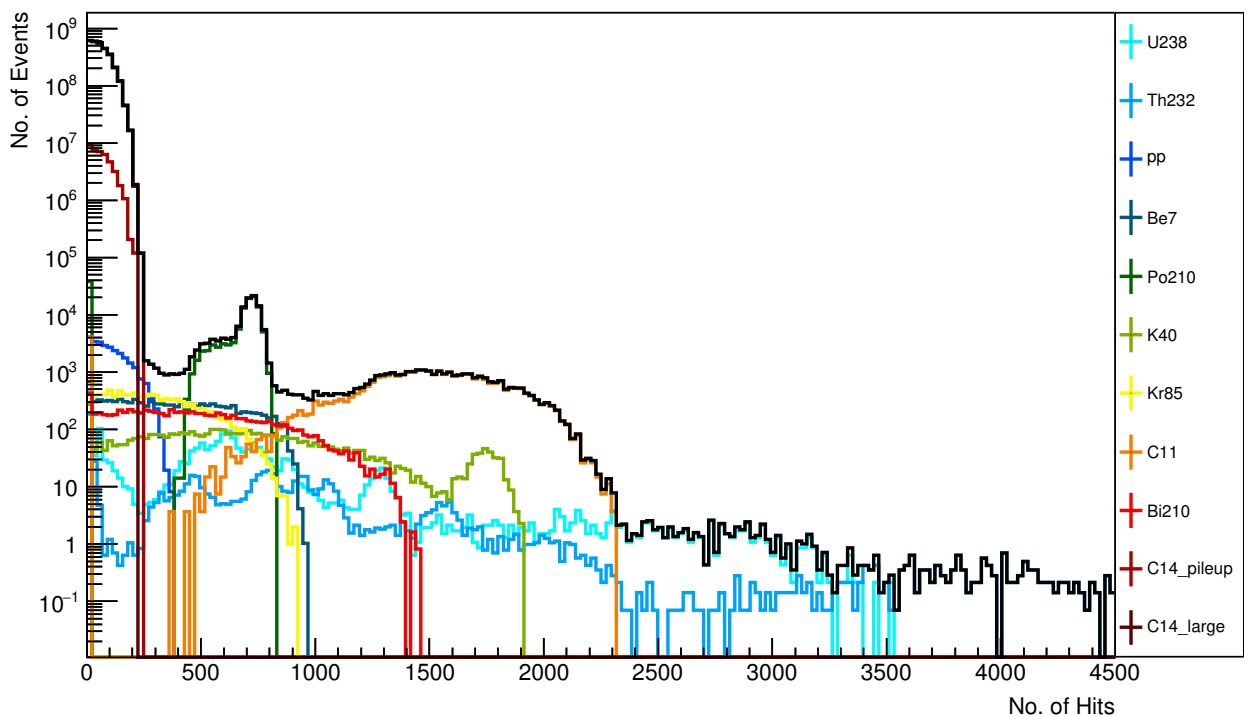

Figure 8.5: Monte Carlo simulation of all components, for the maximum expected events in a single day. The data is generated for the data acquisition window of 1250 ns, without the influence of any dark noise. The solid black line is the sum of all background sources.

54

Spectra of individual components

The following histograms (Figures 8.6, 8.7) show the spectra from each of the individual components, from the hits profile, for a trigger window of $300\,\text{ns}$. These are a day's worth of events for each source (scaled according their specific activity, from the Monte Carlo dataset). The effect of the dark noise has been included for each source with the mechanism previously mentioned. The production of these datasets (specific to each component) displays their inherent decay type, and each background type (as well as the the solar neutrinos) provided some hindrances when generating. These properties and comments, if any, are listed here.

- ^{238}U : Decays via α-emission, spontaneous fission or $\beta\beta$ decay with a half-life of 4.47 Gigayears.

- ^{232}Th : Decays via α-emission, spontaneous fission, double cluster emission or $\beta\beta$ decay with a half-life of 14 Gigayears.

- pp : Events arising from the electron-neutrino scattering, with neutrinos originating from the pp process in the Sun. In the *nusol* package, used in DetSim to generate solar neutrinos, the presence of physics discrepancies regarding the energy of pp neutrinos lead to the stunted production of these events. The correction of this error and generation of these events proved to be successful and resulted in a usable dataset.

- ^{7}Be : Events arising from the electron-neutrino scattering, with neutrinos originating from ^{7}Be decay in the Sun. Further discrepancies in the *nusol* package with respect to the correct naming of output files generated in the DetSim stage were found. These were worked around in order to obtain the correct .root file generated by DetSim for ^{7}Be events.

- ^{210}Po : Decays via α-emission with a half life of 139 days. It is out of equilibrium with ^{238}U, which makes it a major contributor to the background. The value of ^{210}Po's CPD/kton is taken from Borexino [66], and scaling it up to use as an estimate for JUNO (Table 8.1). The typical spectrum for the number of hits for α's from ^{210}Po is a single-peaked histogram since these α are monoenergetic. This is not the case here. The decays close to the detector edge register fewer number of overall hits, thus lead to a preceding tail for the spectrum shown above. In [65], [66] one can see a single peaked nature for hits due to Po decays.

- ^{40}K : Decays via β^+, β^- emission with a half life of 1.248 Gigayears.

- ^{85}Kr : Decays via β^- emission with a half life of 10.731 years.

- ^{11}C : Decays via β^+ emission with a half life of 20.334 minutes. The hits profile seen for the ^{11}C decay events was much higher than the hits expected in JUNO. The error was in the production of decay events near the detector edge, beyond the fiducial volume cut, with a radius of $15.8\,\text{m}$. Once this cut was used, the decay events were produced for radii $\leq 15.8\,\text{m}$, and the hits spectrum was found to be compatible with the expected values.

- ^{210}Bi : Decays via β^-, α emission with a half life of 120 hours. The production of ^{210}Bi decays in the Monte Carlo data required the deactivation of the production of (radioactive, unstable) daughters of ^{210}Bi. This required using the option *decay depth* in the DetSim 7.4 and setting it to 1, so as to produce only ^{210}Bi decays. In the offline software, this ran into problems in the utilization and had to be subsequently produced in the IHEP computer cluster which has the corrected version of the offline software.

- ^{14}C : Decays via β^- emission with a half life of 5700 years. The dataset uses 10^6 events in order to facilitate a faithful reproduction of the actual decays, whereas the rest of the background data sets and solar neutrinos have a dataset of 10^4.

- ^{14}C-^{14}C pileup events are produced from the dataset of ^{14}C events, with hit-level event mixing in the ElecSim.

In order to paint the entire picture of background events arising from the radioactive decay of the unstable nuclei (in the LS) and the pp and ^{7}Be neutrinos, the histograms shown and discussed above can be summed up for common parameters, such as the data acquisition (DAQ) time window (or trigger window) and a specific time duration in which the background events are expected. This is done for the trigger window of 300 ns, as in Figure 8.8, and for the entire readout window of 1250 ns, as in Figure 8.9. For each of these, the histograms in Figures 8.6 to 8.7 are added up, for a specific time duration (and the respective trigger window). In Figures 8.8 and 8.9, the maximum background events expected in a single day (86400 s) are scaled from their respective original Monte Carlo datasets and summed.
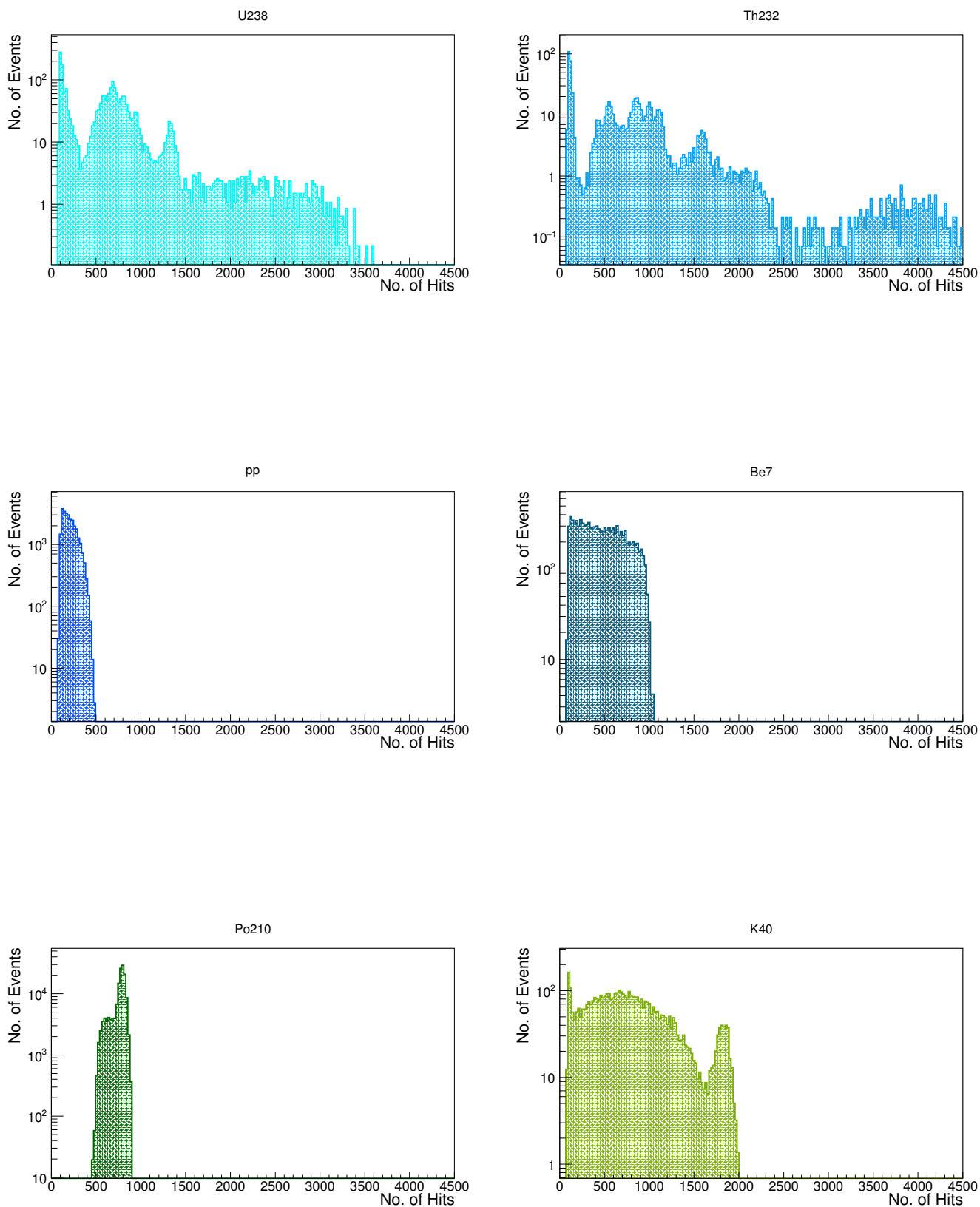
Figure 8.6: Spectra of the individual components, for a trigger window of 300 ns, with respective events detected over a day.
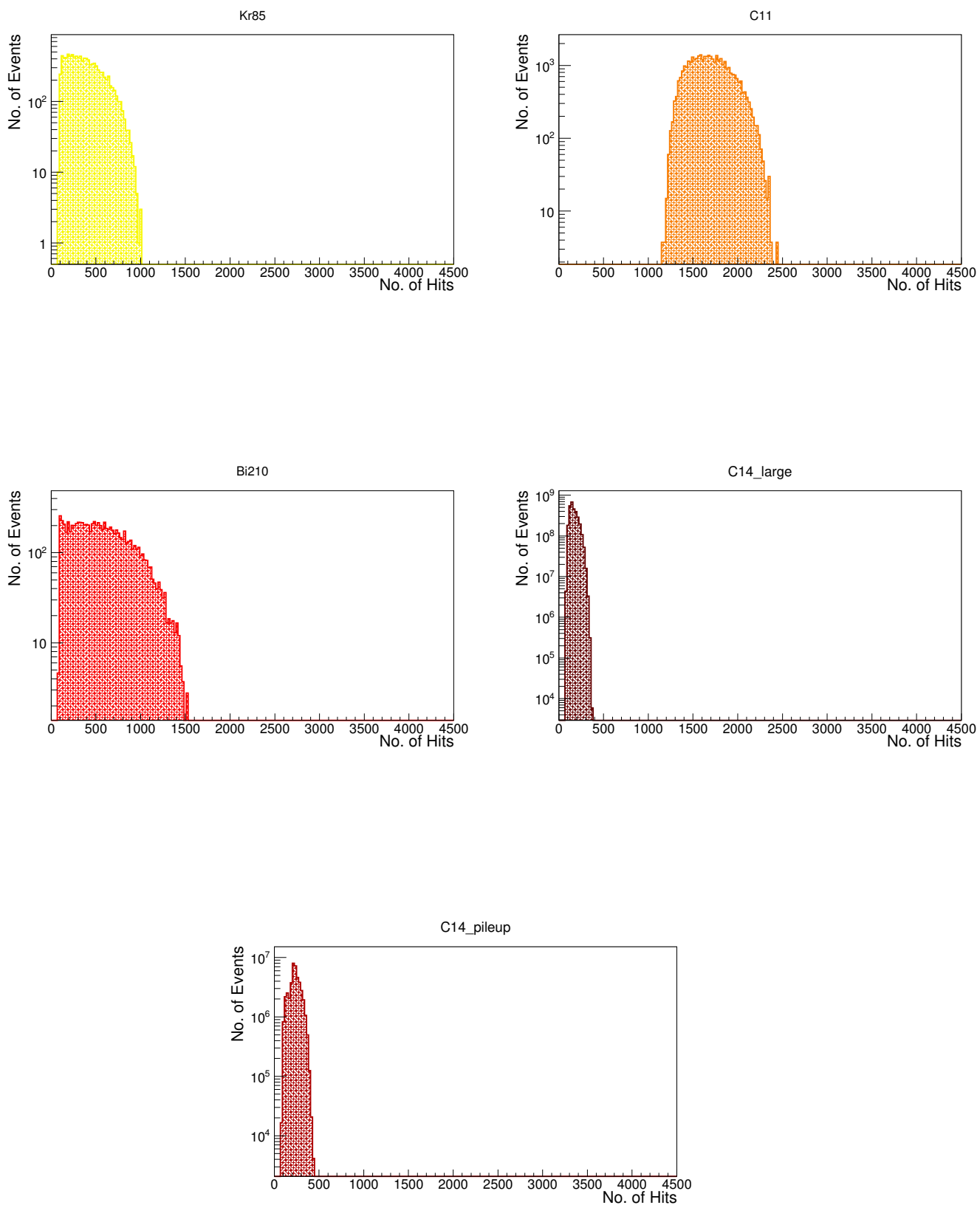
Figure 8.7: Spectra of the individual components, for a trigger window of 300 ns, with respective events detected over a day.
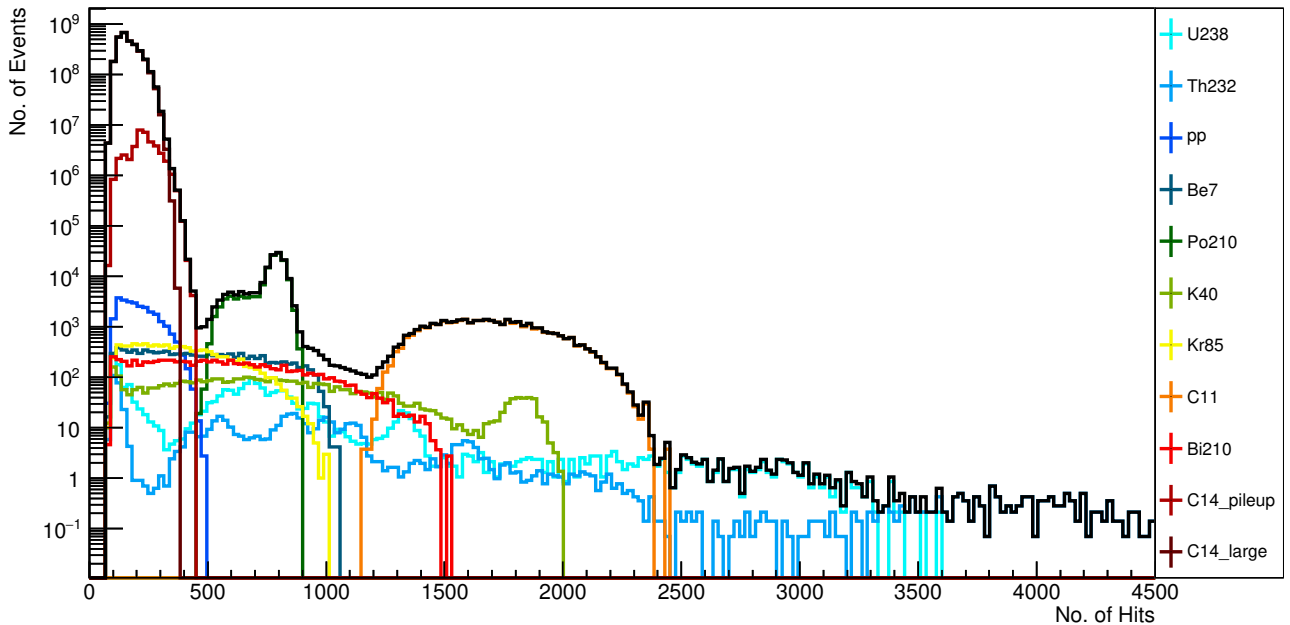
Figure 8.8: Monte Carlo simulation of all components, for the maximum expected background events in a single day. The data is generated for a trigger window of $300\,\text{ns}$. The properties of the separate histograms added up are as seen in Figures 8.6 and 8.7, and the solid black line is the sum of all background sources. For number of hits ≤ 500, the dominant sources of background events are ^{14}C decay events and ^{14}C-^{14}C pileup. As the number of hits increase, the main contrbutors to the overall backgrounds are ^{210}Po and ^{11}C, even though these are respectively fewer than the ^{14}C and ^{14}C-^{14}C pileup events by a factor of $\sim 10^5$. The trigger decision window of $300\,\text{ns}$, as investigated in the previous section, is optimum for the analysis of low-energy events such as those seen here; the decision for any trigger rate can be made from further analysis with the data in this trigger window.
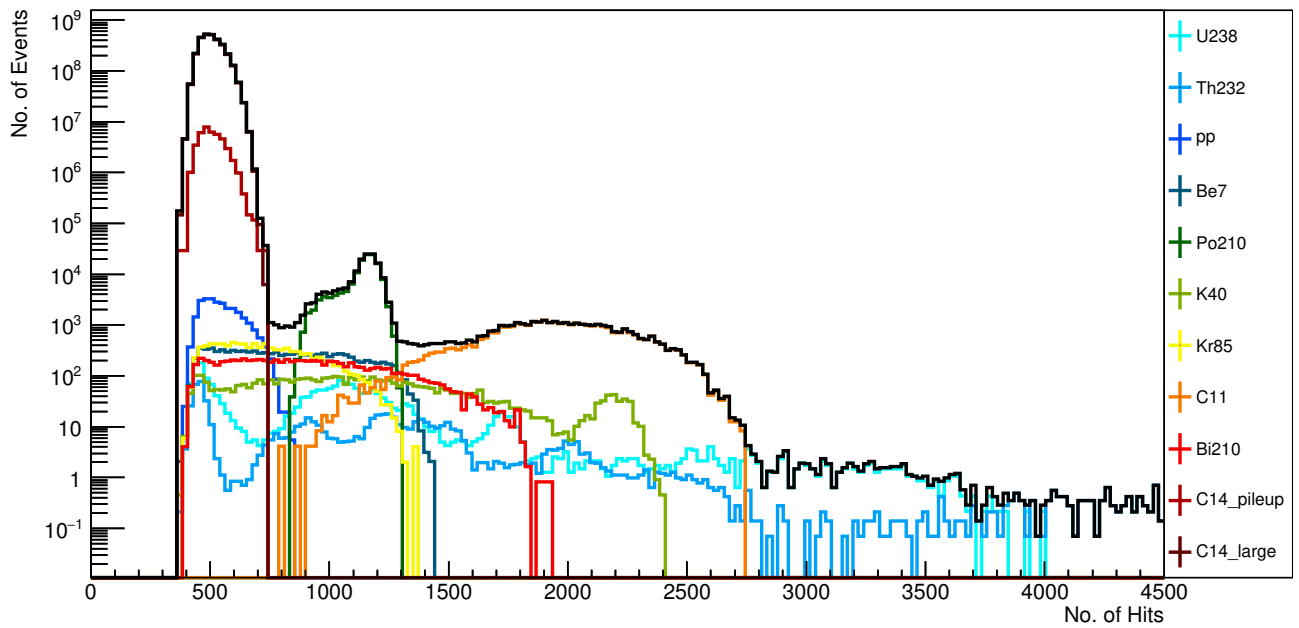
Figure 8.9: Monte Carlo simulation of all components, for the maximum expected background events in a single day. The data is generated for the data acquisition window of 1250 ns. This longer time window allows for the collection of more hits, i.e., more PMTs triggered. The dark noise, which has been added spearately to each background source (mentioned in 8.2), is modified for the time window of 1250 ns and correspondingly added. The changes in the hits profile of each background source due to this are made conspicuous in the solid black line that is the sum of all the background sources.

60

8.4 Trigger rates

In this section, an analysis of the triggering rates due to each individual component is studied, with its relation to the number of hits registered in the detector. For each of the histograms in Figures 8.6 to 8.7, an increment in the number of hits means a decrease in the corresponding number of events above that particular threshold required for trigger decision. This relationship is undertaken for each of the components, and their resulting contribution to the overall trigger rate is found. Once this is normalized to the number of expected background events (from all sources), the fractional contribution of each component can be seen for increasing values of the number of hits. This is seen in Figures A.1 and A.2: these are the contribution of each component to the overall background rate, if only one such event were to be detected. Using the contributions in Figures A.1, A.2 all together, gives the (overall) fractional contribution in Figure 8.10.

The trigger rates for the various components and their sum is Figure 8.11. In order to successfully reduce the effect of ^{14}C and the ^{14}C-^{14}C pileup, the threshold number of hits (i.e. the minimum number of hits registered in the detector) must be 400 to 500. A consequence of this will be that pp neutrinos will not be detected as they also register a maximum of 500 hits (per event). The triggering rate of the remaining components remains $< 4\,$CPS overall.
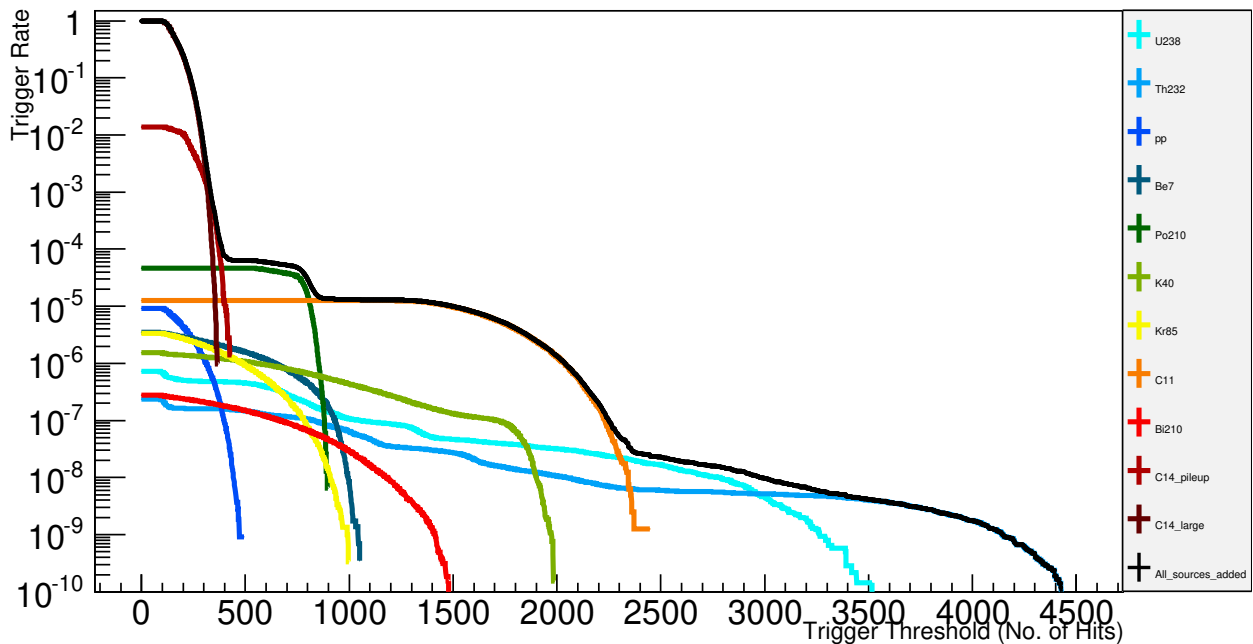

Figure 8.10: The fractional contribution from each component to the overall spectrum. The solid black line is the summed up contribution. As expected from Figure 8.8, the dominant contributors to the signal are ^{14}C and the ^{14}C-^{14}C pileup, which indicates already the threshold number of hits to minimize the effects of these components.
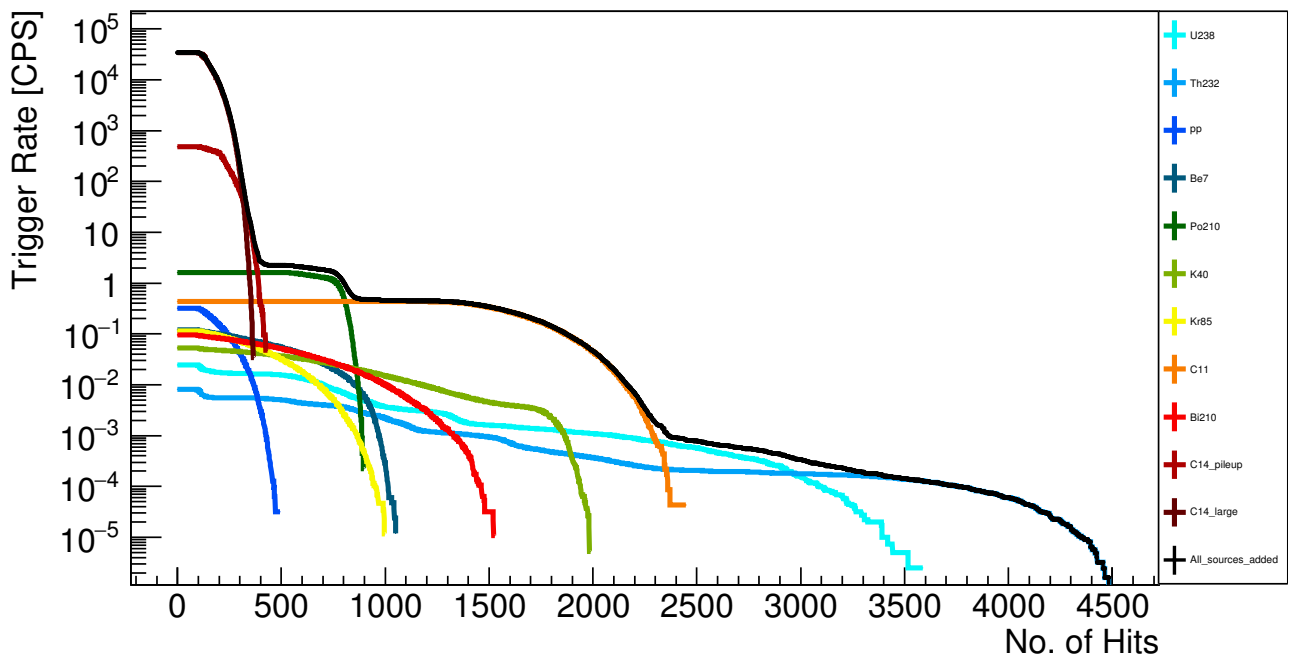
Figure 8.11: Trigger rates for each component and their sum (solid black line) as a function of the threshold number of hits in the 300 ns trigger window.

9

Results and summary

The parametrization of the JUNO detector setup with respect to shells and trigger windows yields information about the treatment of low-energy events. The setup of the realistic dark noise in JUNO is prepared by using data of about 2600 PMTs from the testing site in Zhongshan. Assigning all 17738 PMTs a dark rate from this data realizes the expected dark noise from the PMT setup in the detector. To minimize the effect of this dark noise, the trigger condition is set such that the rate of false triggers, namely the random triggers due to dark hits, is less than 10^{-5} Hz. This optimized trigger condition is then used to obtain threshold energies. Moving through the detector, from the first shell to the outermost shell, we observe some trends in the threshold energy for different trigger windows. The minimum threshold energy is ~ 0.065 MeV, while the highest threshold energy is ~ 0.11 MeV (for the outermost shell). The threshold energies typically get lower with increasing trigger window, and for events with energy ≥ 0.2 MeV, all events can be triggered successfully with no pure dark noise events. The trends seen in the detector for the hits registered shell-by-shell require that the trigger window be set at 300 ns. This ensures a homogeneous treatment of low-energy events in any part of the detector, with no preference for any shell. For any further increase in the trigger window, there is no appreciable increase in the trigger efficiency, for any shell or energy.

Piecing together the spectra from the radioactive decays of several unstable nuclei in the liquid scintillator, and adding to this the events from solar neutrino interactions (from the pp process and ^{7}Be decay), we obtain a tableau of the expected events. The previously prepared setup of the dark rates is utilized again to add dark noise to the pure decay event (or neutrino event) spectra. The concentrations and expected number of events, for every source, is strung together to facilitate the production and analysis of these events. The Monte Carlo simulation of many of the background sources, solar neutrino events, and the pileup required some modifications and workarounds; nevertheless they are presented here in their totality. Varying the threshold number of hits, the events (from any component) reduce according to their energy and/or decay type; this relationship is studied to obtain the trigger rates for these events. The analysis is performed with the optimum trigger window of 300 ns. From the summed trigger rates, and over the entire range of hits, the major contributors that trigger far more than neutrino events are ^{14}C and the ^{14}C-^{14}C pileup. To trigger above these events, the threshold number of PMTs triggered must be set at 400 at least. While this may erase most pp neutrino events, the remaining components have at most a trigger rate of 4 CPS (counts per second). This would be a reduction by a factor of about 10^4.
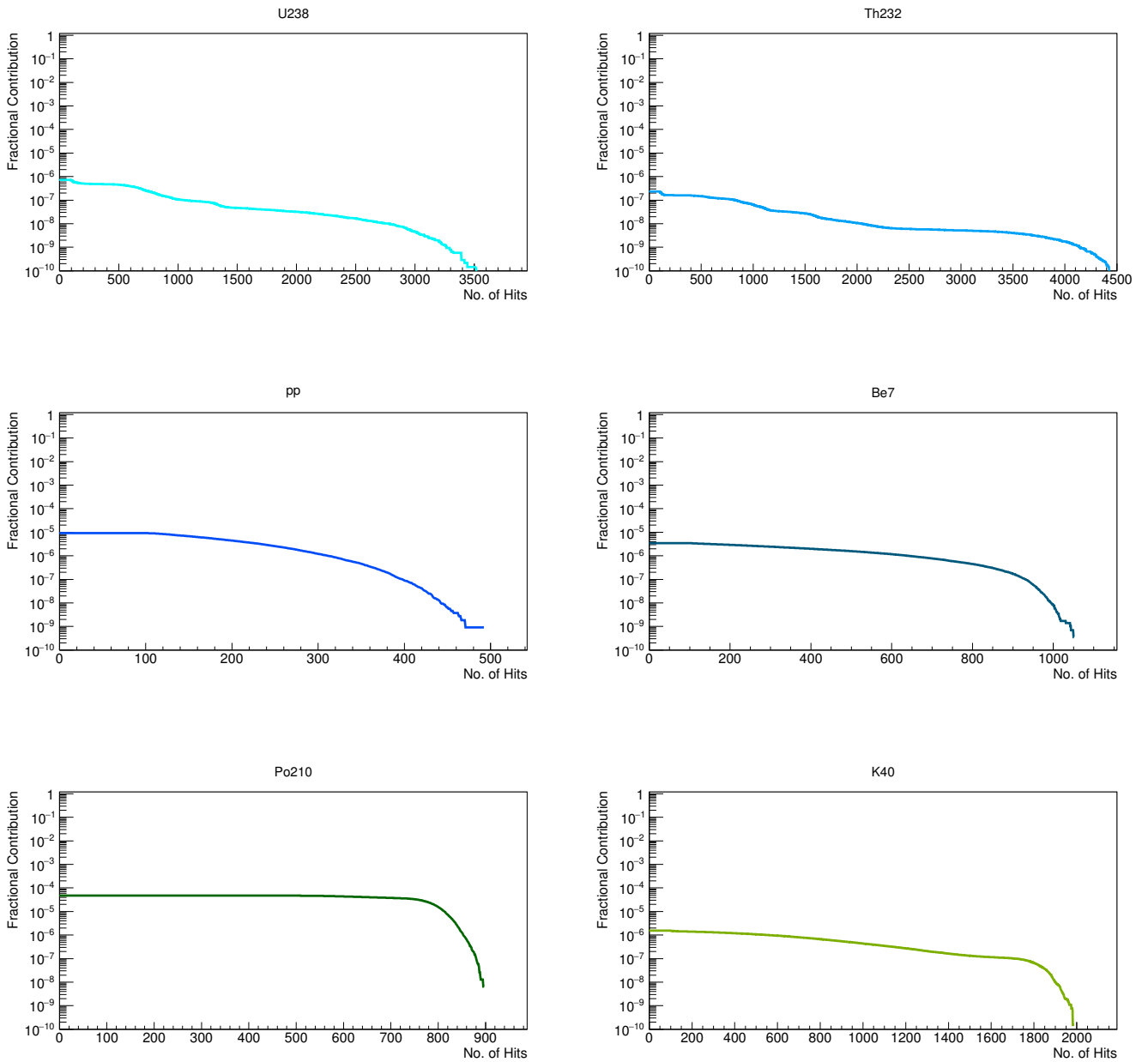
Appendices

Fractional contributions to trigger rate

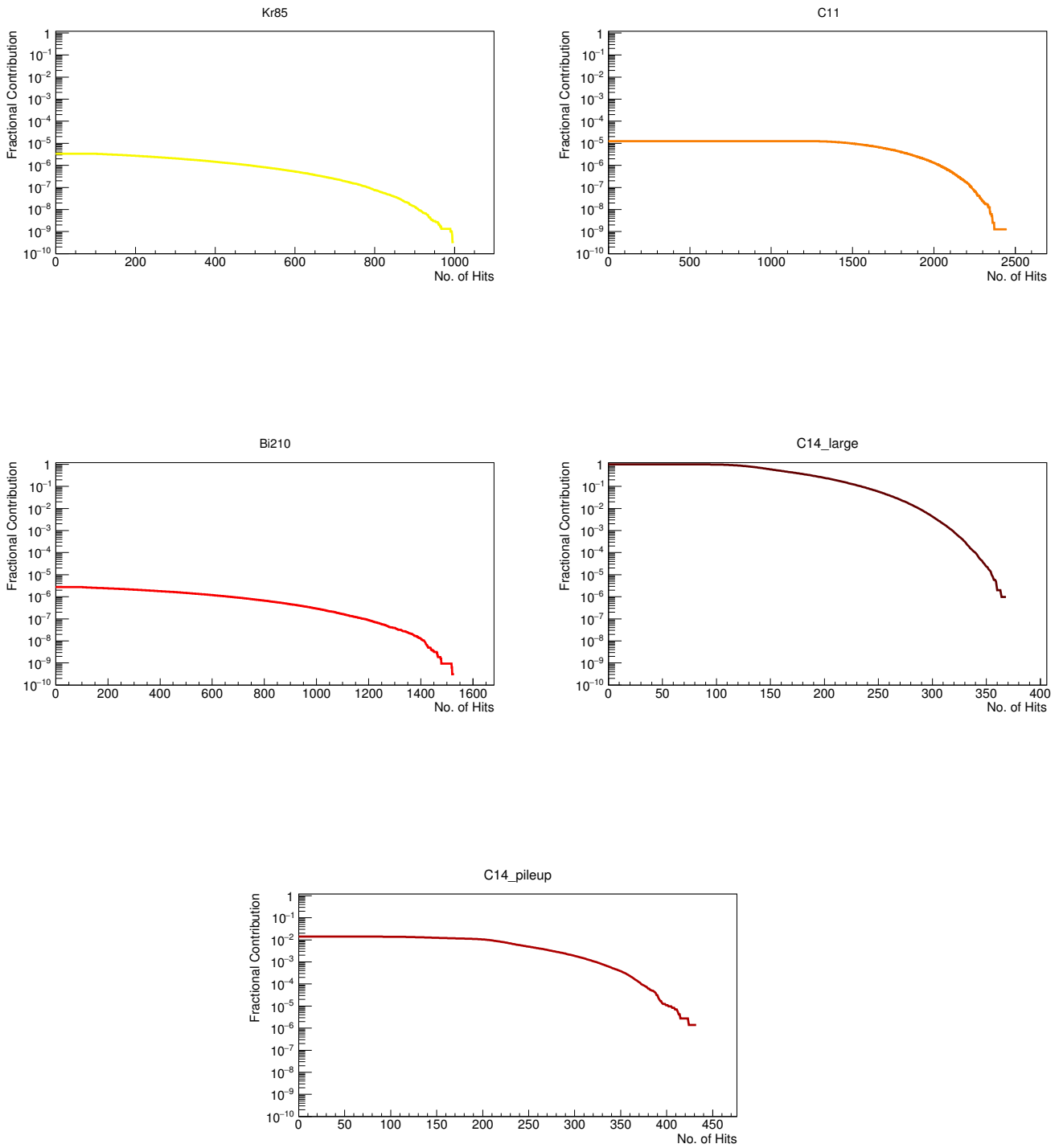

Figure A.1: Fractional contributions

Figure A.2: Fractional contributions

Acknowledgements

Bibliography

[1] Steven Weinberg. A model of leptons. *Phys. Rev. Lett.*, 19:1264–1266, Nov 1967.

[2] Samoil M. Bilenky. Neutrino oscillations: brief history and present status. In *Proceedings, 22nd International Baldin Seminar on High Energy Physics Problems, Relativistic Nuclear Physics and Quantum Chromodynamics, (ISHEPP 2014): Dubna, Russia, September 15-20, 2014*, 2014.

[3] Lev Landau. On the conservation laws for weak interactions. In *Cp Violation*, pages 3–7. Elsevier, 1989.

[4] TD Lee. Td lee and cn yang, phys. rev. 105, 1671 (1957). *Phys. Rev.*, 105:1671, 1957.

[5] A Salam. A. salam, nuovo cimento 5, 299 (1957). *Nuovo cimento*, 5:299, 1957.

[6] B. Pontecorvo. Mesonium and anti-mesonium. *Sov. Phys. JETP*, 6:429, 1957. [Zh. Eksp. Teor. Fiz.33,549(1957)].

[7] B. Pontecorvo. Inverse beta processes and nonconservation of lepton charge. *Sov. Phys. JETP*, 7:172–173, 1958. [Zh. Eksp. Teor. Fiz.34,247(1957)].

[8] Raymond Davis, Don S. Harmer, and Kenneth C. Hoffman. Search for neutrinos from the sun. *Phys. Rev. Lett.*, 20:1205–1209, May 1968.

[9] John N Bahcall and Giora Shaviv. Solar models and neutrino fluxes. *The Astrophysical Journal*, 153:113, 1968.

[10] Q. R. Ahmad et al. Direct evidence for neutrino flavor transformation from neutral current interactions in the Sudbury Neutrino Observatory. *Phys. Rev. Lett.*, 89:011301, 2002.

[11] J.N. Abdurashitov, E.L. Faizov, V.N. Gavrin, A.O. Gusev, A.V. Kalikhov, T.V. Knodel, I.I. Knyshenko, V.N. Kornoukhov, I.N. Mirmov, A.M. Pshukov, A.M. Shalagin, A.A. Shikhin, P.V. Timofeyev, E.P. Veretenkin, V.M. Vermul, G.T. Zatsepin, T.J. Bowles, J.S. Nico, W.A. Teasdale, D.L. Wark, J.F. Wilkerson, B.T. Cleveland, T. Daily, R. Davis, K. Lande, C.K. Lee, P.W. Wildenhain, S.R. Elliott, M.L. Cherry, and R.T. Kouzes. Results from sage (the russian-american gallium solar neutrino experiment). *Physics Letters B*, 328(1):234 – 248, 1994.

[12] M. Altmann et al. Complete results for five years of GNO solar neutrino observations. *Phys. Lett.*, B616:174–190, 2005.

[13] Markus Ahlers, Klaus Helbing, and Carlos Pérez de los Heros. Probing Particle Physics with IceCube. 2018.

[14] Mauro Mezzetto. Long baseline neutrino experiments. In *Journal of Physics: Conference Series*, volume 718, page 022014. IOP Publishing, 2016.

[15] R. Acciarri et al. Long-Baseline Neutrino Facility (LBNF) and Deep Underground Neutrino Experiment (DUNE). 2015.

[16] G. Alimonti et al. Science and technology of BOREXINO: A Real time detector for low-energy solar neutrinos. *Astropart. Phys.*, 16:205–234, 2002.

[17] Fengpeng An, Guangpeng An, Qi An, Vito Antonelli, Eric Baussan, John Beacom, Leonid Bezrukov, Simon Blyth, Riccardo Brugnera, Margherita Buizza Avanzini, et al. Neutrino physics with juno. *Journal of Physics G: Nuclear and Particle Physics*, 43(3):030401, 2016.

[18] Ziro Maki, Masami Nakagawa, and Shoichi Sakata. Remarks on the unified model of elementary particles. *Progress of Theoretical Physics*, 28(5):870–880, 1962.

[19] Ling-Lie Chau and Wai-Yee Keung. Comments on the parametrization of the kobayashi-maskawa matrix. *Physical Review Letters*, 53(19):1802, 1984.

[20] Keith A Olive, Particle Data Group, et al. Review of particle physics. *Chinese Physics C*, 38(9):090001, 2014.

[21] I. Esteban, M. C. Gonzalez-Garcia, M. Maltoni, I. Martinez-Soler, and T. Schwetz. Updated fit to three neutrino mixing: exploring the accelerator-reactor complementarity. *Journal of High Energy Physics*, 1:87, January 2017.

[22] Florian Kaether, Wolfgang Hampel, Gerd Heusser, Juergen Kiko, and Till Kirsten. Reanalysis of the gallex solar neutrino flux and source experiments. *Physics Letters B*, 685(1):47–54, 2010.

[23] JN Abdurashitov, EP Veretenkin, VM Vermul, VN Gavrin, SV Girin, VV Gorbachev, PP Gurkina, GT Zatsepin, TV Ibragimova, AV Kalikhov, et al. Solar neutrino flux measurements by the soviet-american gallium experiment (sage) for half the 22-year solar cycle. *Journal of Experimental and Theoretical Physics*, 95(2):181–193, 2002.

[24] B Aharmim, SN Ahmed, AE Anthony, N Barros, EW Beier, A Bellerive, B Beltran, M Bergevin, SD Biller, K Boudjemline, et al. Combined analysis of all three phases of solar neutrino data from the sudbury neutrino observatory. *Physical Review C*, 88(2):025501, 2013.

[25] K Abe, Y Hayato, T Iida, M Ikeda, C Ishihara, K Iyogi, J Kameda, K Kobayashi, Y Koshio, Y Kozuma, et al. Solar neutrino results in super-kamiokande-iii. *Physical Review D*, 83(5):052010, 2011.

[26] Oleg Smirnov, G Bellini, J Benziger, D Bick, G Bonfini, D Bravo, B Caccianiga, F Calaprice, A Caminata, P Cavalcante, et al. Solar neutrino with borexino: Results and perspectives. *Physics of Particles and Nuclei*, 46(2):166–173, 2015.

[27] Alec Habig. A brief review of minos neutrino oscillation results. *Modern Physics Letters A*, 25(15):1219–1231, 2010.

[28] P. Adamson et al. Measurement of the neutrino mixing angle θ_{23} in NOvA. *Phys. Rev. Lett.*, 118(15):151802, 2017.

[29] K. Asakura et al. Results from KamLAND-Zen. *AIP Conf. Proc.*, 1666:170003, 2015.

[30] S. V. Cao. Latest results from T2K. In *53rd Rencontres de Moriond on Electroweak Interactions and Unified Theories (Moriond EW 2018) La Thuile, Italy, March 10-17, 2018*, 2018.

[31] J. I. Crespo-Anadón. Double Chooz: Latest results. *Nucl. Part. Phys. Proc.*, 265-266:99–104, 2015.

[32] F. Boehm et al. Final results from the Palo Verde neutrino oscillation experiment. *Phys. Rev.*, D64:112001, 2001.

[33] Shaomin Chen. The daya bay reactor neutrino experiment. In *Journal of Physics: Conference Series*, volume 120, page 052024. IOP Publishing, 2008.

[34] JK Ahn, S Chebotaryov, JH Choi, S Choi, W Choi, Y Choi, HI Jang, JS Jang, EJ Jeon, IS Jeong, et al. Observation of reactor electron antineutrinos disappearance in the reno experiment. *Physical Review Letters*, 108(19):191802, 2012.

[35] Ivan Esteban, M. C. Gonzalez-Garcia, Michele Maltoni, Ivan Martinez-Soler, and Thomas Schwetz. Updated fit to three neutrino mixing: exploring the accelerator-reactor complementarity. *JHEP*, 01:087, 2017.

[36] Zhi-Zhong Xing. Implications of the Daya Bay observation of θ_{13} on the leptonic flavor mixing structure and CP violation. *Chin. Phys.*, C36:281–297, 2012.

[37] M Fukugita and Tsutomu Yanagida. Barygenesis without grand unification. *Physics Letters B*, 174(1):45–47, 1986.

[38] Sacha Davidson, Enrico Nardi, and Yosef Nir. Leptogenesis. *Physics Reports*, 466(4-5):105–177, 2008.

[39] Wilfried Buchmüller, Pasquale Di Bari, and Michael Plümacher. Leptogenesis for pedestrians. *Annals of Physics*, 315(2):305–351, 2005.

[40] S. P. Mikheyev and A. Yu. Smirnov. Resonant amplification of ν oscillations in matter and solar-neutrino spectroscopy. *Il Nuovo Cimento C*, 9(1):17–26, Jan 1986.

[41] L. Wolfenstein. Neutrino oscillations in matter. *Phys. Rev. D*, 17:2369–2374, May 1978.

[42] WH Furry. On transition probabilities in double beta-disintegration. *Physical Review*, 56(12):1184, 1939.

[43] M Agostini, M Allardt, E Andreotti, AM Bakalyarov, M Balata, I Barabanov, M Barnabé Heider, N Barros, L Baudis, C Bauer, et al. Results on neutrinoless double-β decay of ge 76 from phase i of the gerda experiment. *Physical Review Letters*, 111(12):122503, 2013.

[44] Lutz Bornschein et al. Katrin-direct measurement of neutrino masses in the sub-ev region. *arXiv preprint hep-ex/0309007*, 2003.

70

[45] Nathalie Palanque-Delabrouille, Christophe Yèche, Julien Lesgourgues, Graziano Rossi, Arnaud Borde, Matteo Viel, Eric Aubourg, David Kirkby, Jean-Marc Legoff, James Rich, et al. Constraint on neutrino masses from sdss-iii/boss lyα forest and other cosmological probes. *Journal of Cosmology and Astroparticle Physics*, 2015(02):045, 2015.

[46] Shu Luo and Zhi-zhong Xing. Resolving the octant of θ_{23} via radiative $\mu - \tau$ symmetry breaking. *Phys. Rev. D*, 90:073005, Oct 2014.

[47] Debajyoti Dutta and Pomita Ghoshal. Probing CP violation with T2K, NOνA and DUNE in the presence of non-unitarity. *JHEP*, 09:110, 2016.

[48] Kevork N Abazajian, MA Acero, SK Agarwalla, AA Aguilar-Arevalo, CH Albright, S Antusch, CA Arguelles, AB Balantekin, G Barenboim, V Barger, et al. Light sterile neutrinos: a white paper. *arXiv preprint arXiv:1204.5379*, 2012.

[49] A Aguilar. A. aguilar et al.(lsnd collaboration), phys. rev. d 64, 112007 (2001). *Phys. Rev. D*, 64:112007, 2001.

[50] AA Aguilar-Arevalo, CE Anderson, SJ Brice, BC Brown, L Bugel, JM Conrad, R Dharmapalan, Z Djurcic, BT Fleming, R Ford, et al. Event excess in the miniboone search for $\nu_\mu \to \nu_e$ oscillations. *Physical Review Letters*, 105(18):181801, 2010.

[51] G Mention, M Fechner, Th Lasserre, Th A Mueller, D Lhuillier, M Cribier, and A Letourneau. Reactor antineutrino anomaly. *Physical Review D*, 83(7):073006, 2011.

[52] C Jaupart, S Labrosse, and JC Mareschal. Temperatures, heat and energy in the mantle of the earth. *Treatise on geophysics*, 7:253–303, 2007.

[53] Ondřej Šrámek, William F McDonough, and John G Learned. Geoneutrinos. *Advances in High Energy Physics*, 2012, 2012.

[54] Oleg Smirnov. Geoneutrino : experimental status and perspectives. *Journal of Physics: Conference Series*, 1056(1):012055, 2018.

[55] John N Bahcall, MH Pinsonneault, and Sarbani Basu. Solar models: Current epoch and time dependences, neutrinos, and helioseismological properties. *The Astrophysical Journal*, 555(2):990, 2001.

[56] Michael Wurm. Solar neutrino spectroscopy. *Physics Reports*, 685:1–52, 2017.

[57] Bruce T Cleveland, Timothy Daily, Raymond Davis Jr, James R Distel, Kenneth Lande, CK Lee, Paul S Wildenhain, and Jack Ullman. Measurement of the solar electron neutrino flux with the homestake chlorine detector. *The Astrophysical Journal*, 496(1):505, 1998.

[58] Yusuke Koshio. Solar results from super-kamiokande. In *AIP Conference Proceedings*, volume 1666, page 090001. AIP Publishing, 2015.

[59] Miao He, JUNO collaboration, et al. Jiangmen underground neutrino observatory. *Nuclear and Particle Physics Proceedings*, 265:111–113, 2015.

[60] R Zimmermann, J Ebert, C Hagner, B Koppitz, V Saveliev, W Schmidt-Parzefall, J Sewing, and Y Zaitsev. The precision tracker of the opera detector. *Nuclear Instruments and Methods in Physics Research Section A: Accelerators, Spectrometers, Detectors and Associated Equipment*, 555(1-2):435–450, 2005.

[61] T Adam, E Baussan, Kurt Borer, JE Campagne, N Chon-Sen, C de La Taille, N Dick, M Dracos, G Gaudiot, T Goeltzenlichter, et al. The opera experiment target tracker. *Nuclear Instruments and Methods in Physics Research Section A: Accelerators, Spectrometers, Detectors and Associated Equipment*, 577(3):523–539, 2007.

[62] Zelimir Djurcic, Xiaonan Li, Wei Hu, Haonan Gan, Sergey Dmitrievsky, Kun Zhang, Can Fang, Jian Fang, Mengjiao Xiao, Li Kang, et al. Juno conceptual design report. Technical report, 2015.

[63] Virginia Strati, Marica Baldoncini, Ivan Callegari, Fabio Mantovani, William F McDonough, Barbara Ricci, and Gerti Xhixha. Expected geoneutrino signal at juno. *Progress in Earth and Planetary Science*, 2(1):5, 2015.

[64] Thomas Schwetz, Mariam Tortola, and JWF Valle. Global neutrino data and recent reactor fluxes: the status of three-flavour oscillation parameters. *New Journal of Physics*, 13(6):063004, 2011.

[65] Gianpaolo Bellini, J Benziger, D Bick, G Bonfini, D Bravo, M Buizza Avanzini, B Caccianiga, L Cadonati, F Calaprice, P Cavalcante, et al. Final results of borexino phase-i on low-energy solar neutrino spectroscopy. *Physical Review D*, 89(11):112007, 2014.

[66] Gianpaolo Bellini. The impact of borexino on the solar and neutrino physics. *Nuclear Physics B*, 908:178–198, 2016.